



Technische Universität München  
Fakultät für Medizin

*Streptococcus pneumoniae* TIGR4 pilus-1 biomechanical  
aspects of adhesion during interaction with host  
extracellular matrix proteins fibronectin and collagen I

Tanja D. Becke

Vollständiger Abdruck der von der  
Fakultät für Medizin  
der Technischen Universität München zur Erlangung des akademischen Grades  
eines

Doktors der Naturwissenschaften

genehmigten Dissertation.

Vorsitzender: Prof. Dr. Markus Gerhard

Prüfende/-r der Dissertation:

1. Prof. Dr. Arndt F. Schilling
2. Prof. Dr. Matthias Rief

Die Dissertation wurde am 09.11.2018 bei der Technischen Universität München eingereicht  
und durch die Fakultät für Medizin am 13.06.2019 angenommen.







---

# Abstract

Surface piliation procures benefits for bacteria during adhesion to and invasion of host cells. Therefore, a detailed investigation of how pili adhere to host cells is a key aspect in understanding their role during infection. *Streptococcus pneumoniae* TIGR 4, a clinical relevant serotype 4 strain, is an important etiologic agent of respiratory tract infections and diseases. Besides a plurality of other cell wall anchored adhesins, it is capable of expressing pilus-1, a hair like structure, consisting of a RrgC cell wall anchor protein, several RrgB backbone proteins and a terminal RrgA tip adhesin.

In this thesis single molecule force spectroscopy (SMFS) and lateral force microscopy (LFM) were used to investigate the binding of single pilus-1 proteins (pilins) to fibronectin (Fn) and collagen I (Col I), two members of the host extracellular matrix (ECM). The SMFS results show that full length RrgA (RrgA FI) and its terminal domains D3 and D4 bind to Fn with forces of 51.6 (full length), 52.8 (D3), and 46.2 pN (D4) at force-loading rates of around 1500 pN/s. The dissociation rate constant  $k_{off} = 3.91 \text{ s}^{-1}$  and the bond lifetime at zero force  $\tau = 0.26 \text{ s}$  of RrgA FI - Fn is the average of the values obtained for the single domains D3 ( $k_{off} = 6.72 \text{ s}^{-1}$ ,  $\tau = 0.15 \text{ s}$ ) and D4 ( $k_{off} = 2.33 \text{ s}^{-1}$ ,  $\tau = 0.43 \text{ s}$ ) and indicates a rapid dissociation of RrgA FI - Fn bonds. Selective saturation of D3 and D4 binding sites on Fn showed that both domains can interact simultaneously with Fn, revealing a two-domain binding mechanism for the pilus-1 tip protein. In addition RrgA FI and full length RrgB (RrgB FI) can bind to Col I with forces of 39.4 and 32.4 pN at force-loading rates of around 1500 pN/s, respectively. During LFM experiments (150 pN contact force,  $11 \mu\text{m s}^{-1}$  tip velocity) comparable forces established between RrgA FI and Col I (38.3 pN). However, interactions between RrgB FI and Col I were 2.5 times stronger

---

(80.1 pN) as in SMFS. In summary, the results may indicate a force driven, consecutive interlocking of the pilus-1 backbone protein with Col I fibrils rather than a specific interaction of this both.

In conclusion, the high off rates and the corresponding short lifetime of the RrgA-Fn bond may enable piliated pneumococci to form and maintain a transient contact to fibronectin-containing host surfaces. In addition, RrgB may interlock with Col I fibrils of the ECM, which in concert with the RrgA-Fn and RrgA- Col I bonds may hinder the displacement of *S. pneumoniae* from host surfaces in flow conditions. This may permit the bacterium to efficiently scan the surface for specific receptors promoting host cell adhesion and invasion, a mechanisms possibly shared with other piliated Gram-positive bacteria.

---

# Zusammenfassung

Während der Adhäsion an und der anschließenden Invasion von Wirtszellen besitzen Bakterien mit Pili einen Vorteil gegenüber Bakterien ohne diese Oberflächenadhäsine. Daher ist eine detaillierte Untersuchung, wie Pili an den Wirtszellen anhaften ein Schlüsselaspekt um ihre Rolle innerhalb der bakteriellen Pathogenität zu verstehen. *Streptococcus pneumoniae* TIGR 4, ein klinisch relevanter Serotyp-4-Stamm, kann vermehrt Atemwegsinfektionen und –erkrankungen auslösen. Neben einer Vielzahl anderer adhäsiver Oberflächenproteine ist er in der Lage eine haarähnliche Struktur, den Pilus-1, zu exprimieren. Dieser besteht aus einem Protein, das den Pilus in der Zellwand verankert (RrgC), mehreren Proteinen, die das Rückgrat des Pilus bilden (RrgB), und einem terminalen Adhäsionsprotein RrgA.

In dieser Arbeit wurden Einzelmolekül-Kraftspektroskopie (SMFS) und Lateralkraftmikroskopie (LFM) verwendet, um die Bindung der einzelnen Pilus-1-Proteine an Fibronektin (Fn) und Kollagen I (Col I), zwei Proteine der extrazellulären Wirtsmatrix (ECM), zu untersuchen. Die SMFS Ergebnisse zeigen, dass das vollständige RrgA (RrgA Fl) und seine terminalen Domänen D3 und D4 bei einer Kraftladungsrate von etwa 1500 pN/s mit Kräften von 51,6 (RrgA), 52,8 (D3) und 46,2 pN (D4) an Fn binden. Die Dissoziationskonstante  $k_{off} = 3.91 \text{ s}^{-1}$  und die Lebensdauer der RrgA Fl - Fn Bindung bei spontaner Dissoziation  $\tau = 0.26 \text{ s}$  entspricht dem Mittel der Werte, die für die einzelnen Proteindomänen D3 ( $k_{off} = 6.72 \text{ s}^{-1}$ ,  $\tau = 0.15 \text{ s}$ ) und D4 ( $k_{off} = 2.33 \text{ s}^{-1}$ ,  $\tau = 0.43 \text{ s}$ ) gemessen wurden und kennzeichnet damit eine schnelle Trennung der RrgA FL - Fn Bindung. Die selektive Absättigung der D3- und D4-Bindungsstellen auf Fn zeigte, dass beide Domänen gleichzeitig mit Fn interagieren können, und offenbart so einen Zwei-Domänen-Bindungsmechanismus für das Pilus-1-Adhäsionsprotein. Zusätzlich können RrgA Fl und das vollständige RrgB

---

(RrgB Fl) bei einer Kraftladungsrate von ca. 1500 pN/s mit Kräften von 39,4 bzw. 32,4 pN an Col I binden. Während der LFM-Experimente (150 pN Kontaktkraft,  $11 \mu\text{m s}^{-1}$  Lateralgeschwindigkeit) wurden ähnliche Kräfte zwischen RrgA und Col I (38,3 pN) festgestellt. Dagegen waren die Wechselwirkungen zwischen RrgB Fl und Col I mit 80,1 pN rund 2.5-mal stärker als bei den SMFS Experimenten. Daraus schlussfolgernd deuten die Ergebnisse eher auf ein serielles, räumliches Ineinandergreifen des Pilus-1-Rückgratproteines mit den Col I Fasern hin, als auf eine spezifische Interaktion der beiden.

Zusammenfassend sprechen die hohe Dissoziationsrate und die entsprechend kurzen Lebensdauer der RrgA - Fn-Bindung für die Bildung und Aufrechterhaltung eines vorübergehenden Kontaktes zu fibronectinhaltigen Wirtsoberflächen. Darüber hinaus scheint es möglich, dass sich RrgB in den Col I Fasern der ECM verhakt und so zusammen mit der Interaktion von RrgA mit Fn und Col I die Verdrängung von *S. pneumoniae* von der Wirtsoberfläche unter Strömungsbedingungen verhindert. Dadurch wird es dem Bakterium möglich, die Oberfläche effizient nach spezifischen Rezeptoren abzutasten, die die Adhäsion und Invasion von Wirtszellen fördern - ein Mechanismus, auf den möglicherweise auch anderen pilierte Gram-positiven Bakterien zurückgreifen können.



# Table of Contents

<b>Abstract .....</b>	<b>I</b>
<b>Zusammenfassung.....</b>	<b>III</b>
<b>Table of Contents .....</b>	<b>i</b>
<b>Abbreviations.....</b>	<b>iii</b>
<b>1 Introduction .....</b>	<b>1</b>
<b>2 <i>Streptococcus Pneumoniae</i> .....</b>	<b>3</b>
2.1 Epidemiology, Microbiology, and Pathogenesis.....	3
2.2 Pneumococcal Adhesins .....	5
2.3 Pneumococcal Pilus-1 .....	8
2.3.1 Pilus-1 Tip Protein RrgA .....	8
2.3.2 Pilus-1 Backbone Protein RrgB .....	9
2.3.3 Pilus-1 Anchor Protein RrgC .....	10
<b>3 Atomic Force Microscopy .....</b>	<b>11</b>
3.1 AFM Imaging .....	11
3.1.1 Contact Force Imaging .....	11
3.1.2 Intermittent Contact Imaging.....	12
3.2 Dynamic Single Molecule Force Spectroscopy .....	13
3.2.1 Evaluation of Dynamic Force Spectroscopy Experiments .....	14
3.2.2 Kinetics of Force Induced Bond Rupture.....	17
3.3 Lateral Force Microscopy .....	20
3.3.1 Evaluation of Friction Force Experiments .....	21
3.4 Surface Immobilization Strategy .....	24
<b>4 Recent Single Cell and Single Protein work .....</b>	<b>29</b>
<b>5 Aim of the Work .....</b>	<b>31</b>

## Table of Contents

---

<b>6</b>	<b>Material and Methods.....</b>	<b>33</b>
6.1	Material.....	33
6.1.1	Materials and Chemicals.....	33
6.1.2	Proteins and Antibodies.....	34
6.1.3	Strains and Plasmids.....	34
6.1.4	Equipment.....	35
6.1.5	Software.....	35
6.2	Methods.....	37
6.2.1	Protein Expression and Purification.....	37
6.2.2	Protein Analysis.....	38
6.2.3	Enzyme Linked ImmunoSorbent Assay.....	41
6.2.4	Surface Functionalization.....	41
6.2.5	Immobilization of Proteins for SMFS and LFM.....	42
6.2.6	Dynamic Single Molecule Force Measurements.....	43
6.2.7	Lateral Force Measurements.....	44
<b>7</b>	<b>Results and Discussion.....</b>	<b>45</b>
7.1	Pneumococcal Pilus-1 Tip Protein RrgA – Fibronectin Adhesion.....	45
7.1.1	Interaction of Full-Length RrgA with Fibronectin.....	45
7.1.2	Interaction of Individual Domains D1–D4 with Fibronectin.....	49
7.1.3	Simultaneous Binding of D3 and D4 to Fibronectin.....	51
7.2	Pneumococcal Pilus-1 Pilins – Collagen I Adhesion.....	57
7.2.1	SMFS of Full-Length RrgA, RrgB and RrgC with Collagen I.....	57
7.2.2	LFM of Full-Length RrgA, RrgB and RrgC with Collagen I.....	61
<b>8</b>	<b>Conclusion and Outlook.....</b>	<b>65</b>
<b>9</b>	<b>References.....</b>	<b>69</b>
<b>10</b>	<b>Supplementary Information.....</b>	<b>S1</b>
10.1	Figures.....	S3
10.2	Protocols.....	S10
10.2.1	Purification of Proteins.....	S10
10.2.2	Immobilization of Proteins for SMFS and LFM.....	S12
10.2.3	Atomic Force Microscopy Based Single Molecule Force Spectroscopy.....	S17
<b>11</b>	<b>Lebenslauf.....</b>	<b>105</b>
<b>12</b>	<b>Eidesstattliche Erklärung.....</b>	<b>107</b>
<b>13</b>	<b>Danksagung.....</b>	<b>1079</b>

## Abbreviations

<b>AFM</b>	Atomic Force Microscope
<b>APS</b>	Ammoniumpersulfate
<b>ATR-FTIR</b>	Attenuated Total Reflection Fourier Transform Infrared Spectroscopy
<b>BSA</b>	Bovine Serum Albumin
<b>Cbp</b>	Pneumococcal Choline Binding Protein
<b>Cna</b>	Collagen-Binding Adhesin
<b>Col I</b>	Collagen I
<b>ECM</b>	Extra Cellular Matrix
<b>EDC</b>	1-(3-(dimethylamino)propyl)-3-ethylcarbodiimide
<b>ELISA</b>	Enzyme Linked ImmunoSorbent Assay
<b>eWLC</b>	Extensible Worm-Like Chain
<b>FDA</b>	Food and Drug Administration (United States)
<b>Fl</b>	Full length
<b>Fn</b>	Fibronectin
<b>FnBP or Fbp</b>	Fibronectin-Binding Protein
<b>IMAC</b>	Immobilized Metal chelate Affinity Chromatography
<b>IPD</b>	Invasive Pneumococcal Disease
<b>IPTG</b>	Isopropyl- $\beta$ -d-thiogalactopyranoside
<b>LFM</b>	Lateral Force Microscopy
<b>MIDAS</b>	Integrin Metal Ion-Dependent Adhesion Site
<b>MSCRAMMs</b>	Microbial Surface Components Recognizing Adhesive Matrix Molecules
<b>NCSP</b>	Non-Classical Surface Protein
<b>NHS</b>	N-hydroxysuccinimide
<b>NVT</b>	Non-Vaccine Type
<b>PBS</b>	Phosphate Buffered Saline
<b>PCho</b>	Phosphorylcholine

## **Abbreviations**

---

<b>PCV</b>	Pneumococcal Conjugate Vaccine
<b>PEG</b>	Polyethylene Glycol
<b>pNPP</b>	p-nitrophenyl phosphate
<b>PPSV</b>	Pneumococcal Polysaccharide Vaccine
<b>PSD</b>	Power Spectral Density
<b>QCM</b>	Quartz Crystal Microbalance
<b>RMS</b>	Root Mean Squared
<b>SCFS</b>	Single Cell Force Spectroscopy
<b>SDS-PAGE</b>	Sodium Dodecyl Sulfate Polyacrylamide Gel Electrophoresis
<b>SEC</b>	Size-Exclusion-Chromatography
<b>SI</b>	Supplement Information
<b>SMFS</b>	Single Molecule Force Spectroscopy
<b>SPR</b>	Surface Plasmon Resonance
<b>SSURE</b>	Streptococcal Surface Repeats
<b>TBS</b>	TRIS Buffered Saline
<b>TEMED</b>	N,N,N',N'-Tetramethylethylenediamine
<b>WLC</b>	Worm-Like Chain

# 1 Introduction

*Streptococcus pneumoniae*, a Gram-positive, prevalent extracellular pathogen, is responsible for a plurality of respiratory tract infections and invasive diseases such as otitis media, community acquired pneumonia, septicemia and meningitis [1-3]. In 2015, it was estimated that 1.5 million people worldwide died from pneumococcal pneumonia [4]. The available pneumococcal vaccines are generally efficacious and safe, but led to increasing incidence of non-vaccine types by either serotype replacement or switching and may show no effects on certain serotypes not included in the vaccines [5-7]. In addition, the emergence of antibiotic resistance has made treatment of pneumococcal diseases more difficult, even if the incidence of antibiotic-resistant serotypes declined substantially after the introduction of the pneumococcal vaccines [5, 8, 9]. One key step for infection initiation is the adherence of pneumococci to eukaryotic surfaces through the interaction of bacterial surface-exposed proteins and host specific factors, *e.g.* the extracellular matrix [10-14]. Besides a plurality of other cell wall anchored adhesins, the pneumococcus is able to express at least two long, polymeric protein appendages, so called pili, which can reach through the bacterial polysaccharide capsule and/or host surface barriers (*e.g.* mucosa) [15, 16]. One of them is the more than 1  $\mu\text{m}$  long pilus-1 [17], which can decorate up to 30 % of the pneumococcal serotypes [18-20]. It is a multimeric structure and consists of a RrgC cell wall anchor protein, multiple RrgB backbone subunits and a terminal RrgA adhesin, which are covalently linked in a linear manner [17]. It has been shown that RrgA can interact with fibronectin, collagen I and laminin, whereas the binding of pilins RrgB and RrgC to these extra cellular matrix components was negligible [14, 21].

## ***Introduction***

---

The atomic force microscope (AFM), which allows to measure interactions on the single molecule [22-25] and single cell level [26-28], has, since its invention in 1986 [29], provided new insights into the binding mechanisms of numerous bacterial adhesins, such as pilus proteins from *Pseudomonas aeruginosa* [30, 31], *Neisseria gonorrhoeae* [32], and *Escherichia coli* [33, 34].

In this work, AFM was employed in the single molecule force spectroscopy (SMFS) and the lateral force microscopy (LFM) mode to explore the interaction force and binding mechanics of *S. pneumoniae* TIGR 4 pilus-1 pilins (RrgA, RrgB and RrgC) with the extracellular matrix proteins fibronectin (Fn) and collagen I (Col I) [35-37]. The individual pilus proteins and the four domains (D1, D2, D3 and D4) of RrgA were heterologously expressed in *E. coli*, purified, checked for correct folding and covalently attached to the AFM tip under nearly native conditions *via* heterobifunctional spacer molecules. Human Fn or Col I were immobilized on a glass substrate using the same immobilization method with the same surface linker. Interaction forces for the protein pairs were determined from the SMFS force curves using the extensible Worm-like chain model [38-40]. The receptor-ligand bond dissociation under force, and the corresponding kinetic parameters, *e.g.* the off-rate and bond lifetime were modeled with the Bell-Evans-Ritchie model [41, 42]. LFM experiments were analyzed using the beam mechanics model by which interaction forces in lateral direction can be approximated from the cantilever geometry and the spring constant, as well as the sensitivity of the AFM photodiode in vertical direction [43-45].

The results expand our understanding of how pili adhere to host cells and the surrounding matrices and may shed a light on one significant detail of pneumococcal invasion. As antimicrobial resistance, vaccine escape and a general tendency toward the spreading of piliated pneumococcal clones have been reported lately [5] and as pneumococcal infection can be potentially lethal, detailed analysis, like the one presented here, may help keep control in future.

## **2 *Streptococcus Pneumoniae***

*Streptococcus pneumoniae* was discovered independently by Pasteur and Sternberg in 1881 [46]. It is a Gram-positive, prevalent extracellular pathogen which inhabits the respiratory tract of mammals as part of the normal flora. It goes unnoticed when present in small densities, but can be triggered to become pathogenic. Intense study and surveillance has yielded an understanding of fundamental aspects of, *e.g.*, its physiology and helped to develop specific vaccines.

### **2.1 Epidemiology, Microbiology, and Pathogenesis**

Risk groups for diseases such as otitis media, community acquired pneumonia, septicemia and meningitis include young children, elderly, and patients with immunodeficiency [1-3, 47, 48]. Approximately 10% of all patients with invasive pneumococcal disease (IPD) die of their illness [49, 50] and depending on age, a high number of survivors of community-acquired pneumococcal meningitis develop long-term sequelae including hearing loss, neurological deficits, and neuropsychological impairment. In 2015, it was estimated that 1.5 million people worldwide died from pneumococcal pneumonia [4].

Until today at least 97 pneumococcal serotypes [51] have been identified by determining the structure of the polysaccharide capsular which includes the identification of saccharide residues and their order and linkages [52]. Although all serotypes can cause serious disease, a relatively limited number of serotypes, which differ between geographic areas and the time period studied, cause the majority of IPD.

In 2000, a 7-valent pneumococcal conjugate vaccine (PCV7) was licensed by the U.S. Food and Drug Administration (FDA), which was highly efficacious against IPD. This altered the serotype distribution and led to an increasing incidence of non-vaccine types (NVTs) by either serotype replacement or switching (*e.g.* through DNA uptake from other bacteria) [53-55]. Therefore PCV7 was replaced by PCV10 and PCV13 around 2010 which resulted in an overall reduction of IPD *e.g.* in Swedish children (by 68.5%), and the whole Swedish

population (by 13.5%) except the elderly [56]. However variable or little effects on certain serotypes, which are included in the PVCs, and serotype switching were still recorded [5-7]. In 2016, NVTs constituted 72% of IPD cases in the Swedish elderly [56]. Vaccination can be strengthened with the pneumococcal polysaccharide vaccine 23 (PPSV23, available since 1983) which targets 11 additional serotypes [8]. By the end of 2017 pneumococcal vaccines have been introduced in 135 countries and the global coverage was estimated to be 44% [57], but until today where is no vaccine availed that covers all relevant serotypes. The pneumococcal serotypes are determined based on the composition of the polysaccharide capsule, whose gen locus shows a similar organization in all strains and which is the most important virulence factor of pneumococci. It can vary between a transparent (decreased polysaccharide) and an opaque state (increased polysaccharide) [58]. While the transparent phenotype dominates in the nasopharynx, the opaque phase predominates in the blood, promotes biofilm formation [59] and is able to invade the lung and brain [60]. The precise mechanism of this phase variation is unclear but it seems to play a role in evasion of host defences through (sterically) hindering the host immune system to react with the cell wall and associated molecules [61, 62], while promoting attachment to host cells by pneumococcal cell wall surface adhesins [63, 64]. The cell wall, as classical Gram-positive structure, consists of a thick layer of peptidoglycans and teichoic acids which contain an unusual ribitol phosphate backbone and covalently attached phosphorylcholine (PCho) [65, 66]. PChos are converted from choline taken up from the environment, and serve as anchors for the noncovalent linkage of pneumococcal cholinebinding proteins (Cbp) [65, 67, 68]. In addition to the Cbps, transmembrane proteins, lipoproteins, cell wall anchored proteins and non-classical surface proteins (NCSP) can be distinguished within the group of pneumococcal surface proteins (see chapter 2.2) [69, 70].



A plurality of these surface-attached (and secreted) proteins contribute individually and/or in concert to pneumococcal pathogenesis. They directly or indirectly (*e.g.* release of host tissue damaging products, regulation of adhesin production) enable pneumococcal adhesion to and invasion of host tissues and matrices and often allow successful evasion from host (innate) immune response.

## **2.2 Pneumococcal Adhesins**

Equipped with the plurality of surface proteins (see Fig.2.1 for an overview), whose presence depends on the serotype, the pneumococcus can either directly bind to the host cell or target the extra cellular matrix (ECM). The ubiquitous ECM with its tissue specific composition of glycosylated proteins and glycosaminoglycans provides structural support for and enables signaling between cells. It provides mechanical inputs into cells, allows for their motility and regulates diverse functions, including cell determination, differentiation, proliferation, survival, polarity and migration [35]. Among others, the ECM includes macromolecules like collagens, elastins, fibronectins and laminins, which can be targeted by a major proportion of pneumococcal adhesins (microbial surface components recognizing adhesive matrix molecules, MSCRAMMs) [71].

A prominent MSCRAMM is the pneumococcal adherence and virulence factor A (PavA), which was the first fibronectin-binding protein (FnBP) identified in *S. pneumoniae* [10]. PavA shares sequence homology with other fibronectin-binding proteins but lacks the typical fibronectin-binding repeats [72]. It belongs to the NCSPs which are often enzymes of metabolic pathways but exert additional biological functions including the adhesion to host tissue. In addition, host-cell adhesins (like the pneumococcal surface proteins, PspA and PspC) can be found in the Cbp family, which also includes proteins for the remodeling of the cell wall (*e.g.* hydrolases LytA and LytC) and other virulence factors [69]. PspA is present in practically all clinically important serotypes [69] and its interactions with lactoferrin [73] and its inhibition of complement deposition [74] play important roles in the escape from the innate immune system.

## *Streptococcus Pneumoniae*

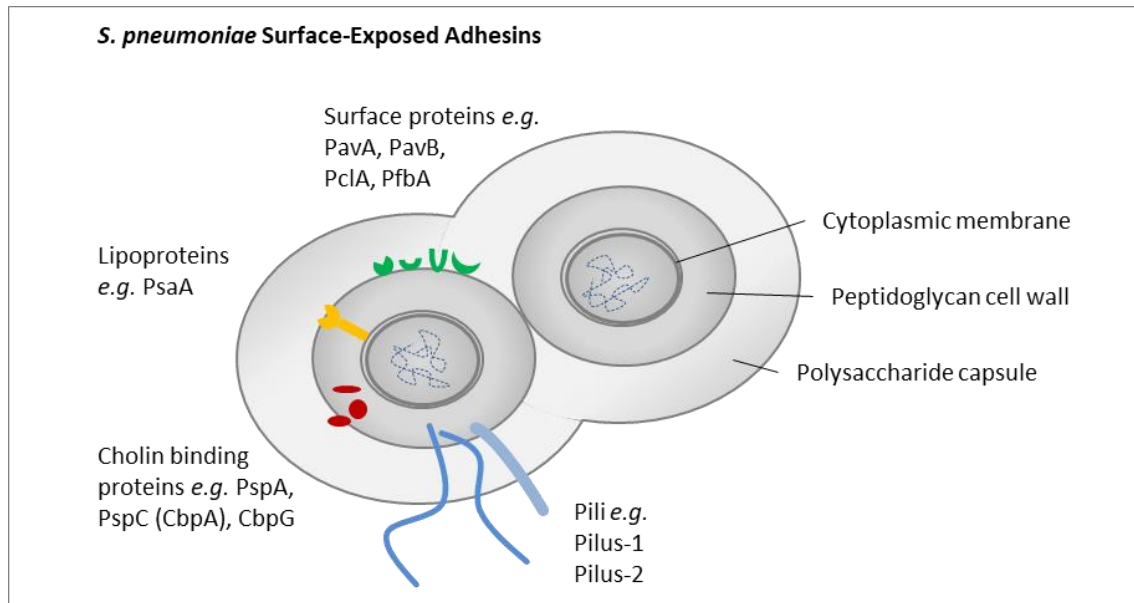


**Figure 2.1: Illustration of surface-exposed adhesins of *S. pneumoniae*.**

Equipped with a plurality of surface attached proteins, pneumococcus can either directly bind to eukaryotic cells or target the cell surrounding extra cellular matrix, thereby enabling invasion into host tissues and evasion from host (innate) immune responses. The adhesins belong to groups of non-covalently anchored cholinebinding proteins, covalently linked surface proteins or lipoproteins. PavA: pneumococcal adhesion and virulence factor A; PavB: pneumococcal adhesion and virulence factor B; PclA: pneumococcal collagen-like protein A; PfbA: plasmin- and fibronectin-binding protein A; PsaA: pneumococcal surface adhesion A; PspA: pneumococcal surface protein A; PspC: pneumococcal surface protein C; CbpG: cholinebinding protein G. Compare [70].

PspC (also known as SpsA and CbpA) is an important adhesins in *S. pneumoniae* as it binds the complement factor C3 [75] and factor H [76] and enables bacterial translocation across the blood–brain barrier through binding to the corresponding receptors [11, 77].

Another highly conserved pneumococcal surface adhesion, PsaA, which is known for its metal ion-binding activity, interacts with E-cadherin, the major determinant of epithelial barrier integrity [78]. It belongs to the group of surface lipoproteins which have important roles in physiological processes (e.g. substrate uptake, signal transduction, antibiotic and oxidative stress resistance) and promotes colonization, invasion into, and survival in the bloodstream [70].

Furthermore *S. pneumoniae* possesses an arsenal of sortase/LPxTG-anchored surface proteins, e.g. lytic enzymes like the neuraminidase A (NanA). These enzymes enable the degradation of human glycoproteins and glycosaminoglycans (components of body fluids and ECM) which not only results in a direct damage of host tissue, but also in an unmasking of potential binding sites for the pneumococcus [69, 79]. Several other sortase-anchored surface proteins have been implicated in pneumococcal adhesion and colonization, such as PavB (also known as plasmin- and fibronectin-binding protein B, PfbB) [80], pneumococcal collagen-like protein A (PclA) [81] and plasmin- and fibronectin-binding protein A (PfbA) [82]. PavB, which is not homologous to PavA, is a conserved multidomain protein with numerous streptococcal surface repeats (SSURE), which bind to fibronectin and plasminogen with an increasing avidity depending on the number of SSURE domains present [10, 71, 80]. PfbA like PavB binds to fibronectin, plasminogen and in addition to human serum albumin and is associated with the invasion of lung and laryngeal epithelial cells [82, 83].

*S. pneumoniae* is able to express at least two long, polymeric protein appendages, so called pili. The pilus-1 is usually formed from a single chain of covalently linked subunit proteins (pilins) [84, 85]. Its pilins are covalently joint to one another and to the cell wall by sortase activity, but in contrast to the other members of the LPxTG-anchored surface protein family, they can reach through the bacterial polysaccharide capsule and/or host surface barriers (e.g. mucosa) [16-18, 20, 21, 58]. The streptococcal pilus-1 (pathogenicity islet PI-1, the *r/rA* islet) [16] is a complex, well studied structure while pilus-2 (pathogenicity islet PI-2) type was only described recently [15, 86]. Both have been associated with pneumococcal pathogenesis and long-distance adhesion to host structures such as cellular receptors and proteins of the ECM [13, 15].

## 2.3 Pneumococcal Pilus-1

The pilus-1, which can be found in ~30 % of the pneumococcal serotypes [18-20] consists of a RrgC cell wall anchor protein, multiple RrgB backbone subunits and a terminal RrgA adhesin (Fig. 2.2 a). [17, 87]. Isopeptide bonds are present in all pilus-1 pilin molecules and have been shown to play important roles in structure stabilization for major or minor pilin proteins, and the whole pilus [88-92]. Pilus-1 has been associated with virulence [16, 93] and the capability of the pneumococcus to adhere to host cell molecules, like the toll-like receptor 2 [13] and the complement receptor 3 [12], as well as the polymeric immunoglobulin receptor and platelet endothelial cell adhesion molecule, leading to the penetration of the blood–brain barrier [11]. As antimicrobial resistance, vaccine escape and a general tendency toward the spreading of piliated pneumococcal clones [5, 18, 94, 95] have been reported lately, the understanding of pilus-1 mediated host adhesion can be one key step towards the prevention of pneumococcal infection.

### 2.3.1 Pilus-1 Tip Protein RrgA

Full length RrgA (RrgA FI) harbours four domains (D1, D2, D3 and D4) which are arranged like beads on a string *via* flexible linker sequences, resulting in approximate dimensions of 19 nm x 7 nm (Fig. 2.2 b) [17, 88]. D2 and D4 are stabilized by two intramolecular isopeptide bonds. RrgA shows sequence and structure similarities to other gram-positiv pilins, *e.g.* GBS104 and GBS52 (adhesive minor pilins from *Streptococcus agalactiae*) [96, 97], or SPY0125 (also known as CPA, adhesive pilin from *Streptococcus pyogenes*) [98]. Structure alignment revealed that domains D1 and D4 show high similarity to IgG domains [88, 97] and D2 to the collagen-binding adhesin Cna from *S. aureus* [28, 99]. A part of the fold of D3 resembles that of the A3 domain of human von Willebrand factor, concealing an integrin metal ion-dependent adhesion site (MIDAS) motif and forms a large cradle shaped surface of basic character [88, 100].

It has been shown that RrgA can interact with fibronectin (Fn), Collagen I (Col I) and laminin, whereas the binding of the anchor-pilin RrgC and the backbone protein RrgB to

these ECM components was negligible [14, 21]. However, a detailed understanding of underlying binding mechanism is still lacking.

### 2.3.2 Pilus-1 Backbone Protein RrgB

Full length RrgB (RrgB FI) displays a modular structure comprising four domains, each with an intramolecular isopeptide bond [89]. Thereby, D1, D2 and D4 form ‘beads on a string’ with D3 laterally arranged relatively to D2 displaying an approximate dimension of 11.5 nm x 4 nm (Fig.2.2 b) [89, 101, 102]. Like RrgC, the cores of all four domains of RrgB display  $\beta$ -barrel folds with additional minor secondary structural features and thus D1, D3 and D4 correspond to the prototype CnaB fold and D2 to the CnaA like region from collagen-binding adhesin Cna [28, 99]. Homologues protein folds can be found in BcpA and SpaA, the major pilins of *B. cereus* [103] and *C. diphtheriae* [104] respectively, as well as in GBS52 from *S. agalactiae* [97].

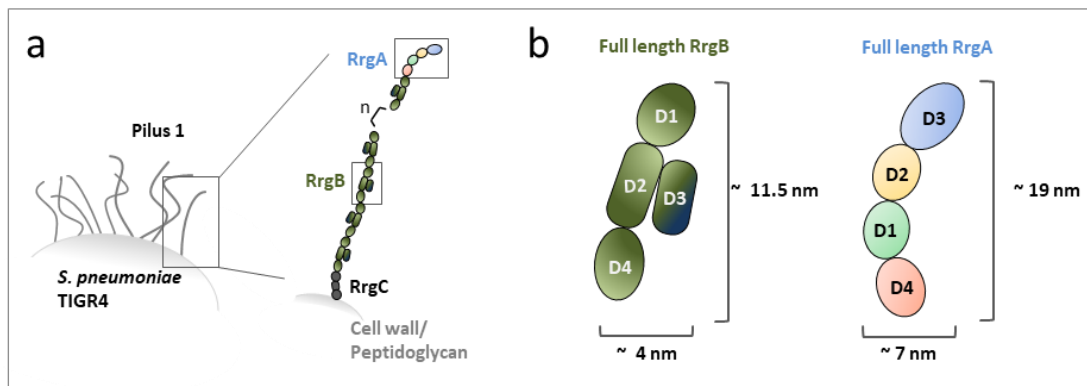


**Figure 2.2: Illustration of *S. pneumoniae* TIGR4 pilus-1, backbone pilin RrgB and adhesive tip pilin RrgA.** (a) Fine pili, which can be longer than 1  $\mu$ m, protrude from the bacterial surface (compare Hilleringmann *et al.*, EMBO J, 2009 [17]). The pilus-1 consists of a cell wall anchored protein RrgC at its proximal and the adhesin RrgA at the distal end. Multiple backbone proteins RrgB determine the pilus length (the figure has been modified from Becke *et al.*, ACSnano, 2018 [105]). (b) The three-dimensional structure of the full length major pilin RrgB is composed of four domains. Domains D4 (C-terminus), D2 and D1 (N-terminus) are arranged in a linear manner, with D3 laterally arranged relatively to D2 (compare El Mortaji *et al.*, Biochem. J., 2012 [89], RCSB PDB: 2Y1V and supplement information (SI) Fig. S2). Full length tip pilin RrgA is composed of four domains, which are aligned much like pearls on a string; Domain D1 is shown in green (N-terminus); domain D2 in yellow, domain D3 in blue and domain D4 in red (C-terminus) (compare Izoré *et al.*, Structure, 2010 [88], RCSB PDB: 2WW8 and SI Fig. S1).

### **2.3.3 Pilus-1 Anchor Protein RrgC**

Full length RrgC (RrgC Fl) harbours three domains (D1 – D3), whose cores display  $\beta$ -barrel folds to which minor secondary structure features (*e.g.*  $\alpha$ -helices) are added [90]. Its approximate dimension is 11 nm x 4 nm and it displays a bended, narrow rod-like shape. D1s fold is comparable with the N-terminal domains of the fimbrial protein FimP from *Actinomyces oris* [106] and GBS52 from *S. agalactiae* [97]. D2 and D3 both fold into anti-parallel  $\beta$ -sheets with high structural similarity and which are reminiscent of the B domain of the collagen-binding adhesin Cna from *S. aureus* [99] and of domains of BcpA, the major pilin of *Bacillus cereus* [103]. In addition, D2 displays structural similarities to the C-terminal domain of GBS52 [97]. Domains D2 and D3 are stabilized by an intramolecular isopeptide bond, respectively, which confer thermal stability and resistance to proteolysis to RrgC [92].

## **3 Atomic Force Microscopy**

The atomic force microscope (AFM) developed in 1986 by Binnig [29] is utilized in many experimental studies in a variety of research fields including biology, physics, and chemistry. Figure 3.1 shows a schematic illustration of a typical AFM setup and the four measurement modes predominantly used in this work. In general, the motion of a flexible AFM cantilever with a sharp pyramidal tip facing towards the sample is tracked by a laser beam which is reflected from the metal coated back side of the lever and detected by a segmented photodiode with nanometer accuracy (Fig. 3.1a). By pushing the tip close to the sample and raster-scanning over it, using a piezo scanner, different modes to image, manipulate or analyze interaction properties of the sample can be carried out.

### **3.1 AFM Imaging**

#### **3.1.1 Contact Force Imaging**

During contact force imaging (Fig. 3.1 b, left side) the AFM tip is moved across the sample surface and a normal force between the tip and the sample is kept constant through a feedback loop. The feedback adjusts the height of the probe (or the cantilever) to restore the predefined force set point. The value of the height movement is equal to the surface topography. Since the tip is in constant contact with the surface, a main drawback of the contact force mode is that significant frictional forces tend to damage or sweep soft samples (*e.g.* polymers or biological macromolecules) on the surface and may distort the features of the generated image. [107, 108]

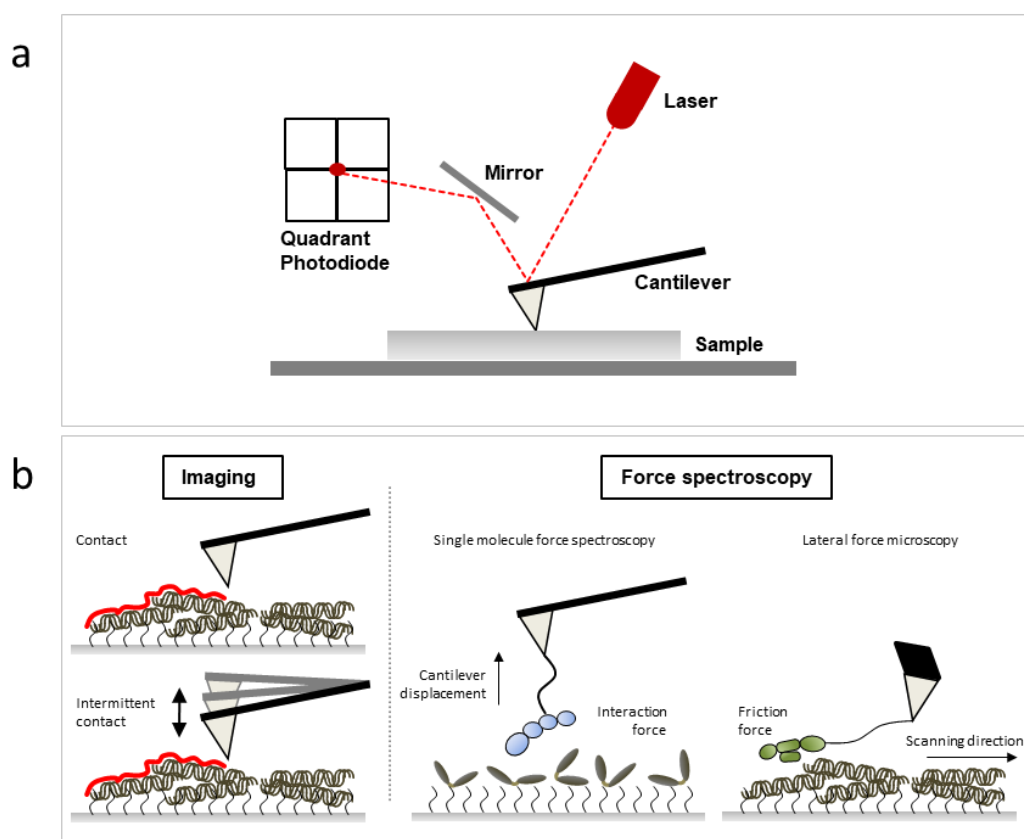


**Figure 3.1: Illustration of an atomic force microscopy setup and typical operation modes.** (a) The motion of a cantilever with the tip facing towards the sample is tracked by a laser beam which is reflected from the lever and detected by a photodiode. By pushing the tip close to and raster-scanning over the sample using a piezo scanner controlled feedback loop different AFM modes can be performed. (b) Typical operation modes are imaging of, and measuring interactions forces with the surface sample.

### 3.1.2 Intermittent Contact Imaging

To image soft samples the intermittent contact mode (Fig. 3.1 b, left side), during which the cantilever scans the sample surface while it oscillates at or near its natural resonant frequency, can be used. The amplitude of vibration, which decreases due to interactions of the tip with the surface, is kept constant through a feedback loop. The adjusted probe (or cantilever) height provides information about the surface topography, similar to the contact mode [107, 108].



## **3.2 Dynamic Single Molecule Force Spectroscopy**

In addition to its high-resolution imaging capabilities, the AFM has emerged as a useful tool to probe molecules with respect to their response to external force and thereby gain insights into many biological and physical processes (Fig 3.1 b, right side) [26, 28, 109, 110]. In contrast to methods like the enzyme linked immunosorbent assay (ELISA), surface plasmon resonance (SPR) or quartz crystal microbalance (QCM) setups, AFM allows to measure interactions on the single molecule (SMFS) [22-25] and single cell level (SCFS) [26-28]. In this case a deflection versus distance curve is generated on a small interaction area as shown in Fig. 3.2, where the cantilever deflection is plotted as a function of the vertical displacement of the piezoelectric scanner (the gained voltage signal can be converted into a force signal, see chapter 3.2.1). If the tip is far away from the surface, no interaction between the tip (or molecules attached to the tip) and the sample is present and the cantilever remains in an undisturbed position (Fig. 3.2, A). As the cantilever is moved towards the sample and the tip-sample separation is reduced beyond a certain point the tip gets into contact with the surface. Once in contact with the sample, the tip remains on the surface and the cantilever will experience an ever-increasing repulsive force which leads to its detectable bending away from the surface (Fig. 3.2, B). As the cantilever is retracted from the surface, the tip or molecules coupled to the tip may remain in contact with the surface, or molecules attached to the surface. Thereby the cantilever is deflected downwards, which, in the presence of flexible molecules, results in a tensile force apparent by the exponential force drop in the retraction force curve (Fig. 3.2, C). At some point the external retraction force is sufficient to overcome the interaction, the tip breaks free from the sample and the cantilever jumps back to its undisturbed position (Fig. 3.2, D) leading to a force peak in the respective force-distance curve (Fig. 3.2, C).

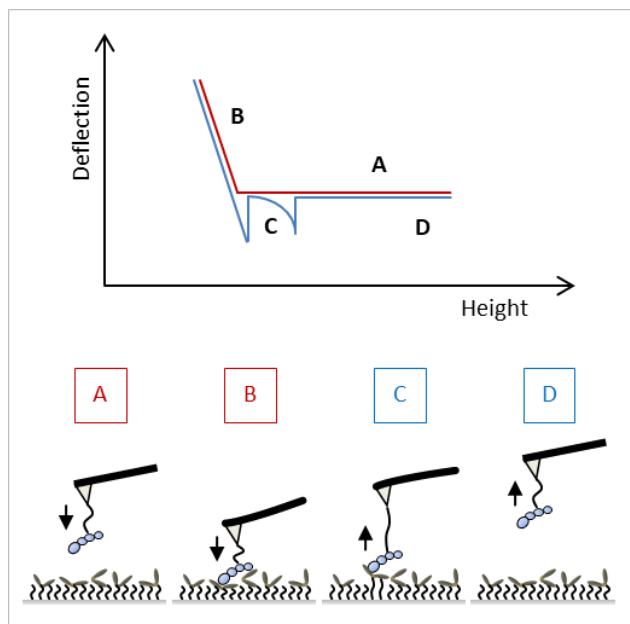


**Figure 3.2: Illustration of a typical force–distance curve recorded during single molecule force spectroscopy experiments.**

The height position of the cantilever is plotted as the x- and its vertical deflection as the y-axis. (A) The probe is away from the surface and the cantilever remains in an undisturbed position. (B) The cantilever is moved towards the sample and the tip gets into contact with the surface and experiences an increasing repulsive force, which leads the lever to bend away from the surface. (C) During retraction from the surface, the tip may remain in contact with the sample and the cantilever is deflected downwards resulting in a change of the slope of the retraction curve. (D) Once the external retraction force is greater as the interactions force, the tip will break free from the sample and the cantilever jumps back to its undisturbed position.

### 3.2.1 Evaluation of Dynamic Force Spectroscopy Experiments

In order to determine the force needed to separate the cantilever tip from the sample surface, the sensitivity and the cantilever spring constant of the optical lever must be recorded. The vertical sensitivity ( $S_n$ ) is the actual deflection for a certain measured change in the photodetector voltage apparent by the slope of the retraction curve in a region where the tip and a hard, non-deformable sample are in contact. Once the deflection (in nm) is known, it can be converted into a force using Hookes' Law

$$F = k \cdot x \quad (\text{Eq. 1})$$

Where  $F$  is the force,  $k$  the spring constant and  $x$  the distance.

The required cantilever spring constant ( $k$ ) can be determined by the thermal noise method introduced by Butt and Jaschke in 1995 [111, 112]. As the cantilever is susceptible to thermal fluctuations, which, for a given temperature, depend on the spring constant of the cantilever,  $k$  can be derived from

$$k = c \cdot \frac{k_b T}{P} \quad (\text{Eq. 2})$$

where  $c$  is a geometrical correction factor [111],  $k_b$  the Boltzmann constant,  $T$  the absolute temperature and  $P$  the integral over the power spectral density (PSD). To calculate the PSD a Lorentzian function is fitted to the first resonance peak in the thermal noise spectrum of the cantilever. In addition to the force conversion, the piezo-height in the force – distance curve needs to be converted to the actual tip-substrate separation. This can be done by subtracting the cantilever deflection from the measured piezo height.

The next step is the fitting of the force peaks in the force – distance curves (Fig. 3.2. C). Assuming that the molecules attached to the cantilever tip and the surface (spacer and proteins) can be physically described as semi-flexible polymers, their stretching in the presence of an external force can be described by the worm-like chain model (WLC) [38], which describes the entropic elasticity of straightening a polymer chain from a random coil configuration (see Fig. 3.3).

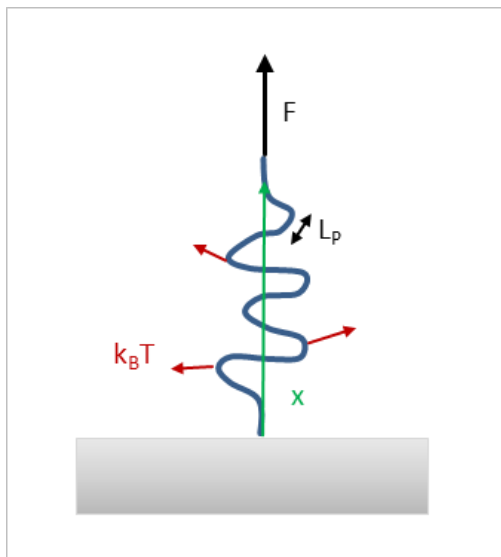


**Figure 3.3: Illustration of the worm-like chain model.** The WLC model describes a continuous, in defined places flexible, isotropic rod stretched by an external force  $F$ .  $k_B$  is the Boltzmann constant,  $T$  the temperature,  $L_p$  the persistence length and  $x$  the end-to-end distance of the polymer.

Including the elasticity of the polymer backbone during stretching at higher forces leads to the extensible worm-like chain model (eWLC) [38-40]

$$f(x) = \frac{k_B T}{L_P} \left[ \frac{1}{4} \left( 1 - \frac{x}{L_C} + \frac{F}{\Phi} \right)^{-2} + \frac{x}{L_C} - \frac{F}{\Phi} - \frac{1}{4} \right] \quad (\text{Eq. 3})$$

where  $k_B$  is the Boltzmann constant,  $T$  the temperature,  $L_P$  the persistence length (which is a measure for the stiffness of the polymer and describes the length over which the direction of the polymer becomes random),  $L_C$  the contour length (which is the total length of the unfolded polymer chain),  $x$  the tip-substrate separation and  $\Phi$  the stretch modulus of the backbone of the molecule. A comprehensible derivation of the WLC models is *e.g.* given by Bouchiat, C., *et al.*, *Biophys. J.*, 1999 [113]. Fitting the rupture peaks present in the force-distance curve with the eWLC model gives, among others, the rupture force, the force-loading rate (see chapter 3.2.2) and the rupture length as indicated in Fig. 3.4.

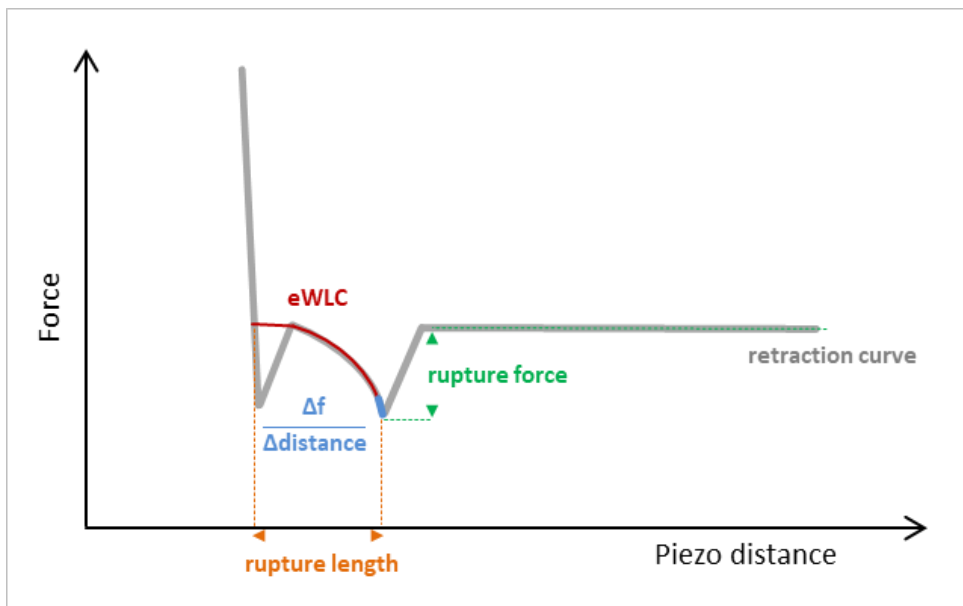


**Figure 3.4: Typical dynamic SMFS force distance curve.**

The deflection signal was converted to a force signal and the height was corrected for the actual deflection of the cantilever. The retraction of the cantilever from the sample surface with one interaction event is shown in grey. Fitting of this rupture event with the eWLC model is displayed in red. The part  $(\Delta f / \Delta \text{distance})$  used by the eWLC fit to calculate the force-loading rate is marked in blue, the rupture length in orange and the rupture force in green.

### 3.2.2 Kinetics of Force Induced Bond Rupture

Receptor-ligand bond dissociation is in general a time-dependent process driven by thermal fluctuation (Fig. 3.5 a). The bond rupture can be approximated by a thermally activated, spontaneous escape over a finite energy barrier ( $\Delta G^\ddagger$ ) within the progression of the Gibbs free energy  $G(x)$  along a one-dimensional reaction coordinate ( $x$ ) [41, 114-116]:

$$k_{off}^0 = \omega^0 e^{-\frac{\Delta G^\ddagger}{k_b T}} \quad (\text{Eq. 4})$$

where  $k_{off}^0$  is the reaction rate constant,  $\omega^0$  a constant of proportionality describing the attempt frequency of the system,  $\Delta G^\ddagger$  the activation energy and  $k_b T$  the thermal energy with  $k_b$  the Boltzmann constant and  $T$  the absolute temperature.

If an external force ( $-f\Delta x$ ) is applied to a receptor-ligand complex, the potential  $G(x)$  is deformed [42] by the additional mechanical energy (stored in the cantilever and the stretched polymers - Fig. 3.5 b) to the effective potential  $G_{eff}(x)$  and the activation energy is lowered to  $\Delta G^\ddagger(f)$ .

$$\Delta G^\ddagger(f) = \Delta G_0^\ddagger - f \cdot \Delta x \quad (\text{Eq. 5})$$

Here  $\Delta G_0^\ddagger$  is the activation barrier without force and  $\Delta x = x - x_0$  is the barrier distance with  $x$  is the direction of the force and  $x_0$  the position of the minimum. As a consequence the force-dependent reaction rate constant  $k_{off}(f)$  becomes

$$k_{off}(f) = \omega^0 \cdot e^{-\frac{\Delta G^\ddagger(f)}{k_b T}} = k_{off}^0 \cdot e^{\frac{f \cdot \Delta x}{k_b T}}. \quad (\text{Eq. 6})$$

The strength of a receptor-ligand bond depends on the temporal evolution of the force  $f$  which grows nearly linear with time in SMFS experiments with constant retraction velocity

$$\Delta G^\ddagger(t) = \Delta G_0^\ddagger - r \cdot t \cdot \Delta x \quad (\text{Eq. 7})$$

## Atomic Force Microscopy

---

Where  $r = \left(\frac{df}{dt}\right)$  is the force-loading rate.

With the assumption that other external forces (e.g. rebinding) are negligible the probability  $P(t)$  that the bond under an external force is intact at the time  $t$  can be determined by a first-order Markov process for thermally activated bond dissociation:

$$\frac{dP(t)}{dt} = -k_{off}(f) \cdot P(t) = -\omega^0 \cdot e^{-\frac{\Delta G_0^\ddagger - r \cdot t \cdot \Delta x}{k_b T}} \cdot P(t) \quad (\text{Eq. 8})$$

The solution of Eq. 8 with  $P(t = 0) = 1$  yields

$$P(t) = \exp\left[\frac{\omega^0 \cdot k_b T}{r \cdot \Delta x} \cdot e^{-\frac{\Delta G_0^\ddagger}{k_b T}} \cdot \left(1 - e^{\frac{r \cdot t \cdot \Delta x}{k_b T}}\right)\right]. \quad (\text{Eq. 9})$$

With this, a distribution of dissociation times  $t_D$  at a defined loading rate  $r$  and subsequent a distribution of dissociation forces with  $t_D \cdot r = f_D$  is obtained as follows

$$p(f_D)df_D = -\left.\frac{dP(f)}{df}\right|_{f_D} df_D = \omega^0 \cdot e^{-\left(\frac{\Delta G_0^\ddagger - f_D \cdot \Delta x}{k_b T}\right)} \exp\left[\frac{\omega^0 \cdot k_b T}{r \cdot \Delta x} \cdot e^{-\frac{-\Delta G_0^\ddagger}{k_b T}} \cdot \left(1 - e^{\frac{f_D \cdot \Delta x}{k_b T}}\right)\right] df_D. \quad (\text{Eq. 10})$$

The most probably dissociation/rupture force  $f_{MP}$  is given by the maximum of Eq. 10

$$f_{MP} = \frac{\Delta G_0^\ddagger}{\Delta x} + \frac{k_b T}{\Delta x} \cdot \ln\left(\frac{r \cdot \Delta x}{k_b T \omega^0}\right) \quad (\text{Eq. 11})$$

Using Eq. 4 leads to the one decay channel model proposed by Evans and Ritchie [42, 117, 118]

$$f_{MP} = \frac{k_b T}{\Delta x} \cdot \ln\left(\frac{r \cdot \Delta x}{k_b T \cdot k_{off}^0}\right). \quad (\text{Eq. 12})$$

The relationship between the most probably dissociation force  $f_{MP}$  and the force-loading rate  $r$  is the basis of dynamic force spectroscopy and describes that  $f_{MP}$  increases logarithmically with  $r$ . To obtain  $k_{off}^0$  the retraction velocity (and thus  $r$ ) needs to be varied over several orders of magnitude during SMFS experiments (see an example in the supplement information (SI) Fig. S7). The loading-rate plotted semi-logarithmically against the respective most likely dissociation force results in a linear dependence (Fig.3.5 c). The slope of the resulting regression line gives  $\Delta x$  and by extrapolating to  $f_{MP} = 0$ ,  $k_{off}^0$  and the bond lifetime at zero force

$$\tau_0 = \frac{1}{k_{off}^0} \quad (\text{Eq. 13})$$

can be obtained.

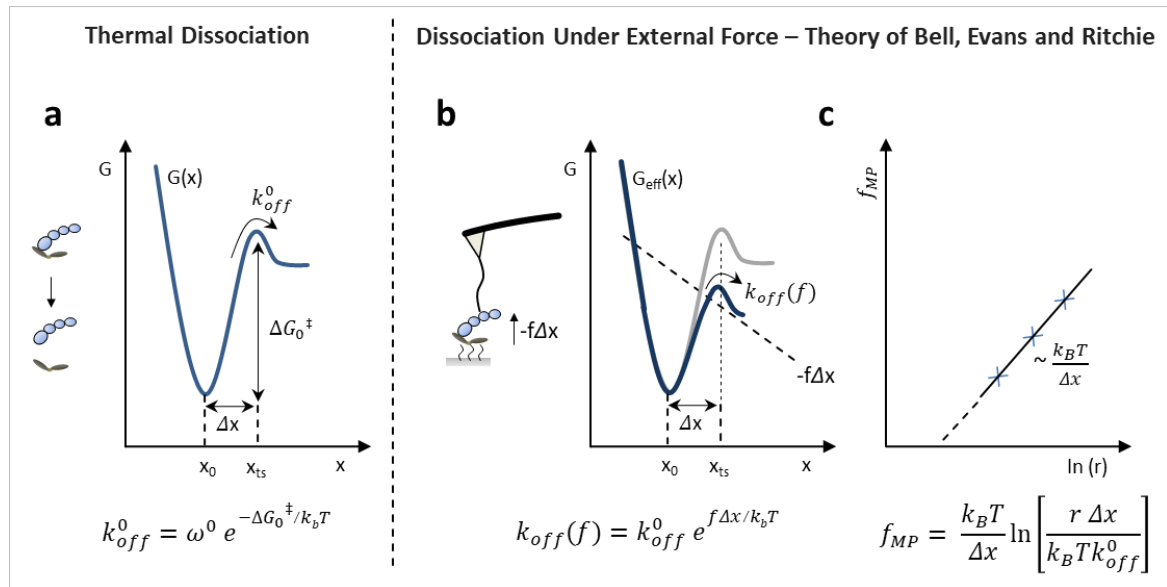


**Figure 3.5: Schematic representation of a single-well potential curve without ( $G(x)$ ) and under external force ( $G_{eff}(x)$ ).**

(a) Undisturbed potential curve as proposed by Bell [41]. Bond separation is seen as a thermal activated, spontaneous escape over an energy barrier  $\Delta G_0^\ddagger$  along the distance between the potential minimum  $x_0$  and the transitions state  $x_{ts}$ . (b) Effective potential curve with an external force and a fixed barrier distance  $\Delta x$ . The additionally applied mechanical energy ( $-f \cdot \Delta x$ ), which is stored in the AFM cantilever and the stretched molecules, leads to the deformation of the undisturbed potential and to a force-dependent reaction rate constant  $k_{off}(f)$ . (c) Based on the assumptions of Bell [41] and following the theoretical model by Evans and Ritchie [42], the most probable rupture force  $f_{MP}$  increases logarithmically with increasing force-loading rate  $r$ . The barrier distance  $\Delta x$  can be obtained from the slope of the graph and the reaction rate constant  $k_{off}^0$ , and subsequently the bond lifetime at zero force, by determining the interception point of the x-coordinate.

One should keep in mind that the Bell-Evans-Ritchie model is a frequently used model, but for certain cases does not provide satisfactory description of the unbinding of receptor ligand complexes. For example, bond relaxation and rebinding are neglected, even if there is the probability that reversible binding can occur, particularly at lower force-loads. Addressing this problem, the Friddle-de-Yoreo model [119] describes two phases, an equilibrium phase at lower pulling velocities where the molecules can rebind, and a kinetic phase at higher loading rates where molecules unbind irreversibly. Dudko, Hummer & Szabo [120, 121] on the other hand, proposed a theory similar to the Bell-Evans-Ritchie model, but with an additional parameter to smoothly interpolate between different shapes of the energy landscapes. This allowed to interpret cases with multiple energy barriers. Until today the models are evolving to encompass the diversity of protein-protein interactions.

### **3.3 Lateral Force Microscopy**

During lateral force microscopy (LFM) experiments the cantilever tip is brought into contact with and scanned over the sample surface in the direction perpendicular to the long cantilever axis (see Fig 3.1 b, right side and Fig. 3.6) [43, 122]. This leads to lateral forces which derive from the collective and interdependent mechanical behavior of a multitude of small contacts between the shearing surfaces, which are constantly being formed, deformed, and ruptured. As illustrated in figure 3.6, when the tip starts sliding with respect to the sample, the lateral force acting on the tip can be recorded as a twisting of the cantilever, which results in a deflection of the laser beam in lateral direction. In addition to SMFS, LFM leads to another perspective on the binding behavior of molecules under external force and can thereby extend the knowledge of biological and biomechanical processes.



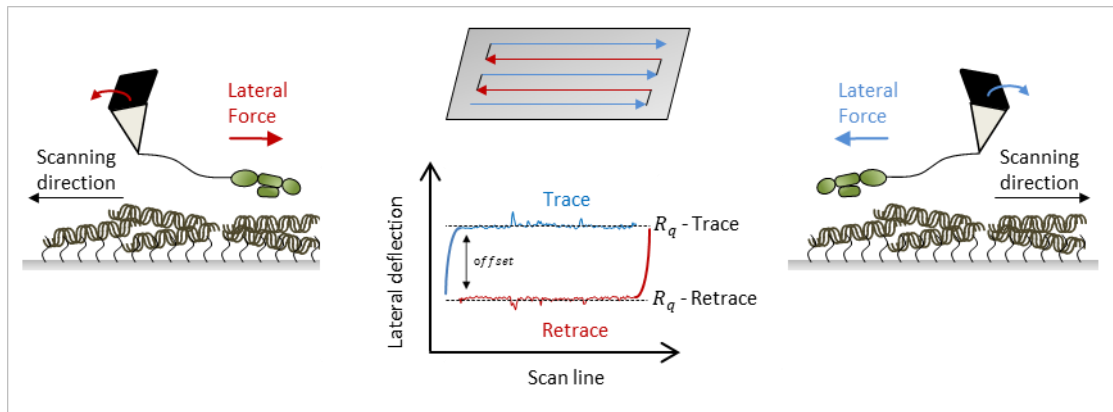


**Figure 3.6: Schematic representation of lateral force microscopy experiments.**

The cantilever tip is scanned over the sample surface in the direction perpendicular to the long cantilever axis while a predefined contact force is kept constant. Thereby lateral forces arise from the interactions between the sliding surfaces, which results in a torsion of the cantilever in lateral direction. Usually the lateral offset is used to determine the friction force established between the tip and the substrate. To eliminate interactions between the tip and the substrate, the lateral photocurrent  $I_l$  can be determined with the root mean squared roughness  $R_q$  from trace and retrace lateral deflection images (see chapter 6.2.7)

### 3.3.1 Evaluation of Friction Force Experiments

A number of methods have been proposed for the calibration of the photodiode response to lateral cantilever deflection and the subsequent calculation of lateral forces acting on the lever beam. During raster-scanning a sample with a constant applied force, the lateral force is defined by the lateral force constant  $k_l$  of the cantilever and its implementation in Hookes' Law (Eq. 1):

$$F_l = k_l \cdot x_l \quad (\text{Eq. 14})$$

A simple access to  $k_l$  is given by the beam mechanics, which is defined for a cantilever with rectangular cross section [43-45, 123, 124] as

$$k_l = \frac{Gwt^3}{3l(h + \frac{t}{2})^2} \quad (\text{Eq. 15})$$

Where  $G$  is the shear modulus,  $w$  the width,  $t$  the thickness and  $l$  the length of the cantilever and  $h$  the height of the tip as illustrated in figure 3.7.

Combining Eq. 14 and 15 leads to

$$F_l = \frac{Gwt^3}{3l(h+\frac{t}{2})^2} \cdot S_l \cdot I_l \quad (\text{Eq. 16})$$

where  $S_l$  is the lateral sensitivity of the photodiode and  $I_l$  the lateral photocurrent which is apparent from the lateral deflection scan as illustrated in figure. 3.6. Furthermore the same distance in the normal ( $x$ , see Eq. 1) or lateral direction  $x_l$  of a bent cantilever, results in different angular cantilever deflections ( $\theta_n$  and  $\theta_l$ , see figure 3.7). Based on the beam mechanics  $\theta_n$  and  $\theta_l$  are related to one another by

$$\theta_l = \frac{E(h+\frac{t}{2})}{2Gl} \cdot \theta_n \quad (\text{Eq. 17})$$

where  $E$  is the Young's modulus.

With the simplified assumption that the sensitivity of the lateral photodiode  $S_l = \theta_l \cdot I_l$  is proportional to the sensitivity of the normal photodiode  $S_n = \theta_n \cdot I_n$  (see chapter 3.2.1)

[43]  $S_l$  can be expressed as

$$S_l = \frac{E(h+\frac{t}{2})}{2Gl} \cdot S_n \quad (\text{Eq. 18})$$

and the lateral force can be calculated *via*

$$F_l = \frac{Ewt^3}{6l^2(h+\frac{t}{2})} \cdot S_n \cdot I_l. \quad (\text{Eq. 19})$$

The Young's modulus of silicon nitride ( $\text{Si}_3\text{N}_4$ ) cantilever depends on the temperature and the thickness of the beam. Reported values for the Young's modulus range from *e.g.* 186 GPa for triangular cantilevers [43], 220 GPa for micro-cantilever beams [125], 290 GPa for low-pressure chemical-vapor deposition silicon nitride thin films [126] and 300 GPa for rectangular silicon nitride cantilever thicker than 150 nm [127].

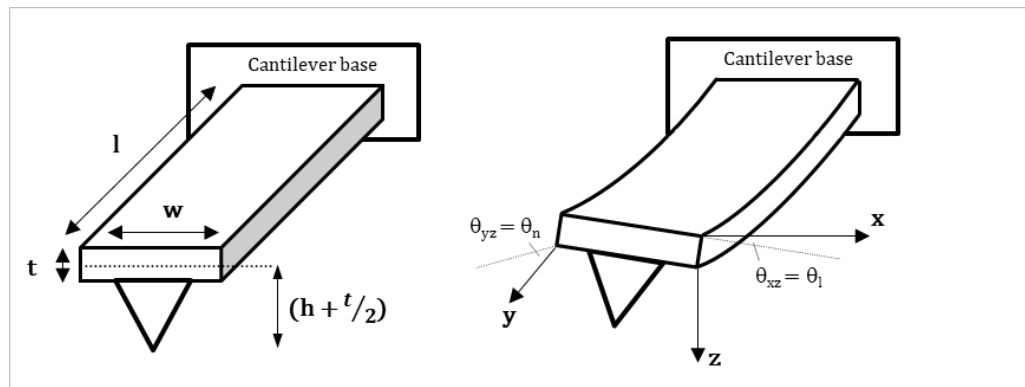


**Figure 3.7: Illustration of the cantilever geometry.**

The AFM cantilever is fixed on one side. If the other side is subjected to force, the beam can bend in vertical and lateral directions.  $l$  is the length,  $w$  the width and the  $t$  thickness of the cantilever,  $h$  the height of the tip.  $\theta_n$  and  $\theta_l$  reflect the angular cantilever deflections caused by forces in vertical and lateral direction.

In addition to the uncertainty in the Young's modulus, the calculation of the lateral force with the beam mechanic method is approximate in the sense that it uses simplified models of the cantilever (*e.g.* ideal geometry, bulk elastic properties, uniform thickness, neglecting of coatings *etc.*) and that it assumes a "rotationally symmetric" photodiode (symmetric laser spot shape, no diffraction effects from the cantilever, no cross talk between the signals for normal and torsional bending).

A number of alternatives to the beam mechanics model have been proposed and are still evolving. A particularly elegant method to calibrate LFM experiments is the analysis of friction loops, *i.e.* lateral force curves from forward and backward scans, recorded across surfaces with well-defined wedges [128-130] or the measurement of the friction force applied by the cantilever's tip to a flat surface of a micro-force sensor measuring beam [131].

### 3.4 Surface Immobilization Strategy

The following chapter contains sections and figures from the article

#### **“Covalent Immobilization of Proteins for the Single Molecule Force Spectroscopy”**

by Tanja D. Becke, Stefan Ness, Stefanie Sudhop, Hermann E. Gaub, Markus Hilleringmann, Arndt F. Schilling, and Hauke Clausen-Schaumann

Published: Journal of Visualized Experiments, 2018, (138).

DOI: 10.3791/58167 [132]

“The success of SMFS [and lateral force] experiments critically depends on the functional and native immobilization of the biomolecules on solid surfaces and AFM tips. As high forces may occur during [...] [interaction] measurements, the proteins should preferably be covalently coupled to the surface. There are a large number of different coupling methods for immobilization of proteins and other biomolecules, as well as whole cells on (inorganic) solid surfaces, nano- particles and other devices described in the literature [110, 133-144]. These protocols often make use of hazardous substances, are difficult to perform and/or require special equipment (*e.g.* plasma cleaner). A simple way to couple molecules to *e.g.* glass is to attach a thicker polymer layer of heterobifunctional crosslinkers with a silane-reactive group on one side and an amine-reactive group on their other side. Depending on the application, the coupling agents can comprise flexible hydrocarbon chains of variable length, *e.g.* polyethyleneglycol (PEG). They suppress non-specific interactions of the modified surfaces (*e.g.* hydrophobic, electrostatic and van-der-Waals interactions) and may provide the coupled molecule rotational freedom.

[...][In this work, the] protocol for the covalent coupling of proteins containing one or more free amino groups (-NH<sub>2</sub>) to glass surfaces and silicon nitride AFM tips *via* a heterobifunctional ethoxy silane-PEG-carboxyl (-COOH) [is used (see Fig. 3.8 for an overview and chapter 6.2.5 and SI 10.2.2 for a detailed protocol)].[...]. The first step is the silanization of the surface [145-148]. It involves the hydrolysis of the ethoxy groups of the coupling agent in order to form highly reactive SiOH groups.

These can react with SiOH groups on the substrate. In a primary condensation step, these silanols form hydrogen bonds and spread on the substrate. In a secondary condensation reaction (which usually requires heat or vacuum to remove water) siloxane bonds are formed. This results in a covalently attached organo-silane layer. The second step is the coupling of the proteins to the functional (-COOH) groups which extend from the polymer [149]. First, the acid is converted to a reactive N-Hydroxysuccinimid (NHS) ester intermediate, which is gained through the well-established NHS/EDC (1-Ethyl-3-(3-dimethylaminopropyl)carbodiimid chemistry [150] and undergoes nucleophilic substitution to finally form an amide bond with primary amines on the proteins.[...].

The surface chemistry is well established and analyzed and similar approaches have been successfully used in multiple SMFS experiments [134, 151-154]. The silylether used for coupling the silane polymer to the surface, is subject to hydrolysis, which depends on the amount of formed siloxane. If high interaction forces ( $\geq 1000$  pN) are expected during SMFS measurements, the silanization should be performed *via* vapor-phase deposition [147] which results in the formation of a continuous layer of siloxanes. As for many experiments (*e.g.* many protein – protein interactions) the interaction forces are in the range of a few hundred pN, the described procedure, in which siloxane formation is carried out by deposition from an aqueous phase and thoughtfully washing off unbound organo-silanes with ethanol [...] followed by curing with heat [...][(110 °C)], is sufficient. [...].

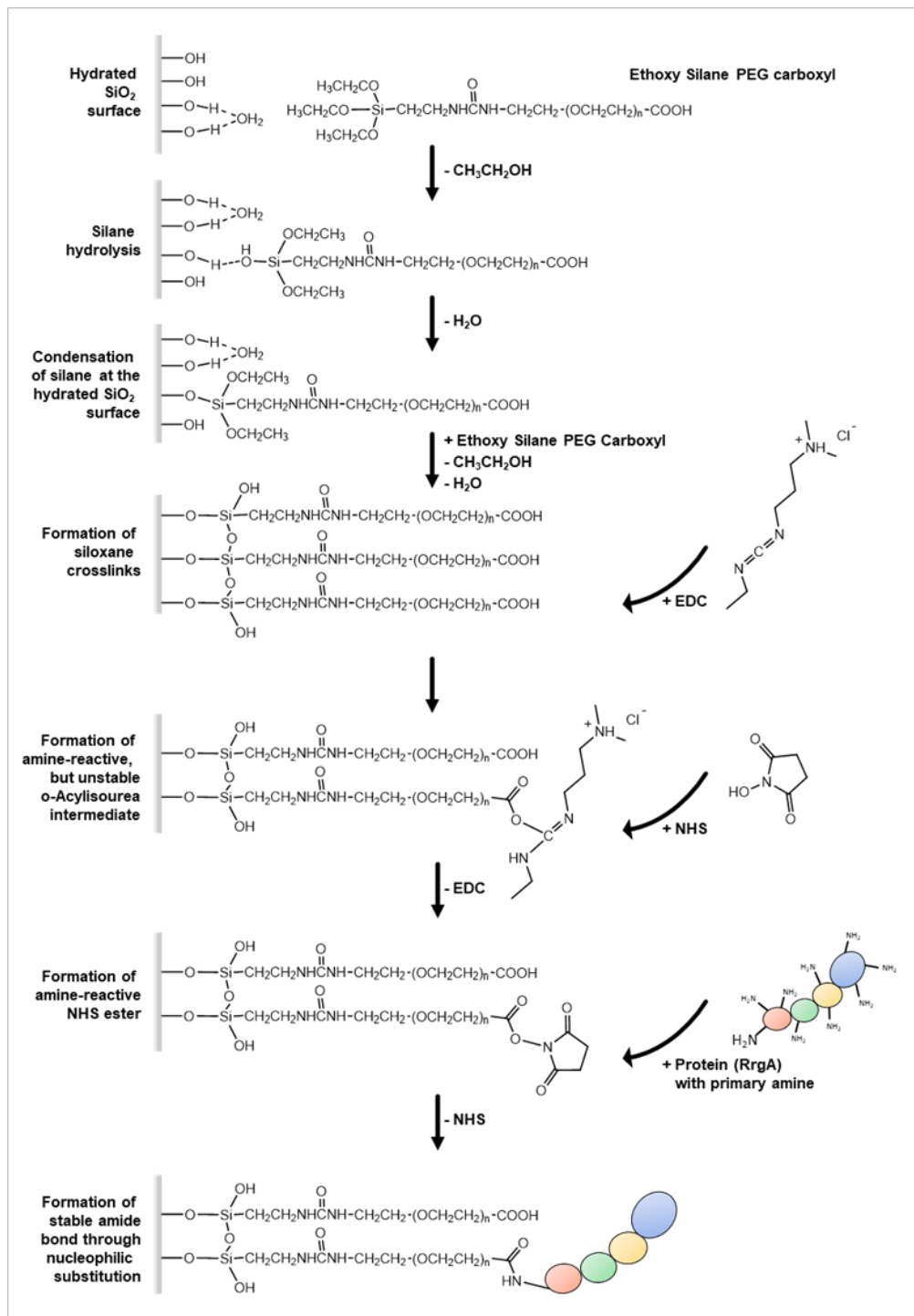


**Figure 3.8: Overview over the surface chemistry.**

The hydrolysis of ethoxy silane-PEG-carboxyl is followed by its condensation at the hydrated glass surface and formation of siloxane crosslinks. The reaction of EDC with the carboxyl groups results in a reactive o-Acylisourea, an amine-reactive intermediate with an extremely short half-life in aqueous solution (hydrolysis). The intermediate is stabilized by the formation of an NHS ester, which undergoes nucleophilic substitution to finally form an amide bond with primary amines on the proteins. The figure has been adapted from Becke *et al.*, JoVE, 2018 [132].

Another elegant way to control the amount of molecules coupled to the sample substrate and cantilever tip besides varying the protein concentration and/or incubation times, is the combination of silane-agents with different secondary functional groups. By changing the ratio of protein reactive groups extending from the PEG-polymer, the number of immobilized proteins can be controlled [135, 137]. The protocol described here can also be used to immobilize other  $-NH_2$  containing molecules or be adjusted to couple proteins to other silicon-oxide surface besides glass and silicon nitride. Depending on the protein design, the amine reactive carboxyl group can be changed to a sulfhydryl reactive group (*e.g.* maleimide or ortho-pyridyl disulfide) to couple the protein *via* its free  $-SH$  group which results in a predefined orientation [105, 133, 136]. In summary, this protocol can be adjusted to serve different requirements and is suitable for other biophysical applications besides single molecule force spectroscopy experiments.”





## 4 Recent Single Cell and Single Protein work

The following chapter contains sections from the article

### **“Single Molecule Force Spectroscopy Reveals Two-Domain Binding Mode of Pilus-1 Tip Protein RrgA of *Streptococcus Pneumoniae* to Fibronectin”**

by Tanja D. Becke, Stefan Ness, Raimund Gürster, Arndt F. Schilling, Anne-Marie di Guilmi, Stefanie Sudhop, Markus Hilleringmann, and Hauke Clausen-Schaumann

Published: ACS Nano, 2018, 12 (1), pp 549–558

DOI: 10.1021/acsnano.7b07247 [105]

“In recent years [...] [AFM] based force spectroscopy on the single molecule and single cell level has provided new insights into the binding mechanisms of numerous bacterial adhesins [30, 155-158], such as, pilus proteins of *Pseudomonas aeruginosa* [30, 31], *Neisseria gonorrhoeae* [32], and *Escherichia coli* [33, 34], the large adhesion protein of *Pseudomonas fluorescens* [159], and adhesion molecules of *Lactobacillus rhamnosus* [26, 109], *Lactobacillus reuteri* [160], *Streptococcus pyogenes* [161], *Streptococcus mutans* [162], *Streptococcus agalactiae* [163], and *Staphylococcus epidermis* [27, 164]. For *S. aureus*, binding to host cell and ECM proteins, as well as biofilm formation *via* cell-cell interaction have been investigated [28, 165-175]. Some bonds, such as the SdrG – fibrinogen [164] or the Cna – collagen bond [171], withstand remarkably high forces, close to rupture forces of covalent bonds [152], which has been explained by ligand-binding induced conformational transitions in the adhesion molecules, such as the “dock, lock, and latch” mechanism for SdrG–fibrinogen or the “collagen hug” for Cna - collagen [176, 177]. By applying a prestress to the bond between the *E. coli* pilus protein FimH and mannose, Yakovenko *et al.* elegantly demonstrated that mechanical stress converts this “catch bond” to a tight binding conformation, showing that the binding mechanism is mechanically controlled through allosteric regulation [178, 179]. Other examples of bacterial adhesion proteins that strengthen in response to mechanical stress in a “catch-bond” like manner are the adhesion complex of the *Ruminococcus flavefaciens* cellulosome [180], and clumping factor B of *Staphylococcus*

*aureus* when interacting with loricin [137]. Several studies have addressed the binding strengths of the Fn binding proteins FnBPa and FnBPb of *S. aureus* [165, 166, 168, 169, 172], because Fn is not only abundant in the ECM and in blood plasma but also and is found on implanted medical devices, such as cardiovascular prostheses. For strains isolated from patients with infected cardiovascular implants, bond strengths and lifetimes were significantly higher, compared to strains from patients with uninfected implants. This has been attributed to elevated expression levels of FnBPb and to polymorphisms in the high affinity Fn-binding regions FnBR-5 and FnBR-9 of FnBPa [172, 181]. Higher binding forces of mutant polypeptides mimicking the tandem  $\beta$ -zipper repeat FnBR-9 have confirmed this hypothesis [165, 166, 172]. These findings are also consistent with polymorphisms observed in the FnBR-9, FnBR-10, and FnBR-11 regions of FnBP in methicillin-resistant *S. aureus* strains isolated from patients with persistent bacteremia, which form stronger bonds to Fn than strains from patients with resolving bacteremia [169]. Finally, elevated levels of the transcription factor SigB in *S. aureus* strains isolated from cystic fibrosis patients lead to increased expression of FnBPa and increased Fn-adhesion rates and Fn-binding forces [167].”

In summary, the expansion of standard protein binding essays with AFM based force spectroscopy (and lateral force microscopy) can give new perspectives regarding the mechanics of protein – protein - interactions and may pave the way towards an overall understanding of how pathogens can colonize and invade host tissue and trigger serious diseases.

## **5 Aim of the Work**

In this thesis single molecule force spectroscopy and lateral force microscopy are used to investigate the binding of the individual pilus-1 proteins to fibronectin and collagen I to answer the question if pneumococcal pilus-1 mediated interaction with host factors allow specific pneumococcal adherence.

Pneumococcal infection can be initiated by the adherence of the bacteria to eukaryotic surfaces and the host cell surrounding matrices. Surface piliation thus procures benefits for the pathogen, and a detailed understanding of how pili adhere to host cells as well as host ECM is a key aspect in understanding their role during infection. Besides a plurality of other surface anchored adhesins, *Streptococcus pneumoniae* TIGR 4 is capable of expressing pilus-1 consisting of three different pilus subunits. Distal adhesive tip molecule RrgA shows dose dependent binding to several host factors including members of the extra cellular matrix like fibronectin and collagen I. However for backbone protein RrgB and cell wall anchor protein RrgC no specific binding to host surfaces has been reported so far. In particular, no data is available describing binding forces of pilus-1 mediated host factor association, which is a critical parameter because efficient pilus mediated host interaction has to resist shear forces originating from innate mechanical removal strategies.



## 6 Material and Methods

### 6.1 Material

#### 6.1.1 Materials and Chemicals

Material, Chemical	Company	Comment
1-(3-dimethylaminopropyl)-3-ethylcarbodiimide	Sigma-Aldrich	EDC
Acetic acid	Carl Roth	Analytical purity
Acrylamide	AppliChem	30%
Alkaline Phosphatase Substrate	Thermo Fisher Scientific	pNPP (p-nitrophenyl phosphate)
Ammoniumpersulfate	AppliChem	APS
Ampicillin sodium salt	Fluka	
Arabinose	Carl Roth	
Blotting membrane	Sartorius	0.45 $\mu$ m nitrocellulose
Blotting paper	Sartorius	Type BF 4
Di-Ethanolamine	AppliChem	
Ethanol	Carl Roth	Analytical purity
Ethoxy silane polyethylene glycol acid	Nanocs	5 kDa; COOH-PEG-Si(OC <sub>2</sub> H <sub>5</sub> ) <sub>3</sub>
Hydrochloric acid	Carl Roth	32%
Imidazole	AppliChem	
Isopropyl- $\beta$ -d-thiogalactopyranoside	Carl Roth	IPTG
Milk powder	AppliChem	
N,N,N',N'-Tetramethylethylenediamine	AppliChem	TEMED
N-Hydroxysuccinimid	Merck	NHS; for synthesis
NuPAGE LDS Sample Buffer	Life Technologies	4x
NuPAGE MOPS SDS Running Buffer	Life Technologies	20x
NuPAGE Sample Reducing Agent	Life Technologies	10x
NuPAGE Transfer Buffer	Life Technologies	20x
Phosphate buffered saline	Sigma-Aldrich	PBS – tablets

## Material and Methods

Material, Chemical	Company	Comments
Ponceau S	AppliChem	
SeeBlue Pre-Stained Plus 2	Life Technologies	
SeeBlue Pre-Stained Standard	Life Technologies	
SimplyBlue SafeStain	Life Technologies	
Sodium chloride	AppliChem or Carl Roth	NaCl
Tris(hydroxymethyl)-aminomethan	AppliChem or Carl Roth	TRIS; Buffer Grade
Tryptone soya broth	AppliChem	CASO-Buillon
Tween 20	AppliChem	
Western Blue Stabilized Substrate for Alkaline Phosphatase	Promega	

### 6.1.2 Proteins and Antibodies

Protein, Antibody	Company	Comment
Anti-Rabbit IgG (Fc)	Promega	
Anti-RrgA Antibody	Intern	Rabbit
Anti-RrgB Antibody	Intern	Rabbit
Bovines serum albumin	Sigma-Aldrich or PAA	BSA
Collagen I	Sigma-Aldrich	Col I; human placenta
Fibronectin	Sigma-Aldrich	Fn; human plasma
RrgA Fl	Intern	
RrgA domain D1	Intern	
RrgA domain D2	Intern	
RrgA domain D3	Intern	
RrgA domain D4	Intern	
RrgB Fl	Intern	
RrgC Fl	Intern	

### 6.1.3 Strains and Plasmids

Strain, Plasmid	Company	Comment
<i>Escherichia coli</i> BL21 De3-RIL	NEB	
<i>Escherichia coli</i> Top 10	Invitrogen	
pETDuet-1	Intern	
pBAD	Thermo Fisher Scientific	

#### 6.1.4 Equipment

<b>Equipment</b>	<b>Company</b>	<b>Comment</b>
JPK NanoWizard 1	JPK Instruments	
Äkta avant 25	GE Healthcare	
Column HisTrap HP	GE Healthcare	1 ml
Column Superdex 200 10/300 GL	GE Healthcare	
Column Superdex 75 10/300 GL	GE Healthcare	
Digital control bath HAAKE DC30-K20	Thermo Scientific	
Dual Gel Caster	GE Healthcare	
Electrophoresis System	Hoefer, Inc.	SE260 and SE250
MaxiSorp flat bottom	Nunc	96-well plate
NanoDrop One™	Thermo Scientific™	
Novex Semi-Dry Blotter System	Life Technologies	
Silicon nitride cantilever	Bruker AXS S.A.S	MLCT
Sonicator HD2070	Bandelin	
Tensor 27	Bruker	CONFOCHECK, Bio-ATRII™, Si crystal
UV PenRay	UVP, LLC	Mercury spectrum primary energy at 254 nm
XCell SureLock Mini-Cell	Life Technologies	

#### 6.1.5 Software

<b>Software</b>	<b>Company</b>
Äkta avant 25 Software UNICORN 6	GE Healthcare
ChemDraw® 11.	Cambridgesoft
Excel	Microsoft
Igor pro 6.3	Wavemetrics
JPK NanoWizard SPM and DP software	JPK Instruments
OPUS 6.5 software	Bruker





## 6.2 Methods

### 6.2.1 Protein Expression and Purification<sup>1</sup>

For heterologous expression, genes encoding full length and individual RrgA domains (D1, D2, D3, and D4, SI Fig. S1) were cloned into pETDuet-1 expression vectors<sup>2</sup> and transformed in chemically competent *Escherichia coli* (BL21 De3-RIL) applying standard heat shock protocols with 5 ng of the respective plasmid, 100 µg ml<sup>-1</sup> Ampicillin and a 10 sec heat shock. Gene encoding full length RrgB (SI Fig. S2) was cloned into pBAD expression vector and transformed in chemically competent *Escherichia coli* (Top 10) applying the same heat shock procedure as for pETDuet-1 vectors and BL21 De3-RIL cells with a 30 sec heat shock.. Expression of RrgA FI, individual domains and RrgB FI was performed as described before [21] with minor modifications: Individual *E. coli* strains were cultivated in LB medium (3 % Trypton Soya broth, 37 °C) supplemented with 100 µg mL<sup>-1</sup> ampicillin. For RrgA FI and domains protein expression was induced at an optical density OD 600 of around 1.0 by adding a final concentration of 0.5 mM IPTG (isopropyl-β-d-thiogalactopyranoside). To avoid inclusion body formation, growth temperature during overnight-induction was reduced (25 and 15 °C, for RrgA FI and RrgA domains, respectively). For RrgB FI protein expression was induced by adding a final concentration of 0.1 % Arabinose at an optical density OD 600 of around 0.4 and overnight growth by 37°C.

Cells were harvested by centrifugation (20 min, 3000 rpm, 4 °C), and the protein containing pellets were resuspended in 10 ml of buffer containing 50 mM Tris HCl, 150 mM NaCl, pH 8.0 at 4 °C. Ultrasonic cell disruption was performed on ice applying an amplitude of 70 % and an interval of 0.5 s. for 2 × 10 min (Sonicator HD2070, Bandelin). Following another centrifugation step (20 min, 4 °C), the supernatant was sterile-filtrated and subjected to an immobilized metal chelate affinity chromatography (IMAC, HisTrap HP column). IMAC exploiting N-terminal 6 × His TAG sequences of respective protein

---

<sup>1</sup> Protein expression and purification was mainly performed by Stefan Ness, M.Sc. (FG Protein Biochemistry & Cellular Microbiology, Munich University of Applied Sciences, 80335 Munich, Germany).

<sup>2</sup> Plasmids used for the heterologous expression of the individual RrgA constructs were ceded by Anne-Marie Di Guilmi (DRF/IRCM/SIGRR/LRIG, 92265 Fontenay-aux-roses Cedex, France).

## **Material and Methods**

---

constructs was carried out on an Äkta Avant 25 System (GE-Healthcare) according to the manufacturer purification protocol (see SI 10.2.1). Polishing of protein containing fractions was performed using a Size-Exclusion-Chromatography step (Superdex 75 10/300 GL or Superdex 200 10/300 GL column for RrgA domains or RrgA FI and RrgB FI, respectively, with Äkta Avant 25 System, GE-Healthcare, see SI 10.2.1) and proteins were stored in phosphate-buffered saline (PBS; 137 mM NaCl, 2.7 mM KCl, 10 mM Na<sub>2</sub>HPO<sub>4</sub>, 1.8 mM KH<sub>2</sub>PO<sub>4</sub>, pH 7.4). Respective protein concentrations were measured at 280 nm (NanoDrop One™). RrgC FI was provided as purified sample and dialyzed in PBS.

### **6.2.2 Protein Analysis**

#### **SDS-PAGE<sup>3</sup>**

Purity of final protein samples was determined by standard sodium dodecyl sulfate polyacrylamide gel electrophoresis (SDS PAGE, SI Fig.S3 and S4) using a SDS running gel containing 13.5 % acrylamide dissolved in NuPAGE MOPS SDS running buffer supplemented with, 0.05% (w/v) Ammoniumpersulfate (APS) and 0.16 % N,N,N',N'-Tetramethylethylenediamine (TEMED) and a 5 % acrylamide stacking gel. Protein samples were prepared based on standard protocols using NuPAGE LDS sample buffer and NuPAGE sample reducing agent with a final protein concentration of around 0.5 µg per gel band. All SDS-PAGE's were carried out at 220 Volts constant. Coomassie staining was done using a standard microwave procedure.

#### **Semi-dry western blotting<sup>3</sup>**

Standard western blot analysis using polyclonal anti-RrgA and anti-RrgB antibodies confirmed identity of the purified RrgA FI and its single domains D1, D2, D3 and D4, as well as of RrgB FI, respectively (SI Fig. S3 and S4). Therefore the SDS-PAGE gel was washed two times for 15 min in NuPAGE transfer buffer and placed together with a nitrocellulose

---

<sup>3</sup> Photometric determination of protein concentration, SDS-PAGE and WESTERN blot analysis was mainly performed by Stefan Ness, M.Sc. (FG Protein Biochemistry & Cellular Microbiology, Munich University of Applied Sciences, 80335 Munich, Germany)

membrane between blotting papers (membrane and blotting paper soaked in transfer buffer). The blot was carried out using a standard semi-dry western blotting system (Invitrogen) at 20 Volt for 1 h. Subsequently the membrane was rinsed with ddH<sub>2</sub>O and stained with Ponceau red (0.1% Ponceau S, 3 % Trichloroacetic acid) for 5 minutes to confirm successful protein transfer. The staining was removed by washing the membrane with ddH<sub>2</sub>O. The membrane was blocked overnight in blocking buffer (Tris-buffered saline, TBS, 10 mM Tris-HCl, 150 mM NaCl, pH 7.5 with 0.1 % Tween 20 and 5 % (w/v) dried milk powder) and washed two times for 10 min with TBS containing 1% (w/v) dried milk powder afterwards. The membrane was incubated for 1 h with the respective antibodies (anti-RrgA or anti-RrgB, 1:10000 dilution in TBS, 37 °C) and subsequently washed two times for 10 min with TBS containing 0.1 % Tween 20 and one time for 10 min with TBS with 1 % dried milk powder. After incubation for 1 h with anti-rabbit secondary antibody (1:10000 dilution in TBS, 37 °C) unbound secondary antibodies on the membrane were removed by washing two times for 15 min with TBS, 0.1 % Tween 20 and 10 min in TBS and the membrane-bound proteins were stained with western blue stabilized substrate for alkaline phosphatase (Promega).

### **ATR-FTIR**

Proper protein folding was analyzed by Attenuated Total Reflection Fourier Transform Infrared Spectroscopy (ATR-FTIR, SI Fig. S5, S6). ATR-FTIR measurements were performed with a Tensor 27 FTIR spectrometer (Bruker). The detector unit was cooled down with liquid nitrogen. The ATR crystal was flushed and cleaned with isopropanol, which was allowed to evaporate completely before measurements. The ATR cell was connected to a digital control bath to setup a defined temperature of 23°C. Infrared spectra were recorded from 3600  $\text{cm}^{-1}$  to 800  $\text{cm}^{-1}$  with a resolution of 4  $\text{cm}^{-1}$ . The ATR cell chamber was purged by air throughout the measurement to provide an atmosphere largely free from water vapor. The background signal for all samples was recorded by the measurement of 15  $\mu\text{l}$  of PBS buffer. 15  $\mu\text{l}$  of the respective protein sample (3 $\mu\text{M}$ , PBS) was applied on the ATR crystal and incubated for 1 min. IR absorption was measured 10 times in 10 seconds intervals and the resulting spectra were later summarized to one average curve and experiments were performed in triplicate.

The region of the amide I vibration (1600  $\text{cm}^{-1}$  – 1700  $\text{cm}^{-1}$ ) was baseline corrected and normalized with the OPUS 6.5 software. The amide I vibration is the most useful for peptide structural analysis as it consists of several overlapping bands arising from different secondary structures (predominantly from C=O stretching vibrations ( $\approx 80\%$ ) and  $\text{NH}_2$  scissoring) [182-184]. The number and position of the underlying amide I peaks were determined by the second derivative profile of the spectrum and the amide I band was multi peak fitted based on the Gaussian function using Wavemetrics IGOR Pro 6.3. Subsequently the sub-peaks were assigned to secondary structure elements of the proteins as follows:  $\beta$ -sheet from 1610 to 1637  $\text{cm}^{-1}$  and 1680 to 1695  $\text{cm}^{-1}$ ,  $\alpha$ -helix from 1646 to 1661  $\text{cm}^{-1}$ , random coil/loops 1637 – 1648  $\text{cm}^{-1}$  and random coil/turns from 1660 to 1680  $\text{cm}^{-1}$  [182]. Thereby the area of the sub-peaks equals the percentage of these structures present in the protein. Peaks assigned to the same structures were summed up. Structural information were compared to data from published crystallography data (SI Fig. S5) and the sum of the individual RrgA domains to the structural data of RrgA FI to verify domain folding (SI Fig. S6).

### **6.2.3 Enzyme Linked ImmunoSorbent Assay**

Ninety six well MaxiSorp flat bottom plates (Nunc) were coated with 1 µg/well Fn in PBS pH 7.4 for 2 h at 37 °C followed by an overnight incubation at 4 °C. Unbound Fn was removed by washing three times for 10 min with washing buffer (PBS containing 0.05 % Tween 20). Empty binding sites were blocked for 2 h at 37 °C with blocking solution (100 µl PBS containing 1 % BSA) for 2 h at 37 °C, followed by three washing steps with washing buffer. Recombinant protein samples were transferred into the first wells with an initial equimolar ration of 750 pmol protein/ well and serially diluted two-fold with PBS, obtaining a final volume of 100 µl/well. Plates were incubated for 2 h at 37 °C and overnight at 4 °C. Unbound proteins were removed with three washing steps and the wells were incubated for 2 h at 37 °C with 100 µl of the respective primary rabbit antibodies (anti-RrgA, anti-RrgB, 1/10.000 dilutions). After three consecutive washing steps with washing buffer, all wells were incubated with 100 µl of secondary anti-Rabbit IgG antibody (1/10.000 dilutions) for another 2 h at 37 °C. Following another (3 x 10 min) washing procedure, all wells were filled with 150 µl alkaline phosphatase substrate buffer for the antibody detection. The reaction was stopped after 15 min by adding 50 µl of 1 M NaOH. Readout was performed at 405 nm (SI Fig. S9).

### **6.2.4 Surface Functionalization**

Glass microscope slides and silicon nitride AFM cantilevers (MLCT, Bruker) were cleaned and functionalized as described before (see SI 10.2.2 for a detailed protocol) [105, 151-153]. Briefly, the AFM tips were irradiated with UV light (UV PenRay) for 90 min, and subsequently rinsed with ethanol. Glass slides were cleaned in a 3 % solution of hydrochloric acid in doubly distilled water in an ultrasonic bath for 90 min, followed by three times cleaning in purified water in the ultrasonic bath for 10 min. For surface silanization both, slides and cantilevers, were incubated for 90 min in a solution of 0.1 mg mL<sup>-1</sup> COOH-PEG-Si(OC<sub>2</sub>H<sub>5</sub>)<sub>3</sub> dissolved in ethanol and doubly distilled water (w/w 95 %/5 %, pH 4.6). After the slides and cantilevers were rinsed with ethanol, they were cured at 110 °C for 30 min and stored in a vacuum chamber for up to 1 week.

### **6.2.5 Immobilization of Proteins for SMFS and LFM**

Prior to AFM experiments, the carboxyl group of the functionalized surfaces and cantilever tips were activated by incubating them in a solution of 42 mg mL<sup>-1</sup> of 1-(3-(dimethylamino)propyl)-3-ethylcarbodiimide and 20 mg mL<sup>-1</sup> of N-hydroxysuccinimide in standard PBS [151, 153]. Afterward, the slides and AFM tips were thoroughly rinsed with PBS. The activated AFM tips were incubated in a droplet of either 3 μM RrgA (FI, D1, D2, D3, D4), RrgB FI, RrgC FI or BSA for 2 h. The surfaces of the glass slides were exposed to 0.6 mg mL<sup>-1</sup> human fibronectin, 0.6 mg mL<sup>-1</sup> bovine serum albumin or PBS containing no protein for 2 h or 0.6 mg mL<sup>-1</sup> collagen I for 30 min, respectively. All proteins were dissolved in PBS (collagen I was dialyzed against PBS prior to use, as it was dissolved in 0.5 M acetic acid for long term storage), and the formation of covalent bonds between the EDC/NHS activated COOH group of the PEG molecules and the accessible NH<sub>2</sub> groups on the protein surfaces took place at room temperature. Subsequently, the slides and AFM tips were rinsed thoroughly with PBS and unbound NHS groups were saturated by placing them in Tris-buffered saline (TBS; 50 mM Tris, 150 mM NaCl, pH 7.6) for 20 min. Substrates for blocking experiments were subject to an additional incubation step with 3 μM RrgA FI, D3, or D4 in PBS for 30 min at room temperature, followed by a PBS washing step. The AFM cantilever and the glass slides were stored in PBS and used the same day. The overview over the surface chemistry in figure 3.8 was made using ChemDraw® 11.

### **6.2.6 Dynamic Single Molecule Force Measurements**

Single molecule force spectroscopy experiments were performed in PBS pH 7.4 at room temperature with a NanoWizard® I atomic force microscope (JPK Instruments) and silicon nitride AFM cantilevers (MLCT, Bruker) with a nominal force constant of  $0.03 \text{ N m}^{-1}$ . (see SI 10.2.3 for a protocol). In brief; the optical lever sensitivity and spring constant of the cantilever were determined by the thermal noise method (see chapter 3.2.1 and SI 10.2.3 part 1.1 for a protocol) [111]. Force–distance curves were obtained using the Force RampDesigner™ (JPK Instruments) applying a contact force of 250 pN, a contact time of 1 s and a retraction velocity of  $1000 \text{ nm s}^{-1}$ . Experiments for every protein combination were carried out at least in triplicate and the force curves were obtained at three different positions on the substrates. For experiments with increasing force loading rates, the retraction speed was varied between 250 and  $4000 \text{ nm s}^{-1}$ . Force extension traces were analyzed using the JPK data processing software (JPK Instruments) and screened for force peaks occurring at rupture lengths above 70 nm, in order to sort out nonspecific interactions. In the case of multiple adhesion peaks, only the last event was considered. Force curves were analyzed using the extensible worm-like chain model (see chapter 3.2.1) [38] to obtain rupture lengths and force loading rates for the respective protein combination. The kinetic parameters were determined using the Bell-Evans-Ritchie model (see chapter 3.2.2 and SI Fig. S7) [42]. Diagrams were illustrated and data fitted using Microsoft Excel 2016 and Wavemetrics Igor Pro 6.3 software.

### 6.2.7 Lateral Force Measurements

Lateral force experiments were performed in PBS pH 7.4 at room temperature with a Nano Wizard® I atomic force microscope (JPK Instruments) and rectangular silicon nitride AFM cantilevers (MLCT, Bruker) with a nominal force constant of  $0.02 \text{ N m}^{-1}$ . The optical lever sensitivity and spring constant of the cantilever were determined by the thermal noise method (see chapter 3.2.1, 3.3.1 and SI 10.2.3 part 1.1 for a protocol) [111]. For lateral force experiments the lateral deflection (trace and retrace) of the cantilever were recorded on  $5 \times 5 \mu\text{m}^2$  area with  $256 \times 256$  pixels while scanning the surface in the direction perpendicular to the long cantilever axis applying a contact force of 150 pN and a scan velocity of  $11 \mu\text{m s}^{-1}$ . The lateral force was analyzed using the JPK data processing software (JPK Instruments). A polynomial fit was subtracted from each scan line of the lateral deflection images (trace and retrace). By that the lateral offset (usually used to determine the friction force established between the tip and the substrate) was eliminated, leaving the lateral bending, which only results from protein interactions. The root mean squared RMS roughness  $R_q$  was determined (for trace and retrace) incorporating the whole image area and  $I_l$  was assumed to be the average of trace and retrace roughness of at least two independent experiments. Lateral force was calculated using the vertical optical lever sensitivity (see chapter 3.3.1 and Eq. 19) the beam mechanics model [43-45, 123, 124] and with the geometrical parameters:  $t = 0.55 \mu\text{m}$ ,  $w = 20 \mu\text{m}$ ,  $l = 210 \mu\text{m}$ ,  $h = 2.5 \mu\text{m}$ , and  $E = 300 \text{ GPa}$  [127]. Moreover, the effective lateral forces for individual protein pairs, were obtained by subtracting lateral forces established between a collagen I coated surface and a cantilever tip without proteins immobilized.



## 7 Results and Discussion

### 7.1 Pneumococcal Pilus-1 Tip Protein RrgA–Fibronectin Adhesion

The following chapter contains sections and figures from the article

#### “Single Molecule Force Spectroscopy Reveals Two-Domain Binding Mode of Pilus-1 Tip Protein RrgA of *Streptococcus Pneumoniae* to Fibronectin”

by Tanja D. Becke, Stefan Ness, Raimund Gürster, Arndt F. Schilling, Anne-Marie di Guilmi, Stefanie Sudhop, Markus Hilleringmann, and Hauke Clausen-Schaumann

Published: ACS Nano, 2018, 12 (1), pp 549–558,

DOI: 10.1021/acsnano.7b07247 [105]

#### 7.1.1 Interaction of Full-Length RrgA with Fibronectin

“To investigate binding forces of RrgA to Fn, full-length RrgA [...] [(RrgA FI, SI Fig. S1, S3, S5, S6)] was expressed in *E. coli*, purified, and covalently attached to the AFM tip *via* a 5 kDa silane-PEG-COOH linker [...] [(Figure 7.1 a)]. Human Fn was immobilized on a glass substrate using the same surface linker (see the Materials and Methods section [chapter 6.2.5] for details). AFM imaging of Fn-coated glass surfaces [...] [(Fig. 7.1 b)] confirmed a homogeneous distribution of Fn on the substrate surface. The dimeric structure of Fn can be recognized, and Fn seems to be compact with a height of 4–5 nm and a length of ~120 nm, which is consistent with previous AFM data and reminiscent of the structure of Fn in solution [185]. [...] [Figure 7.1 c] shows the distribution of rupture forces and rupture lengths of 1400 rupture events together with five representative force–distance curves of RrgA FI on Fn, recorded at a pulling velocity of 1000 nm s<sup>-1</sup>. After overcoming nonspecific surface interactions between AFM tip and substrate, and stretching the PEG linkers (>70 nm), 19 % of the force curves showed mainly single or double rupture events at rupture lengths between 70 and 400 nm, while in 81 % of the

## Results and Discussion

---

force curves, no specific interaction was observed. The corresponding force–extension traces were fitted using an extensible worm-like chain (eWLC) model [Eq. 3] [38]. [...].

The most probable rupture force between RrgA FI and Fn was  $51.6 \pm 2$  pN, which is in the typical force range of receptor–ligand interactions [109, 162] and well below the 100–300 pN reported for the interaction of single staphylococcal FnBPs with Fn at comparable pulling velocities [27].

The majority of rupture events occurred at a tip substrate separation of approximately 100 nm, which matches well with the length obtained by stretching the PEG spacers (~40 nm each), together with the RrgA FI and Fn molecules. Unfolding of Fn or RrgA FI is therefore rather unlikely, which is consistent with earlier AFM measurements, which report unfolding forces above 100 pN for single Fn modules [186, 187]. In addition RrgA FI is stabilized by two intramolecular isopeptide bonds which can sustain much higher forces than the ones observed in our experiments [88, 153, 188]. The frequency of rupture events could be reduced by blocking the binding sites of RrgA on Fn with free RrgA FI or when performing control experiments with [the pilus-1 backbone protein RrgB, Fig. S8], BSA or no protein immobilized on the PEG-coated substrate [...][Figure 7.1 d), indicating that the rupture events observed in [...][Figure 7.1 c] were indeed caused by specific RrgA FI–Fn interactions. [Binding of RrgA FI to Fn could further be confirmed by ELISA studies, whose results showed in different independent experiments unsteady, but always dose depending binding of the pilus-1 tip protein to Fn (see SI Fig. S.9).]

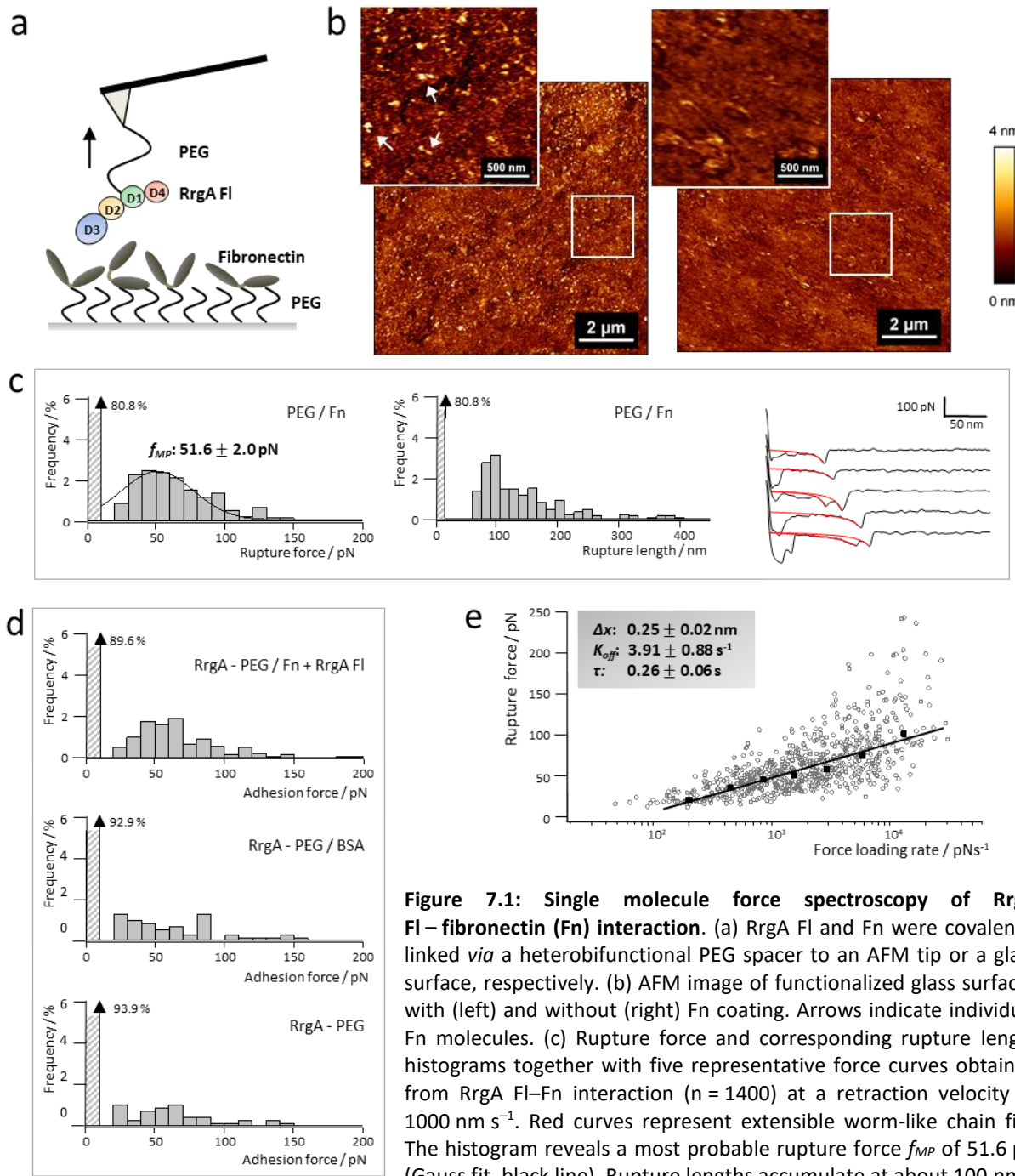


**Figure 7.1: Single molecule force spectroscopy of RrgA FI–fibronectin (Fn) interaction.** (a) RrgA FI and Fn were covalently linked *via* a heterobifunctional PEG spacer to an AFM tip or a glass surface, respectively. (b) AFM image of functionalized glass surfaces with (left) and without (right) Fn coating. Arrows indicate individual Fn molecules. (c) Rupture force and corresponding rupture length histograms together with five representative force curves obtained from RrgA FI–Fn interaction ( $n = 1400$ ) at a retraction velocity of  $1000 \text{ nm s}^{-1}$ . Red curves represent extensible worm-like chain fits. The histogram reveals a most probable rupture force  $f_{MP}$  of  $51.6 \text{ pN}$  (Gauss fit, black line). Rupture lengths accumulate at about  $100 \text{ nm}$ .

(d) Control experiments performed on PEG/Fn surfaces preincubated with RrgA FI ( $n = 1200$ ), on PEG/BSA surfaces ( $n = 700$ ) or on PEG-coated substrates without any protein immobilized ( $n = 700$ ). (e) Semi-logarithmic representation of RrgA FI–Fn rupture forces vs force-loading rate at retraction velocities from  $250$  to  $4000 \text{ nm s}^{-1}$ . Gray circles correspond to single rupture events, whereas black squares represent the most probable rupture forces for seven distinct force-loading rate intervals between  $50$  and  $30000 \text{ pN s}^{-1}$ , determined by fitting Gaussian distributions to the rupture force histograms within these intervals (see SI, Figure [..][S7]). The black line represents a Bell[Evans-Ritchie] fit to the seven  $f_{MP}$  with the fit parameters  $\Delta x = 0.25 \text{ nm}$  and  $k_{off} = 3.91 \text{ s}^{-1}$  (corresponding to  $\tau = 0.26 \text{ s}$ ). (a-e) The figure has been adapted from Becke *et al.*, ACSnano, 2018 [105].

## Results and Discussion

---

To obtain the kinetic parameters of the RrgA Fl–Fn interaction, the force-loading rate was varied by altering the retraction velocity of the z-piezo of the AFM between 250 and 4000 nm s<sup>-1</sup>. In [...] [Figure 7.1 e], the rupture forces of 676 rupture events are plotted vs the logarithm of the force loading rate (gray circles). In addition, the most probable rupture forces for seven distinct force-loading rate intervals between 50 and 30.000 pN s<sup>-1</sup> were determined by fitting Gaussian distributions to the rupture force histograms within these intervals [...] [(Figure 7.1 e, black squares, and Supporting Information Figure S7)]. To extract the average bond lifetime at zero force from these data, we used the Bell–Evans [–Ritchie] model [(Eq. 12)] [42], which assumes that the activation barrier of the binding potential decreases linearly with force, leading to an exponential amplification of the dissociation kinetics with force and a logarithmic increase of the most probable bond rupture force  $f_{MP}$  with the force-loading rate.[...]. Fitting the Bell–Evans [–Ritchie] model (black curve in [...] [Figure 7.1 e]) to the most probable rupture forces (black squares in [...] [Figure 7.1 e]) renders a zero force off-rate  $k_{off}$  for the RrgA Fl – Fn interaction of  $3.91 \pm 0.88$  s<sup>-1</sup> ( $\Delta x = 0.25$  nm), which corresponds to a mean bond lifetime at zero force  $\tau = 1/k_{off}$  of  $0.26 \pm 0.06$  s and indicates a rapid dissociation of RrgA Fl – Fn bonds. Comparably short bond lifetimes and similar  $\Delta x$  values have already been reported for other bacterial adhesion proteins, such as SpaC, the key adhesion protein of the *Lactobacillus rhamnosus* GG pilus or FnBP of *S. epidermis* and *S. aureus* [27, 109, 165, 172]. It has been suggested that such comparably weak bonds may enable bacteria to form an initial contact to host cells and at the same time provide sufficient mobility on the tissue surface to permit searching for stronger and more specific surface receptors, *e.g.*, under shear conditions, as they are encountered in the nasopharynx and lung or on blood vessels [26, 109, 189]. A similar interaction scheme has been observed for neutrophils, which roll along the lymphatic vessel wall, where L-Selectin on the neutrophils surface rapidly binds to and detaches from peripheral lymph node addressin, which is displayed on the vessel wall ( $\tau$  of 0.15 s) [190]. In this way, the immune cells are able to withstand moderate detachment

force generated by shear stress and are able to search the vessel walls for specific inflammatory induced receptors, such as ICAM - 1 and PECAM - 1 [191, 192]. Considering that *S. pneumoniae* triggers pneumonia particularly in individuals with pre-existing diseases [47, 48] which evoke alterations in the ECM composition, such as increased fibronectin expression [193, 194], pilus-1 adhesion to Fn may play a similar role, constituting an additional bacterial fitness factor favoring the expansion and invasion of the bacterium into prestressed tissue. However, RrgA might also facilitate adhesion to host surfaces at physiological Fn amounts in the presence of a capsule, which is not possible for other Fn-binding molecules of *S. pneumoniae* [see chapter 2.2].

### **7.1.2 Interaction of Individual Domains D1–D4 with Fibronectin**

To address the question which domain of RrgA mediates the bond with Fn, we repeated the SMFS experiments with distinct RrgA domains. A structure-based approach taking RrgAs three-dimensional structure (RCSB PDB: 2WW8) [88] as a basis was applied to design respective RrgA domain constructs (see SI Figure S1). Domains D1–D4 of high purity were generated (see the Materials and Methods [chapter 6.2.1] and Supporting Information [...] [Figure S3]), checked for correct folding *via* attenuated total reflection Fourier transform infrared spectroscopy (SI [...] [Figure S6]) and covalently attached to the AFM tip *via* the same PEG surface linker used for RrgA Fl. [...] [Figure 7.2] shows the binding frequencies of RrgA Fl as well as all four domains individually against Fn and BSA. The terminal domains D3 and D4 adhere to Fn with frequencies of 19.7% and 16.5%, respectively (total number of evaluated force curves,  $n(\text{D3-Fn}) = 1200$ ;  $n(\text{D4-Fn}) = 1000$ ), which is in the same range as RrgA Fl (19.2%) and significantly higher than on the BSA controls (4.9% and 2.7%) and on pure PEG surfaces (data not shown). D1 and D2, on the other hand, show adhesion rates of only 3.8% and 4.1%, respectively, which is well below the value determined for RrgA Fl and only slightly above the 2.4% and 2.9%

## Results and Discussion

determined on the respective BSA controls. This indicates that the adhesion of D3 and D4 to Fn is the result of a specific molecular recognition event, highlighting the special role of RrgA's terminal domains D3 and D4 for the adhesion of the pilus-1 to Fn, while the interaction of D1 and D2 with Fn is negligible. [ELISA studies confirmed the role for D3 and D4 during interaction with Fn. In different independent assays both domains were able to bind to the ECM molecule in an unsteady, but dose depending manner and to a lesser extent as RrgA FI. The binding of domains D1 and D2 to Fn was insignificant (SI Fig. S9)].

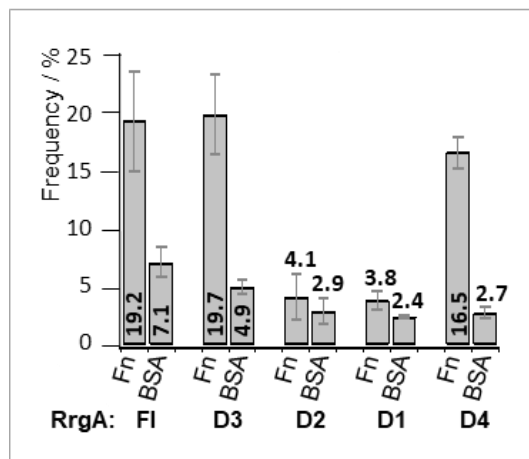


**Figure 7.2: RrgA FI and single domain interactions with fibronectin.** AFM-tips coated with D3 and D4 adhere to Fn substrates with frequencies of 19.7% and 16.5%, respectively, which is in the same range as for RrgA FI –Fn interaction (19.2%). Adherence to BSA coated control surfaces was significantly reduced (4.9% for D3 and 2.7% for D4). D1 and D2 show adhesion rates of only 3.8% and 4.1%, respectively, which is well below the value determined for RrgA-FI and only slightly above the 2.4% and 2.9% determined on the respective BSA controls (error bars originate from  $n = 3$  independent experiments with  $> 1000$  analyzed force curves for each protein pair). The figure has been adapted from Becke *et al.*, ACSnano, 2018 [105].

Structure-based analysis and comparison with other bacterial systems suggest that domains D1 and D2 serve as stalk regions with additional specific functions in other host factor interactions. In addition, the intramolecular isopeptide bonds in D2 (and D4) are essential for RrgA FI stability [88].

Parts a and b of [...] [Figure 7.3] show rupture force and length distributions as well as representative force–distance curves of D3 and D4 on Fn. For D3, the most probable rupture force  $f_{MP}$  at  $1000 \text{ nm s}^{-1}$  pulling velocity is 52.8 pN, which is close to  $f_{MP}$  for the full length protein at the same conditions, while for D4  $f_{MP}$  is only 46.2 pN. For both D3 and D4, most rupture events were observed at tip–sample separations around 100 nm and a smaller percentage at separations as far as

400 nm. As already observed for RrgA FI on Fn, the rupture forces of both D3 and D4 on Fn increase nearly logarithmically with the force-loading rate [...] (Figure 7.3 c)], which is in accordance with the Bell[-Evans-Ritchie] model, indicating an almost linear decrease of the binding potential barrier with force. The dissociation rate constants and average bond lifetimes at zero force were again derived using [...] [Eq. 12] and are in the same range as for the RrgA FI–Fn interaction. For D3 on Fn we obtain a dissociation rate constant at zero force  $k_{off}$  of  $6.72 \text{ s}^{-1}$  which corresponds to a bond lifetime at zero force of  $\tau = 0.15 \text{ s}$  and a  $\Delta x$  of  $0.19 \text{ nm}$ . The average bond lifetime at zero force is thus slightly smaller than for RrgA FI on Fn ( $\tau = 0.26 \text{ s}$ ). With  $k_{off} = 2.33 \text{ s}^{-1}$  which corresponds to  $\tau = 0.43 \text{ s}$ , the D4 domain exhibits a somewhat longer average bond lifetime as RrgA FI and a  $\Delta x$  of  $0.32 \text{ nm}$ . Both D3 and D4 show fast detachment from Fn, which is characteristic for transient binding. Note that with  $\tau = 0.29 \text{ s}$  and  $\Delta x = 0.23 \text{ nm}$  the average bond lifetime and bond length of the two domains D3 and D4 is close to the values observed for RrgA FI ( $\tau = 0.26 \text{ s}$  and a  $\Delta x$  of  $0.25 \text{ nm}$ ).

### **7.1.3 Simultaneous Binding of D3 and D4 to Fibronectin**

Finally, we investigated whether RrgA's terminal domains D3 and D4 can bind to Fn simultaneously, which could explain the double peaks observed in the force–distance curves of the RrgA FI–Fn interaction [...] (Figure 7.1 c)]. We blocked the binding sites for D3 or D4 on Fn by applying either free D4 or D3 molecules on the Fn substrate prior to the SMFS experiments with RrgA FI attached to the AFM tip [...] (Figure 7.4 a)]. The frequency of RrgA FI adhesion events on the Fn substrate was reduced by approximately 50%, from 19% to  $\sim 12\%$  and  $\sim 9\%$  upon blocking Fn with D3 and D4, respectively (total number of analyzed force curves,  $n(\text{Fn} + \text{D4}) = 1400$ ,  $n(\text{Fn} + \text{D3}) = 1300$ ). These results clearly show that the two domains D3 and D4 bind to distinct binding sites along the Fn molecule and that the

two sites are far enough apart, in order to permit binding to one site, if the other site is blocked by a bound domain.

The force curves showing double-rupture events were reduced from ~7% with RrgA FI to ~3% for Fn treated with D3 and to 2% for Fn treated with D4, which indicates that the double ruptures observed in [...] [Figure 7.1 c] may indeed be caused by a stepwise detachment of the two domains from Fn. To further corroborate this assumption, we determined the length increment  $\Delta l$  between the two peaks for all force curves with double rupture events [...] [(see Figure 7.4 b—black arrows)], and plotted the distribution in [...] [Figure 7.4 c].

For RrgA FI on Fn, there is a distinct peak in the  $\Delta l$  distribution around 15–20 nm [...] [(Figure 7.4 c, top)], which is significantly reduced when blocking Fn with D3 or D4 and which disappears completely for single domain (D3 and D4) interactions [...] [(Figure 7.4 c, centre and bottom)]. The observed  $\Delta l$  of 15–20 nm correlates rather well with the distance between domain D3 and D4 on native RrgA FI of about 18–19 nm (see also [...] [Figure 2.2 b]) [17, 88]. This corroborates our assumption that the two terminal domains D3 and D4 can bind to Fn simultaneously, giving rise to the double ruptures observed in the force–distance curves of RrgA FI on Fn [...] [(Figures 7.1 c and 7.4 b)]. [Binding of domains D3 and D4 to specific sites on Fn, which are far enough apart in order to permit simultaneous interaction of both domains, is confirmed with ELISA binding studies (see SI Fig. S9). At same molar concentrations the binding of both domains D3 and D4 resulted in a more than twofold higher signal as for the interaction of individual domains, indicating that both domains can bind at the same time to different sites on Fn].



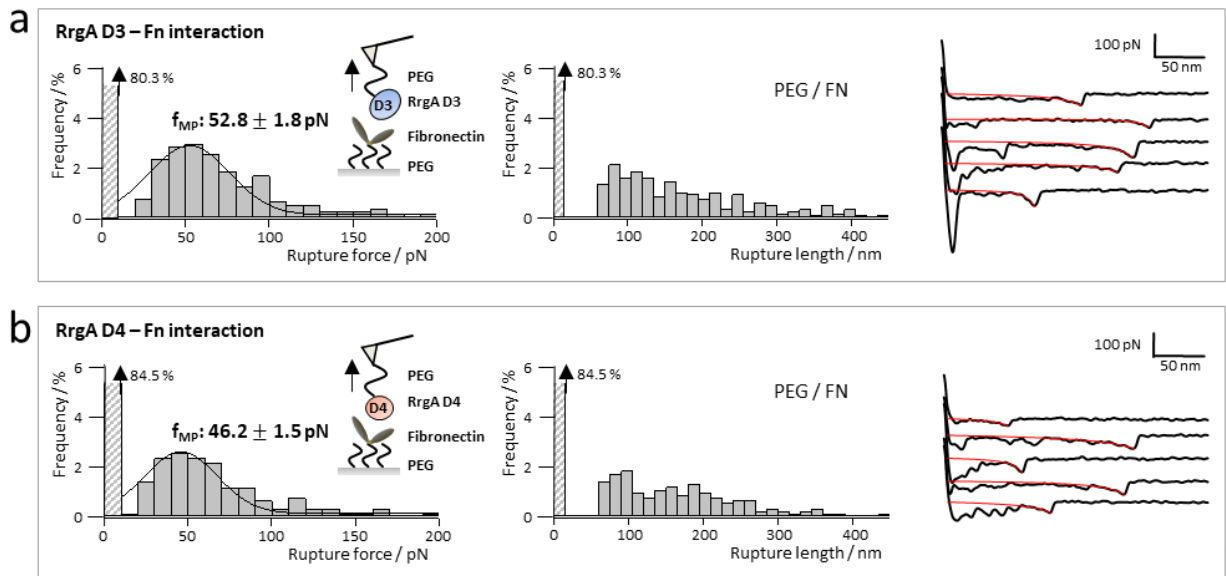
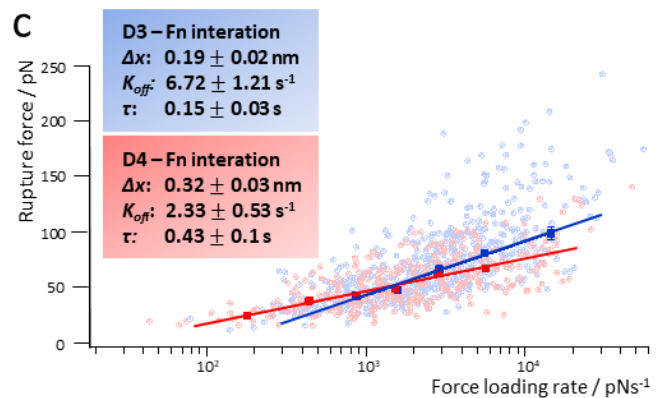


**Figure 7.3: Dynamic force spectroscopy of the RrgA D3 and D4 – fibronectin (Fn) interaction.** (a, b) D3 or D4 domains were covalently attached to the AFM tip, Fn was coated on glass. Rupture force and corresponding rupture length histograms derived from  $n = 1200$  (D3-Fn) or  $n = 1000$  (D4-Fn) force–distance curves are illustrated (left). The Gauss fits (black line in the rupture force histograms) render a most probable force  $f_{MP}$  of 52.8 pN for D3–Fn and of 46.2 pN for D4–Fn. Rupture length histograms (middle), and five representative force curves (right), together



with an extensible worm-like chain fit (red). Retraction speed: 1000 nm  $s^{-1}$ . (c) RrgA D3–Fn (blue) and RrgA D4–Fn (red) rupture forces, obtained by varying the retraction velocity from 250 to 4000 nm  $s^{-1}$ . Dots represent data gained from single rupture events, while the squares show the most probable rupture force for five (D3-Fn) and six (D4-Fn) distinct force-loading rate intervals between 50 and 30.000 pN  $s^{-1}$  and were determined by fitting Gaussian distributions to the rupture force histograms within these intervals. The blue line represents a Bell fit to the most probable forces of D3–Fn, the red line to the most probable forces of D4–F. The figure has been adapted from Becke *et al.*, ACSnano, 2018 [105].

Note that binding of RrgA FI to multiple Fn molecules, as has been reported for *S. aureus* FnBPs [166, 181], is extremely unlikely in our study because individual Fn molecules are typically separated by several hundred nm, as can be seen in [...] [Figure 7.1 b]. However, in the case of higher Fn densities, multi-Fn binding

cannot be ruled out. Nevertheless, unlike staphylococcal FnBPs, which have up to 11 largely unstructured Fn binding regions that can bind up to 6 Fn molecules via tandem  $\beta$ -zipper repeats, RrgA comprises only four highly structured domains, making a similar binding mechanism as in staphylococcal FnBPs unlikely. Additional control experiments where Fn was linked to OPSS-PEG-coated substrates via thiol groups, which leaves the N-terminal site of Fn accessible [187, 195], showed the same double ruptures with identical  $\Delta l$  (see Supporting Information [...] [Figure S10]), indicating that the binding sites could be located near the N-terminal end of Fn, as for staphylococcal FnBPs. This however remains speculative, and the exact locations of the D3 and D4 binding sites on Fn have to be identified in future studies with, *e.g.*, defined Fn fragments.

Unlike for other bacterial adhesins showing multidomain binding to Fn, where the interaction strength increases with the number of interactions [166, 168, 172, 196], in the case of the RrgA FI–Fn interaction, adhesion force and bond lifetime seem to be unaffected by multidomain binding: In the SMFS experiments, the two domains unbind sequentially and independently and not in a concerted and cooperative manner. As already pointed out in the last section, the bond lifetime ( $\tau$ ) and bond length ( $\Delta x$ ) of RrgA FI seem to be average values of the individual domains D3 and D4 rather than the sum of both, as would be the expected if both domains would act in concert and unbind in a cooperative manner. The independent binding of the domains D3 and D4 may increase the likelihood of binding to Fn and their simultaneous binding may extend the overall interaction time by enhancing the chance of rebinding of one domain while the other one remains attached. However, as rebinding effects are not readily accessible via SMFS, this assumption has to be validated in future experiments, *e.g.*, with surface plasmon resonance spectroscopy or a quartz crystal microbalance setup."

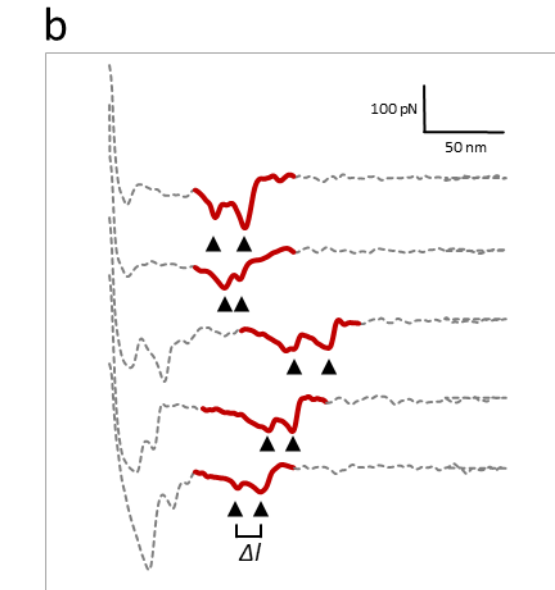
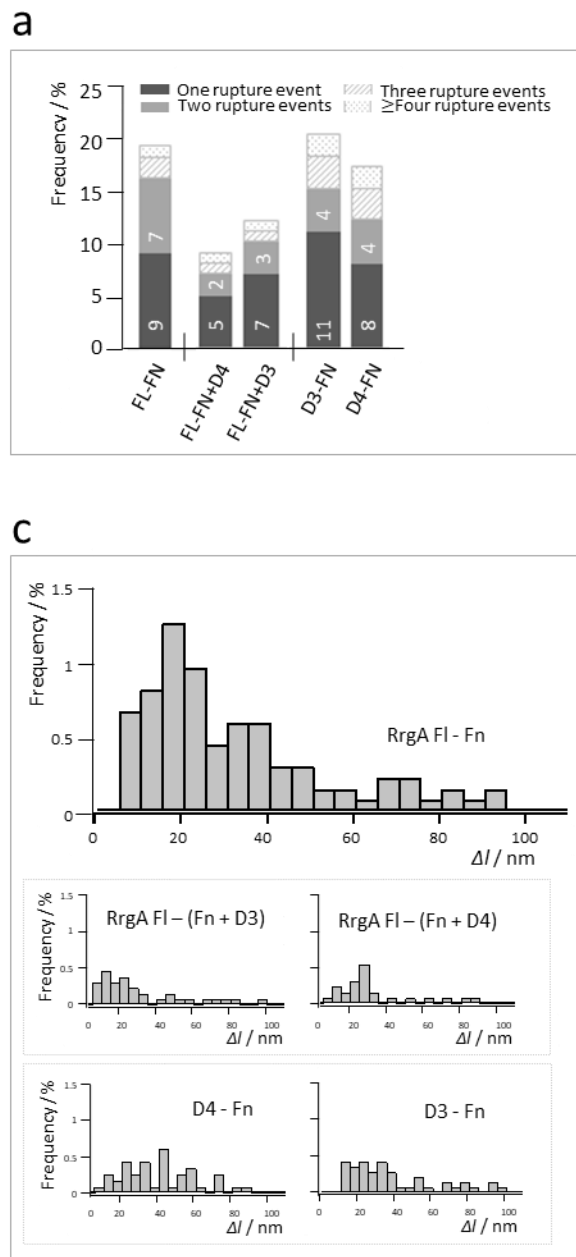


**Figure 7.4: Simultaneous binding of RrgA domains D3 and D4 to Fn** (a) Frequency of RrgA FI adhesion events on Fn was reduced from 19 % to ~12 % and ~9 % upon blocking Fn with D3 and D4, respectively. Force curves displaying double rupture peaks were mainly observed for the RrgA FI-Fn interaction (7 %) and nearly disappeared after the saturation of binding sides on Fn with D4 (2 %) or D3 (3 %). Force curves with two rupture events rarely appeared in D3-Fn and D4-Fn adhesion (4 % each). Number of analyzed force curves: RrgA FI-Fn,  $n = 1400$ ; D3-Fn,  $n = 1200$ ; D4-Fn,  $n = 1000$ ; RrgA FI-(Fn+D4),  $n = 1400$ ; RrgA FI-(Fn+D3),  $n = 1300$ .

(b) Representative force curves with two rupture events obtained from RrgA FI-Fn interaction. Arrowheads indicate the rupture peaks. (c) Distribution of the length increment  $\Delta l$  between the two rupture peaks. For RrgA FI-Fn,  $\Delta l$  frequency is highest for distances from 15–20 nm. This accumulation is significantly reduced by blocking Fn with D3 or D4 (middle) and disappears in single domain (D3 or D4) - Fn interactions (bottom). The figure has been adapted from Becke *et al.*, ACSnano, 2018 [105].

“It has been shown that [the pneumococcal pilus-1 tip protein] RrgA can interact with fibronectin (Fn), which is present in the connective tissue matrix [14, 197] and which becomes particularly accessible after degradation of the mucosal layer during infection and is therefore a target for a large number of bacterial adhesins [36, 198]. However, a detailed understanding of the interaction of RrgA and its four domains D1 - D4 with Fn is still lacking, and until today no isolated RrgA fragment was found to retain its capability to adhere to epithelial cells or any ECM components [21].[...]. [...] [Here] we have used the [...] [AFM] in the [...] [SMFS] mode, to explore the interaction force and binding kinetics of *S. pneumoniae* TIGR 4 pilus-1 tip protein RrgA with the extracellular matrix protein fibronectin, in order to gain a better understanding of how the pilus-1 of *S. pneumoniae* interacts with and adheres to host cells. Our results show that full length RrgA and its terminal domains D3 and D4 bind to fibronectin, with different binding strengths. Both domains can interact with Fn independently or in concert, revealing two-domain binding mechanism for the pilus-1 tip protein. The short bond lifetimes observed for full-length D3 and D4 binding to Fn indicate that RrgA mediated Fn adhesion may constitute a transient, initial contact allowing the bacterium to further search host structures for more specific surface receptors which permit stronger attachment and, *e.g.*, promoting bacterial virulence, as has been proposed, *e.g.*, for *Lactobacillus rhamnosus* [109].”

## 7.2 Pneumococcal Pilus-1 Pilins – Collagen I Adhesion

In addition to Fn, it is known that pilus-1 tip protein RrgA can interact with collagen type I (Col I) [14, 21], which is the major constituent of most ECM variants where it forms fibrils with diameters ranging from 20 to 70 nm in an entropy-driven self-assembly process (fibrillogenesis) [199, 200]. In contrast, the pilus-1 backbone protein RrgB and the anchor protein RrgC showed no interaction to Col I in standard binding assays and a detailed understanding of the biomechanical interaction of pilus-1 with Col I is still lacking [14].

We have used SMFS and LFM, to explore the interaction of *S. pneumoniae* TIGR 4 proteins RrgA, RrgB and RrgC with Col I, in order to expand the understanding of how the pilus-1 of *S. pneumoniae* interacts with and adheres to host cells and surrounding matrices. The results show that RrgA FI and RrgB FI, but not RrgC FI, bind to Col I with different binding strengths in the lower force range known for receptor ligand interactions [109, 162, 201]. In addition, interaction of RrgB FI - Col I becomes stronger if the backbone protein is dragged along the Collagen fibrils in lateral direction, whereas for RrgA FI Col I, adhesion forces remain modest.

### 7.2.1 SMFS of Full-Length RrgA, RrgB and RrgC with Collagen I

To investigate binding mechanics of pneumococcal pilins with Col I, RrgA FI, RrgB FI and RrgC FI (SI, Fig. S1 and S2) were expressed in *E. coli*, purified, check for correct folding (SI, Fig. S5), and covalently attached to the AFM tip *via* a 5 kDa silane-PEG-COOH linker. Human Col I was immobilized on a glass substrate using the same surface chemistry (see the Materials and Methods section chapter 6.2.4 and 6.2.5 and SI 10.2.2 for details). AFM imaging of Col I coated glass surfaces confirmed a homogeneous distribution of Col I arranged in small fibrils with random orientation (Figure 7.5). The disorganized fibrils resemble the Col I structure in skin, airways and artery [202]. In contrast, in tendon and ligaments collagen can be found as parallel fibre bundles and as concentric waves in bone [203, 204].

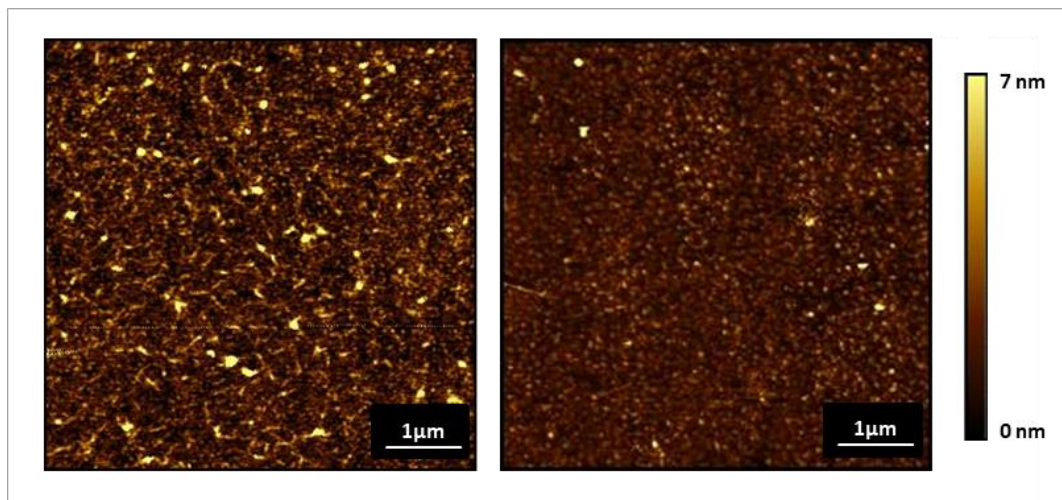


**Figure 7.5: AFM image of functionalized glass surfaces with (left) and without (right) Col I coating.** Col I is homogeneous distributed and arranged in small fibrils with a random orientation, which resembles the Col I structure in skin, airways and artery [202].

Figure 7.6 a and b show the distribution of rupture forces and rupture lengths of 1300 force-distance curves recorded for RrgA FI on Col I and 1100 force-distance traces for RrgB FI on Col I, pooled from three independent experiments and recorded at a pulling velocity of  $1000 \text{ nm s}^{-1}$ , respectively. After overcoming nonspecific surface interactions between AFM tip and substrate, and stretching the PEG linkers ( $>70 \text{ nm}$ ), 12.3 % of the force curves showed well defined rupture events (Fig. 7.6 d, left) at rupture lengths between 70 and 300 nm for RrgA FI - Col I, while 87.7 % of the force curves showed no specific interaction. Similar values were obtained for RrgB FI – Col I where 12.2 % of force curves showed rupture events between 70 and 250 nm accumulating around 100 nm. RrgC FI as well as BSA coupled to the AFM tip showed no significant interaction with immobilized Col I (Fig. 7.6 c), highlighting the special role of RrgA FI and RrgB FI for pneumococcal adhesion to the host.

Taking the stretching of the PEG spacer (40 nm each) and of the proteins into account, the majority of ruptures should occur at a tip-substrate-separation of approximately 100 nm. The longer extensions (especially for RrgA FI) could be explained by the long, fibrillar structure of collagen which may not be covalently coupled along the whole molecule to the glass surface and could thus partially be lifted off the substrate.

The most probable rupture force  $f_{MP}$  between RrgA FI and Col I was  $39.4 \pm 0.7$  pN and  $32.4 \pm 1$  pN between RrgB FI and Col I, which is in the lower force range of typical receptor–ligand interactions [109, 162] and well below forces reported for bacterial interaction with Collagen I at comparable pulling velocities [171, 201]. Again, similar to the Fn interactions, the weak adhesion forces of RrgA FI to Col I, which can establish even in the presence of the pneumococcal capsule [58], may help pili to rapidly adhere and detach in shear flow conditions and rebind to more specific host sites. However, this assumption again remains speculative as RrgA FI – Col I binding off-rates ( $k_{off}$ ) and lifetimes at zero force  $\tau$  remain to be determined.

In contrast to RrgA FI, whose binding to Col I was already known (classical ELISA experiments) [14, 21], an interaction of the backbone protein with the ECM molecule was not reported. During SMFS experiments, a directional, external force is applied on the protein interaction, which was not the case in previous investigations [14, 21]. This suggests that adhesion of RrgB FI to Col I molecules may be force-dependent. Regarding the structure of RrgB FI (see Fig.2.2) [89] a force-dependent interlocking of its domain D3 with the collagen fibrils resulting in a subsequent turning of domain D3 during pulling on the RrgB FI – Col I bond seems possible and could explain the regions of constant force observed before bond rupture events (Fig. 7.6 d, blue arrows), which, in contrast to RrgA FI - Col I, could not always be fitted with the eWLC model (see Eq. 3) [38]. The speculative assumptions of RrgB interlocking with collagen fibrils might be confirmed by side directed coupling of RrgB FI to the AFM tip *via* its N- or C-terminus which would be expected to result in a significant reduction or increase in adhesion events during SMFS experiments, respectively. Furthermore, genetically engineering RrgBs lacking the D3 domain could clarify D3's role during interaction with host Col I.

## Results and Discussion

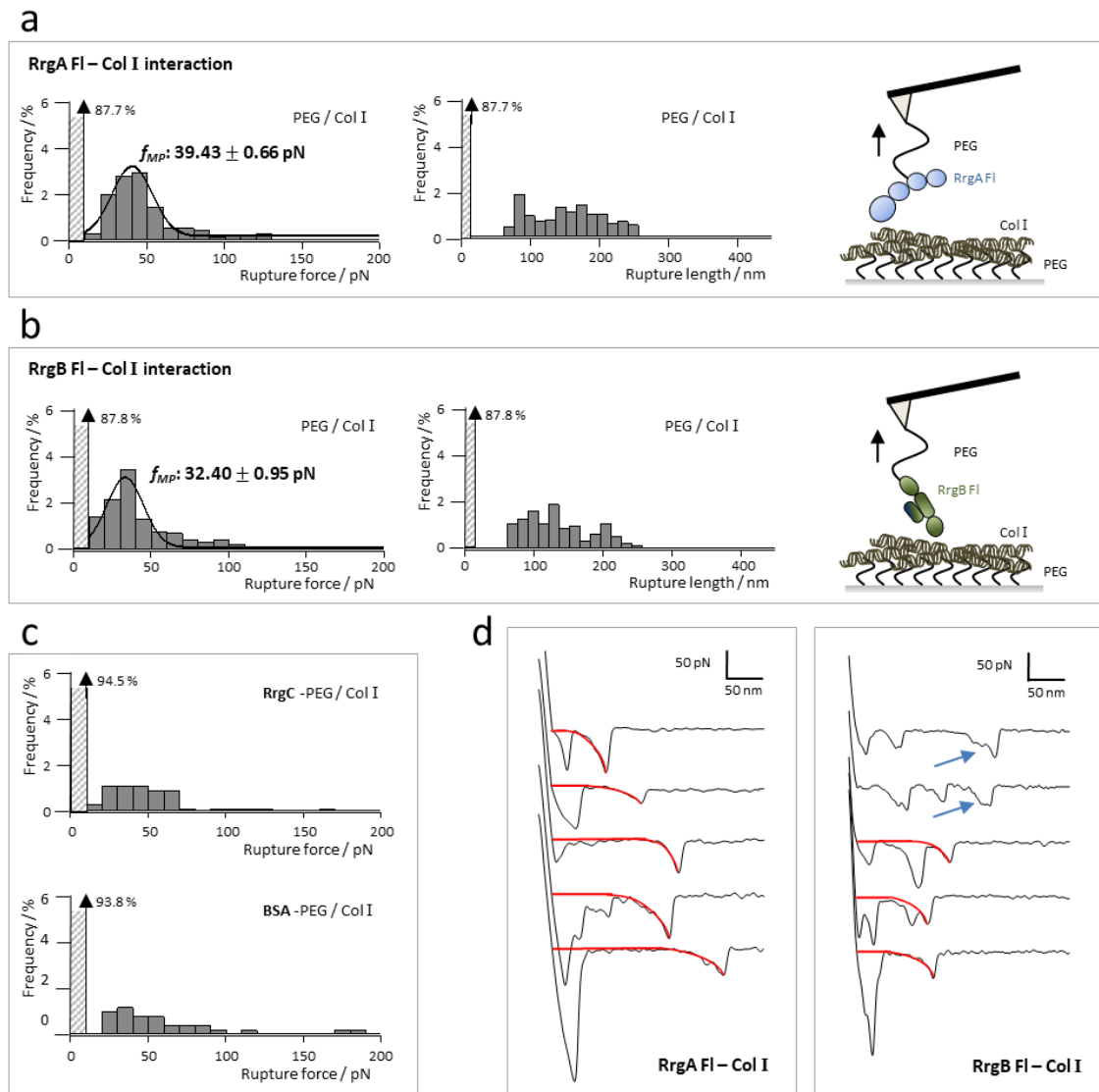


**Figure 7.6: Single molecule force spectroscopy of pneumococcal pilus-1 pilins with collagen I (Col I).**

(a,b) RrgA FI or RrgB FI were covalently attached to the AFM tip, Col I was coated on glass *via* a hetero-bifunctional PEG spacer, respectively. Rupture force and corresponding rupture length histograms for RrgA FI - Col I ( $n = 1300$ ), as well as RrgB FI - Col I ( $n = 1100$ ) interaction at a retraction velocity of  $1000 \text{ nm s}^{-1}$  are shown. A most probable rupture force (Gaussian fits in the rupture force histograms) was rendered for RrgA FI - Col I of  $f_{MP} = 39.4 \text{ pN}$  and for RrgB FI - Col I of  $f_{MP} = 32.4 \text{ pN}$ . Ruptures accumulate around  $100 \text{ nm}$  for RrgB FI - Col I and between  $100 - 200 \text{ nm}$  for RrgA FI - Col I. (c) Interactions for RrgC FI ( $n = 1000$ ), or BSA ( $n = 500$ ) attached to the tip with Col I are negligible. (d) Representative force curves together with extensible worm-like chain fits (red) for RrgA FI - Col I (left) RrgB FI - Col I (right). As indicated with blue arrows, a fitting of interactions between RrgB FI and Col I with the eWLC was not always possible.



### **7.2.2 LFM of Full-Length RrgA, RrgB and RrgC with Collagen I**

To further examine the interaction of RrgB FI with Col I, lateral force measurement [205] were carried out. RrgA FI, RrgB FI and RrgC FI were covalently and non-orientated attached to the tip of a rectangular AFM cantilever and Col I to a glass substrate using the same surface chemistry as for SMFS experiments. Note that the theory for lateral force calculation with the beam mechanics method is approximate in the sense that it uses simplified models of the cantilever, assumes a rotationally symmetric photodiode and contains uncertainties about the Young's modulus. However, as the assumptions, and thereby the error contribution, remain the same within all LFM experiments carried out with the same type of AFM cantilever, the results obtained for different tip functionalization can be compared to each other.

After subtracting the lateral force measured with no protein immobilized in the AFM tip, the results in figure 7.7 showed moderate interaction strength of RrgA FI with collagen fibrils of around 38 pN at scanning velocities of  $11\mu\text{m s}^{-1}$  and a contact force of 150 pN, similar to those determined in SMFS experiments, while the interaction of RrgC FI with Collagen I was once again negligible. However the lateral force of RrgB FI (at lateral tip velocities of  $11\mu\text{m s}^{-1}$  and a contact force of 150 pN) was 80 pN which was around 2.5-fold higher than in vertical force experiments. With the assumption that the adhesion may be a force-dependent interlocking of RrgB FI with collagen fibrils, the increase in lateral force may be interpreted as a consecutive catching of type I collagen fibrils by the pilus backbone protein leading to an intense lateral bending of the cantilever as it is scanned across the collagen coated surface. Other mechanisms, which exhibit conformational transitions during adhesion, have been reported for other bacterial adhesins interacting with collagens. In the "collagen hug" model the collagen triple helix is initially associated with the CnaA-N2 domain. The collagen is then wrapped by the N1–N2 linker and the CnaA-N1 domain and finally the C-terminal latch is introduced in the N1 domain to secure the ligand in place [177, 206].

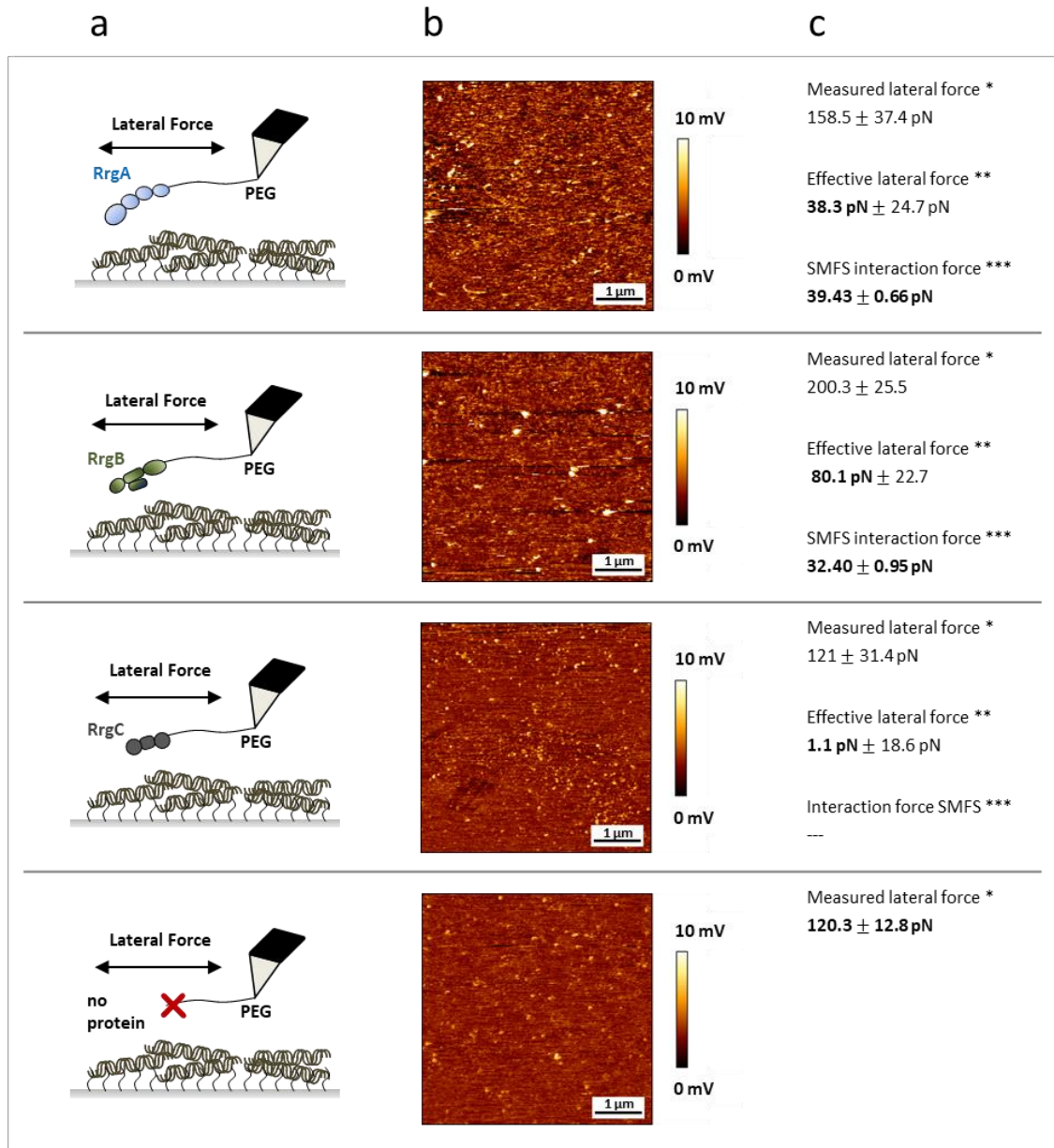


**Fig. 7.7 Lateral force microscopy of pneumococcal pilus-1 pilins with collagen I (Col I).**

(a) Illustration of lateral force microscopy (LFM) experiments with RrgA FI, RrgB FI, RrgC FI or no protein covalently attached to the AFM tip and Col I to the sample surface *via* hetero-bifunctional PEG spacers, respectively. (b) Representing lateral deflection images (trace) for each protein combination recorded with a rectangular cantilever. Experiments ( $n \geq 2$ ) were carried out applying a contact force of 150 pN and a scan velocity of  $\sim 11 \mu\text{m s}^{-1}$ . The normal cantilever sensitivity was similar for the shown images. (c) RrgA FI – Col I interactions result in a lateral force of around 38 pN, whereas the lateral interaction force for RrgB FI with Col I is with  $\sim 80$  pN about 2.5 times higher as in SMFS experiments. Lateral interaction of RrgC FI with Col I is negligible. \* Lateral forces were calculated from the lateral deflection signals (RMS Roughness) using the beam mechanic theory and the normal sensitivity (see Eq. 19). \*\* Effective lateral force for each protein combination was calculated through subtraction of the measured lateral force gained in experiments with no protein attached to the AFM tip. \*\*\* Interaction force as determined in SMFS experiments (see Fig. 7.6).

In contrast to RrgB FL, which domain D2 shows structure similarities to the CnaA and domain D3 to the CnaB fold [99], the Cna – collagen bond withstands remarkably high forces [28, 171], close to rupture forces of covalent bonds [151], that were not measurable for the RrgB FL - Col I interaction, assuming that the interaction of the pilus-1 backbone protein and Col I displays a somehow different binding mechanism as the Cna – collagen bond.

Like for SMFS experiment, side-directed coupling of RrgB FL *via* its N- or C-terminus to the cantilever tip and scanning over the collagen fibrils should result in a significant reduction or increase in lateral forces if interlocking is prevented or favored.

The *in vivo* significance of RrgA FL and RrgB FL collagen-binding capacity becomes significant once ECM components are available for interaction, especially after disruption of the epithelial barrier. For example, the respiratory distress syndrome comprises an increase in type I collagen content in lungs both of children and elderly [207, 208] and pilus-1 adhesion to Col I might be an additional bacterial factor favoring the invasion of the bacterium into this pre-stressed tissue [48]. However, RrgA might also facilitate adhesion to host surfaces at physiological Col I amounts in the presence of a capsule, which might only be possible to a lesser extent for RrgB, as a plurality of pilus-1 backbone proteins may be masked if the pneumococcal capsule is present [58]. However, RrgBs interaction with type I collagen may not only hinder the sweeping of *S. pneumoniae* from, but even push the bacterium closer to the host cell surface in shear flow conditions, permitting a more intimate and stronger attachment. Protein folds homologues to RrgB can, *e.g.*, be found in the major pilins of *B. cereus* [103], *C. diphtheriae* [104], *S. agalactiae* [97], and *Actinomyces oris* [106] but the lateral arrangement of the D3 domain to the pilus backbone seems to be rather unique for *S. pneumoniae*, possibly providing benefits over the other bacteria.



## 8 Conclusion and Outlook

The SMFS results show “that the pilus-1 tip protein RrgA of *Streptococcus pneumoniae* TIGR4 as well as its two terminal domains D3 and D4 bind to Fn. D3 and D4 bind independently to distinct binding sites on the Fn molecule. RrgA FI binds to Fn either through one single domain [D3 or D4] or with [the] two domains simultaneously, constituting a two domain binding mode and giving rise to double rupture events in the respective force–distance traces. Average bond lifetimes in the absence of force are in the order of a few hundred milliseconds, and both adhesion force and bond lifetime are unaffected by dual-domain binding and unbinding, which seems to be a sequential rather than a cooperative process. The fast dissociation rate of the RrgA FI–Fn bond enables the bacterium to rapidly detach and bind new receptor sites.” (Becke *et al.*, ACSnano, 2018 [105])

In addition, during SMFS and LFM experiments RrgA can bind to Col I with forces in the lower force range of typical receptor–ligand interactions. In concert, the pilus-1 tip protein RrgA, which protrudes from the protective capsule, may enable the pneumococci to establish and maintain an initial, but transient adhesion to Fn and Col I, allowing the bacterium to remain near the host tissue surface, *e.g.*, in shear force environments (Figure 8.1).

Furthermore, the results show that RrgB can bind to Col I with significantly stronger interactions established between RrgB and Col I in LFM than in SMFS experiments. Taking the structure of RrgB into account, an interlocking of its domain D3 with the collagen fibrils and a subsequent turning of domain D3 during pulling on the RrgB – Col I bond seems possible and could explain the regions of constant force right before bond rupture in respective force–distance traces (Fig. 7.6d, blue arrows). Combined with the fact that RrgB does not bind to Col I in standard binding assays, *e.g.* ELISA, [14, 21], force-dependent interlocking of RrgB in collagen fibrils may occur under shear flow conditions (Figure 8.2).

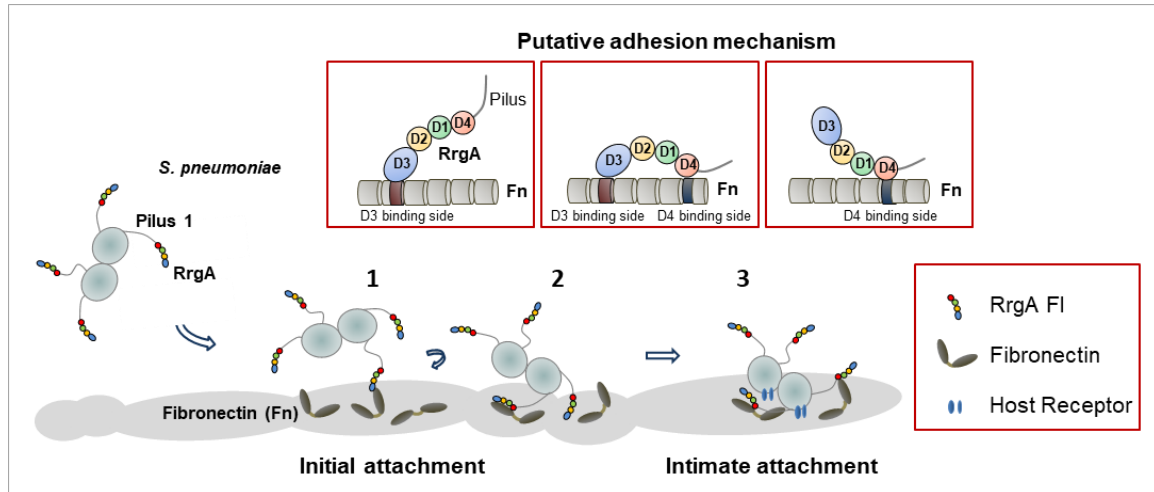


**Figure 8.1: Putative mechanism of *S. pneumoniae*–host adhesion mediated by pilus-1 RrgA–Fn binding.** Exposed pilus-1 adhesin RrgA enables the pneumococci to establish and maintain an initial but transient contact to fibronectin with short bond lifetimes (1). This allows the bacterium to remain near the host tissue surface, *e.g.*, in shear force environments (2) and scan for specific host receptors, providing a more intimate attachment to the host cells and thereby promoting infection (3). The proposed scheme provides a mechanistic picture of initial pilus-mediated host interaction, based on a model proposed by Telford *et al.*, Nat. Rev. Microbiol., 2006 [85], which is extended here by the ability of full length RrgA to bind to Fn either through single D3 or D4 domains or both domains simultaneously in a dual domain binding mode. The figure has been adapted from Becke *et al.*, ACSnano, 2018 [105].

Thereby RrgB, which seems to be in particular accessible if the pneumococcal capsule is (partly) dismantled, may not only hinder the sweeping of *S. pneumoniae* from host surfaces but even push the bacterium closer to the host cell surface under shear flow conditions. In concert with RrgA–Fn and RrgA–Col I interactions, this could allow the pathogen to further search host structures for more specific surface receptors which permit stronger attachment and, *e.g.*, promoting bacterial virulence [85].

These results expand our understanding of how Gram-positive pili adhere to host cells and the surrounding extracellular matrices and shed a light on one significant detail of pneumococcal invasion. Complementary studies on a cellular level carried out with surface plasmon resonance spectroscopy or a quartz crystal microbalance setup, might provide additional information on the role of pilus-1 mediated pathogen–host interaction. Repeating of SMFS and LFM experiments with side directed coupling of RrgB, *via* its N- or C-terminus to the cantilever tip, can simulate native-like shear flow conditions and give information about the effect of the pulling direction. Genetically engineering RrgBs, lacking the D3 domain, could clarify D3s role during interactions with host Col I.

As a tendency toward the spreading of piliated pneumococcal clones, as well as a general antibiotic resistance and vaccine escape have been reported lately [5, 18, 94, 95], and because pneumococcal infections can still be lethal, a detailed analysis can help to devise future strategies to control and possibly inhibit pilus-mediated bacterial adhesion to host cells and tissue and thereby prevent pneumococcal invasion and subsequent diseases.

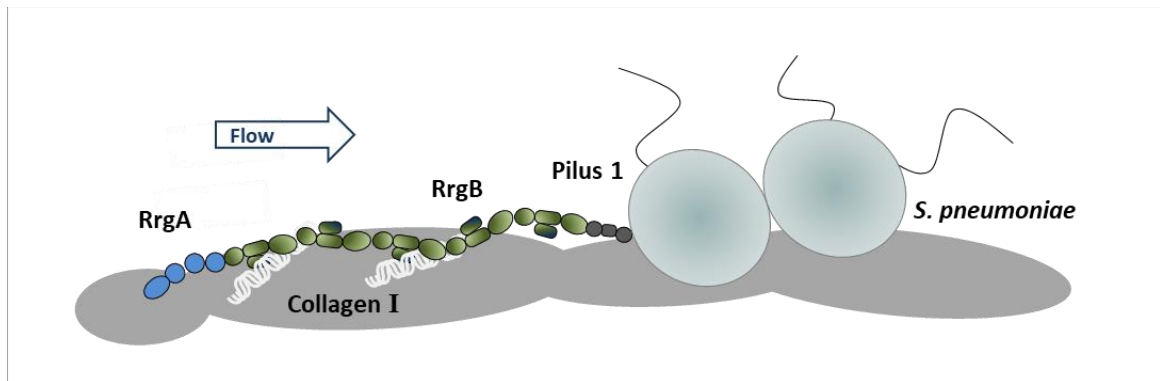


**Figure 8.2: Putative mechanism of *S. pneumoniae*–host adhesion mediated by pilus-1 RrgB–Col I binding.** Exposed pilus-1 RrgB may interlock with collagen fibres and thereby may not only hinder a sweeping of the pneumococcus from, but also push the bacterium closer to host surfaces in shear flow conditions in order to scan for specific host receptors promoting infection.





## 9 References

1. Henriques-Normark, B. and E.I. Tuomanen, *The Pneumococcus: Epidemiology, Microbiology, and Pathogenesis*. Cold Spring Harb Perspect Med, 2013. **3**(7).
2. Feldman, C. and R. Anderson, *Recent Advances in Our Understanding of Streptococcus Pneumoniae Infection*. F1000Prime Rep, 2014. **6**: p. 82.
3. Feldman, C. and R. Anderson, *Epidemiology, Virulence Factors and Management of the Pneumococcus*. F1000Res, 2016. **5**: p. 2320.
4. Mortality, G.B.D. and C. Causes of Death, *Global, Regional, and National Life Expectancy, All-Cause Mortality, and Cause-Specific Mortality for 249 Causes of Death, 1980-2015: a Systematic Analysis for the Global Burden of Disease Study 2015*. Lancet, 2016. **388**(10053): p. 1459-1544.
5. Kawaguchiya, M., et al., *Serotype Distribution, Antimicrobial Resistance and Prevalence of Pilus Islets in Pneumococci Following the Use of Conjugate Vaccines*. J Med Microbiol, 2017. **66**(5): p. 643-650.
6. Moore, M.R., et al., *Effect of Use of 13-Valent Pneumococcal Conjugate Vaccine in Children on Invasive Pneumococcal Disease in Children and Adults in the USA: Analysis of Multisite, Population-Based Surveillance*. Lancet Infect Dis, 2015. **15**(3): p. 301-9.
7. Andrews, N.J., et al., *Serotype-Specific Effectiveness and Correlates of Protection for the 13-Valent Pneumococcal Conjugate Vaccine: a Postlicensure Indirect Cohort Study*. Lancet Infect Dis, 2014. **14**(9): p. 839-46.
8. Stanek, R.J., N.B. Norton, and M.A. Mufson, *A 32-Year Study of the Effect of Pneumococcal Vaccines on Invasive Streptococcus pneumoniae Disease*. Am J Med Sci, 2016. **352**(6): p. 563-573.
9. Tomczyk, S., et al., *Prevention of Antibiotic-Nonsusceptible Invasive Pneumococcal Disease With the 13-Valent Pneumococcal Conjugate Vaccine*. Clin Infect Dis, 2016. **62**(9): p. 1119-25.
10. Kanwal, S., et al., *Mapping the Recognition Domains of Pneumococcal Fibronectin-Binding Proteins PavA and PavB Demonstrates a Common Pattern of Molecular Interactions with Fibronectin Type III Repeats*. Mol Microbiol, 2017. **105**(6): p. 839-859.
11. Iovino, F., et al., *PIgR and PECAM-1 Bind to Pneumococcal Adhesins RrgA and PspC Mediating Bacterial Brain Invasion*. J Exp Med, 2017. **214**(6): p. 1619-1630.
12. Orrskog, S., et al., *Pilus Adhesin RrgA Interacts with Complement Receptor 3, Thereby Affecting Macrophage Function and Systemic Pneumococcal Disease*. MBio, 2012. **4**(1): p. e00535-12.

## References

---

13. Basset, A., et al., *Toll-like Receptor (TLR) 2 Mediates Inflammatory Responses to Oligomerized RrgA Pneumococcal Pilus Type 1 Protein*. J Biol Chem, 2013. **288**(4): p. 2665-75.
14. Hilleringmann, M., et al., *Pneumococcal Pili Are Composed of Protofilaments Exposing Adhesive Clusters of Rrg A*. PLoS Pathog, 2008. **4**(3): p. e1000026.
15. Bagnoli, F., et al., *A Second Pilus Type in Streptococcus Pneumoniae Is Prevalent in Emerging Serotypes and Mediates Adhesion to Host Cells*. J Bacteriol, 2008. **190**(15): p. 5480-92.
16. Barocchi, M.A., et al., *A Pneumococcal Pilus Influences Virulence and Host Inflammatory Responses*. Proc Natl Acad Sci USA, 2006. **103**(8): p. 2857-62.
17. Hilleringmann, M., et al., *Molecular Architecture of Streptococcus Pneumoniae TIGR4 Pili*. EMBO J, 2009. **28**(24): p. 3921-30.
18. Aguiar, S.I., et al., *The Presence of the Pilus Locus Is a Clonal Property Among Pneumococcal Invasive Isolates*. BMC Microbiol, 2008. **8**: p. 41.
19. Selva, L., et al., *Prevalence and Clonal Distribution of PcpA, PsrP and Pilus-1 Among Pediatric Isolates of Streptococcus Pneumoniae*. PLoS One, 2012. **7**(7): p. e41587.
20. Moschioni, M., et al., *Streptococcus Pneumoniae Contains 3 rlrA Pilus Variants that Are Clonally Related*. J Infect Dis, 2008. **197**(6): p. 888-96.
21. Moschioni, M., et al., *The Two Variants of the Streptococcus Pneumoniae Pilus 1 RrgA Adhesin Retain the Same Function and Elicit Cross-Protection In Vivo*. Infect Immun, 2010. **78**(12): p. 5033-42.
22. Weisenhorn, A.L., Hansma, P.K., Albrecht, T.R., Quate, C.F, *Forces in Atomic Force Microscopy in Air and Water*. Applied Physics Letters, 1989. **54**(26): p. 2651-2653.
23. Rief, M., et al., *Single Molecule Force Spectroscopy on Polysaccharides by Atomic Force Microscopy*. Science, 1997. **275**(5304): p. 1295-7.
24. Rief, M., et al., *Reversible Unfolding of Individual Titin Immunoglobulin Domains by AFM*. Science, 1997. **276**(5315): p. 1109-12.
25. Grandbois, M., et al., *How Strong Is a Covalent Bond?* Science, 1999. **283**(5408): p. 1727-30.
26. Sullan, R.M., et al., *Single-Cell Force Spectroscopy of Pili-Mediated Adhesion*. Nanoscale, 2014. **6**(2): p. 1134-43.
27. Bustanji, Y., et al., *Dynamics of the Interaction Between a Fibronectin Molecule and a Living Bacterium Under Mechanical Force*. Proc Natl Acad Sci U S A, 2003. **100**(23): p. 13292-7.
28. Valotteau, C., et al., *Single-Cell and Single-Molecule Analysis Unravels the Multifunctionality of the Staphylococcus aureus Collagen-Binding Protein Cna*. ACS Nano, 2017. **11**(2): p. 2160-2170.
29. Binnig, G., C.F. Quate, and C. Gerber, *Atomic Force Microscope*. Phys Rev Lett, 1986. **56**(9): p. 930-933.

30. Touhami, A., et al., *Nanoscale Characterization and Determination of Adhesion Forces of Pseudomonas Aeruginosa Pili by Using Atomic Force Microscopy*. J Bacteriol, 2006. **188**(2): p. 370-7.
31. Beaussart, A., et al., *Nanoscale Adhesion Forces of Pseudomonas Aeruginosa Type IV Pili*. ACS Nano, 2014. **8**(10): p. 10723-33.
32. Biais, N., et al., *Force-Dependent Polymorphism in Type IV Pili Reveals Hidden Epitopes*. Proc Natl Acad Sci U S A, 2010. **107**(25): p. 11358-63.
33. Miller, E., et al., *The Mechanical Properties of E. coli Type 1 Pili Measured by Atomic Force Microscopy Techniques*. Biophys J, 2006. **91**(10): p. 3848-56.
34. Lugmaier, R.A., et al., *Dynamic Restacking of Escherichia Coli P-Pili*. Eur Biophys J, 2008. **37**(2): p. 111-20.
35. Frantz, C., K.M. Stewart, and V.M. Weaver, *The Extracellular Matrix at a Glance*. J Cell Sci, 2010. **123**(Pt 24): p. 4195-200.
36. Henderson, B., et al., *Fibronectin: a Multidomain Host Adhesin Targeted by Bacterial Fibronectin-Binding Proteins*. FEMS Microbiol Rev, 2011. **35**(1): p. 147-200.
37. Brodsky, B. and A.V. Persikov, *Molecular Structure of the Collagen Triple Helix*. Adv Protein Chem, 2005. **70**: p. 301-39.
38. Bustamante, C., et al., *Entropic Elasticity of Lambda-Phage DNA*. Science, 1994. **265**(5178): p. 1599-600.
39. Janshoff, A., et al., *Force Spectroscopy of Molecular Systems-Single Molecule Spectroscopy of Polymers and Biomolecules*. Angew Chem Int Ed Engl, 2000. **39**(18): p. 3212-3237.
40. Wang, M.D., et al., *Stretching DNA With Optical Tweezers*. Biophys J, 1997. **72**(3): p. 1335-46.
41. Bell, G.I., *Models for the Specific Adhesion of Cells to Cells*. Science, 1978. **200**(4342): p. 618-27.
42. Evans, E. and K. Ritchie, *Dynamic Strength of Molecular Adhesion Bonds*. Biophys J, 1997. **72**(4): p. 1541-55.
43. E. Liu, B.B., J.P. Celis, *Calibration Procedures for Frictional Measurements With a Lateral Force Microscope*. Wear, 1996. **192**(1-2): p. 141-150.
44. John E. Sader, I.L., Paul Mulvaney, *Method for the Calibration of Atomic Force Microscope Cantilevers*. Review of Scientific Instruments, 1995. **66**(7).
45. John E. Sader, J.W.M.C., Paul Mulvaney, *Calibration of Rectangular Atomic Force Microscope Cantilevers*. Review of Scientific Instruments, 1999. **70**(10).
46. White, B., *The Biology of Pneumococcus*. The Commonwealth Fund, New York, NY., 1938.
47. O'Brien, K.L., et al., *Burden of Disease Caused by Streptococcus Pneumoniae in Children Younger Than 5 Years: Global Estimates*. Lancet, 2009. **374**(9693): p. 893-902.

## References

---

48. Torres, A., et al., *Risk Factors for Community-Acquired Pneumonia in Adults in Europe: a literature review*. Thorax, 2013. **68**(11): p. 1057-65.
49. Robinson, K.A., et al., *Epidemiology of Invasive Streptococcus Pneumoniae Infections in the United States, 1995-1998: Opportunities for Prevention in the Conjugate Vaccine Era*. JAMA, 2001. **285**(13): p. 1729-35.
50. Prevention, C.f.D.C.a., *Active Bacterial Core Surveillance Report, Emerging Infections Program Network, Streptococcus pneumoniae*. 2015.
51. Geno, K.A., et al., *Pneumococcal Capsules and Their Types: Past, Present, and Future*. Clin Microbiol Rev, 2015. **28**(3): p. 871-99.
52. Calix, J.J., et al., *Biochemical, Genetic, and Serological Characterization of Two Capsule Subtypes Among Streptococcus Pneumoniae Serotype 20 Strains: Discovery of a New Pneumococcal Serotype*. J Biol Chem, 2012. **287**(33): p. 27885-94.
53. Feikin, D.R., et al., *Serotype-Specific Changes in Invasive Pneumococcal Disease After Pneumococcal Conjugate Vaccine Introduction: a Pooled Analysis of Multiple Surveillance Sites*. PLoS Med, 2013. **10**(9): p. e1001517.
54. Galanis, I., et al., *Effects of PCV7 and PCV13 on Invasive Pneumococcal Disease and Carriage in Stockholm, Sweden*. Eur Respir J, 2016. **47**(4): p. 1208-18.
55. Farrell, D.J., K.P. Klugman, and M. Pichichero, *Increased Antimicrobial Resistance Among Nonvaccine Serotypes of Streptococcus Pneumoniae in the Pediatric Population After the Introduction of 7-Valent Pneumococcal Vaccine in the United States*. Pediatr Infect Dis J, 2007. **26**(2): p. 123-8.
56. Naucler, P., et al., *Comparison of the Impact of Pneumococcal Conjugate Vaccine 10 or Pneumococcal Conjugate Vaccine 13 on Invasive Pneumococcal Disease in Equivalent Populations*. Clin Infect Dis, 2017. **65**(11): p. 1780-1789.
57. WHO, *Fact Sheet, Immunization coverage*. 2017.  
<http://www.who.int/news-room/fact-sheets/detail/immunization-coverage>  
accessed on 13.10.2018
58. Weiser, J.N., *Phase Variation in Colony Opacity by Streptococcus Pneumoniae*. Microb Drug Resist, 1998. **4**(2): p. 129-35.
59. Moscoso, M., E. Garcia, and R. Lopez, *Pneumococcal Biofilms*. Int Microbiol, 2009. **12**(2): p. 77-85.
60. Trappetti, C., et al., *Extracellular Matrix Formation Enhances the Ability of Streptococcus Pneumoniae to Cause Invasive Disease*. PLoS One, 2011. **6**(5): p. e19844.
61. Hyams, C., et al., *The Streptococcus Pneumoniae Capsule Inhibits Complement Activity and Neutrophil Phagocytosis by Multiple Mechanisms*. Infect Immun, 2010. **78**(2): p. 704-15.

62. Wartha, F., et al., *Capsule and D-alanylated Lipoteichoic Acids Protect Streptococcus Pneumoniae Against Neutrophil Extracellular Traps*. Cell Microbiol, 2007. **9**(5): p. 1162-71.
63. Nelson, A.L., et al., *Capsule Enhances Pneumococcal Colonization by Limiting Mucus-Mediated Clearance*. Infect Immun, 2007. **75**(1): p. 83-90.
64. Bootsma, H.J., M. Egmont-Petersen, and P.W. Hermans, *Analysis of the in Vitro Transcriptional Response of Human Pharyngeal Epithelial Cells to Adherent Streptococcus Pneumoniae: Evidence for a Distinct Response to Encapsulated Strains*. Infect Immun, 2007. **75**(11): p. 5489-99.
65. Bean, B. and A. Tomasz, *Choline Metabolism in Pneumococci*. J Bacteriol, 1977. **130**(1): p. 571-4.
66. Denapaite, D., et al., *Biosynthesis of Teichoic Acids in Streptococcus Pneumoniae and Closely Related Species: Lessons from Genomes*. Microb Drug Resist, 2012. **18**(3): p. 344-58.
67. Hakenbeck, R., et al., *Versatility of Choline Metabolism and Choline-Binding Proteins in Streptococcus Pneumoniae and Commensal Streptococci*. FEMS Microbiol Rev, 2009. **33**(3): p. 572-86.
68. Young, N.M., S.J. Foote, and W.W. Wakarchuk, *Review of Phosphocholine Substituents on Bacterial Pathogen Glycans: Synthesis, Structures and Interactions with Host Proteins*. Mol Immunol, 2013. **56**(4): p. 563-73.
69. Perez-Dorado, I., S. Galan-Bartual, and J.A. Hermoso, *Pneumococcal Surface Proteins: When the Whole Is Greater Than the Sum of Its Parts*. Mol Oral Microbiol, 2012. **27**(4): p. 221-45.
70. Hilleringmann, M.K., Sylvia & Gámez, Gustavo, Hammerschmidt, Sven., *Pneumococcal Pili and Adhesins*, in *Streptococcus Pneumoniae*, S.H. Jeremy Brown, Carlos Orihuela, Editor. 2015, Jeremy Brown Sven Hammerschmidt Carlos Orihuela. p. 309-346.
71. Paterson, G.K. and C.J. Orihuela, *Pneumococcal Microbial Surface Components Recognizing Adhesive Matrix Molecules Targeting of the Extracellular Matrix*. Mol Microbiol, 2010. **77**(1): p. 1-5.
72. Holmes, A.R., et al., *The PavA Gene of Streptococcus Pneumoniae Encodes a Fibronectin-Binding Protein that is Essential for Virulence*. Mol Microbiol, 2001. **41**(6): p. 1395-408.
73. Hammerschmidt, S., et al., *Identification of Pneumococcal Surface Protein A as a Lactoferrin-Binding Protein of Streptococcus Pneumoniae*. Infect Immun, 1999. **67**(4): p. 1683-7.
74. Ren, B., et al., *Both Family 1 and Family 2 PspA Proteins Can Inhibit Complement Deposition and Confer Virulence to a Capsular Serotype 3 Strain of Streptococcus Pneumoniae*. Infect Immun, 2003. **71**(1): p. 75-85.

## References

---

75. Kerr, A.R., et al., *The Contribution of PspC to Pneumococcal Virulence Varies Between Strains and Is Accomplished by Both Complement Evasion and Complement-Independent Mechanisms*. *Infect Immun*, 2006. **74**(9): p. 5319-24.
76. Hammerschmidt, S., et al., *The Host Immune Regulator Factor H Interacts via Two Contact Sites with the PspC Protein of Streptococcus Pneumoniae and Mediates Adhesion to Host Epithelial Cells*. *J Immunol*, 2007. **178**(9): p. 5848-58.
77. Orihuela, C.J., et al., *Laminin Receptor Initiates Bacterial Contact with the Blood Brain Barrier in Experimental Meningitis Models*. *J Clin Invest*, 2009. **119**(6): p. 1638-46.
78. Anderton, J.M., et al., *E-cadherin Is a Receptor for the Common Protein Pneumococcal Surface Adhesin A (PsaA) of Streptococcus Pneumoniae*. *Microb Pathog*, 2007. **42**(5-6): p. 225-36.
79. King, S.J., K.R. Hippe, and J.N. Weiser, *Deglycosylation of Human Glycoconjugates by the Sequential Activities of Exoglycosidases Expressed by Streptococcus Pneumoniae*. *Mol Microbiol*, 2006. **59**(3): p. 961-74.
80. Jensch, I., et al., *PavB Is a Surface-Exposed Adhesin of Streptococcus Pneumoniae Contributing to Nasopharyngeal Colonization and Airways Infections*. *Mol Microbiol*, 2010. **77**(1): p. 22-43.
81. Paterson, G.K., et al., *PclA, a Pneumococcal Collagen-Like Protein with Selected Strain Distribution, Contributes to Adherence and Invasion of Host Cells*. *FEMS Microbiol Lett*, 2008. **285**(2): p. 170-6.
82. Yamaguchi, M., et al., *PfbA, a Novel Plasmin- and Fibronectin-Binding Protein of Streptococcus Pneumoniae, Contributes to Fibronectin-Dependent Adhesion and Antiphagocytosis*. *J Biol Chem*, 2008. **283**(52): p. 36272-9.
83. Beulin, D.S.J., et al., *Streptococcus Pneumoniae Surface Protein PfbA Is a Versatile Multidomain and Multiligand-Binding Adhesin Employing Different Binding Mechanisms*. *FEBS J*, 2017. **284**(20): p. 3404-3421.
84. Proft, T. and E.N. Baker, *Pili in Gram-Negative and Gram-Positive Bacteria - Structure, Assembly and Their Role in Disease*. *Cell Mol Life Sci*, 2009. **66**(4): p. 613-35.
85. Telford, J.L., et al., *Pili in Gram-Positive Pathogens*. *Nat Rev Microbiol*, 2006. **4**(7): p. 509-19.
86. Shaik, M.M., et al., *A Structural Snapshot of Type II Pilus Formation in Streptococcus Pneumoniae*. *J Biol Chem*, 2015. **290**(37): p. 22581-92.
87. LeMieux, J., et al., *RrgA and RrgB Are Components of a Multisubunit Pilus Encoded by the Streptococcus Pneumoniae rlrA Pathogenicity Islet*. *Infect Immun*, 2006. **74**(4): p. 2453-6.
88. Izore, T., et al., *Structural Basis of Host Cell Recognition by the Pilus Adhesin from Streptococcus Pneumoniae*. *Structure*, 2010. **18**(1): p. 106-15.

89. El Mortaji, L., et al., *The Full-Length Streptococcus Pneumoniae Major Pilin RrgB Crystallizes in a Fibre-Like Structure, which Presents the D1 Isopeptide Bond and Provides Details on the Mechanism of Pilus Polymerization*. *Biochem J*, 2012. **441**(3): p. 833-41.
90. Shaik, M.M., et al., *Structural Basis of Pilus Anchoring by the Ancillary Pilin RrgC of Streptococcus Pneumoniae*. *J Biol Chem*, 2014. **289**(24): p. 16988-97.
91. Kang, H.J. and E.N. Baker, *Intramolecular Isopeptide Bonds: Protein Crosslinks Built for Stress?* *Trends Biochem Sci*, 2011. **36**(4): p. 229-37.
92. El Mortaji, L., et al., *Stability and Assembly of Pilus Subunits of Streptococcus Pneumoniae*. *J Biol Chem*, 2010. **285**(16): p. 12405-15.
93. Gianfaldoni, C., et al., *Streptococcus Pneumoniae Pilus Subunits Protect Mice Against Lethal Challenge*. *Infect Immun*, 2007. **75**(2): p. 1059-62.
94. Khodaei, F., et al., *The Dominance of Pilus Islet 1 in Pneumococcal Isolates Collected From Patients and Healthy Individuals*. *Jundishapur J Microbiol*, 2016. **9**(5): p. e30470.
95. Figueira, M., et al., *Variation of Pneumococcal Pilus-1 Expression Results in Vaccine Escape During Experimental Otitis Media [EOM]*. *PLoS One*, 2014. **9**(1): p. e83798.
96. Krishnan, V., et al., *Structure of Streptococcus Agalactiae Tip Pilin GBS104: a Model for GBS Pili Assembly and Host Interactions*. *Acta Crystallogr D Biol Crystallogr*, 2013. **69**(Pt 6): p. 1073-89.
97. Krishnan, V., et al., *An IgG-Like Domain in the Minor Pilin GBS52 of Streptococcus Agalactiae Mediates Lung Epithelial Cell Adhesion*. *Structure*, 2007. **15**(8): p. 893-903.
98. Smith, W.D., et al., *Roles of Minor Pilin Subunits Spy0125 and Spy0130 in the Serotype M1 Streptococcus Pyogenes Strain SF370*. *J Bacteriol*, 2010. **192**(18): p. 4651-9.
99. Deivanayagam, C.C., et al., *Novel Fold and Assembly of the Repetitive B Region of the Staphylococcus Aureus Collagen-Binding Surface Protein*. *Structure*, 2000. **8**(1): p. 67-78.
100. Whittaker, C.A. and R.O. Hynes, *Distribution and Evolution of von Willebrand/integrin A Domains: Widely Dispersed Domains with Roles in Cell Adhesion and Elsewhere*. *Mol Biol Cell*, 2002. **13**(10): p. 3369-87.
101. Spraggon, G., et al., *Supramolecular Rrganization of the Repetitive Backbone Unit of the Streptococcus Pneumoniae Pilus*. *PLoS One*, 2010. **5**(6): p. e10919.
102. Paterson, N.G. and E.N. Baker, *Structure of the Full-Length Major Pilin from Streptococcus Pneumoniae: Implications for Isopeptide Bond Formation in Gram-Positive Bacterial Pili*. *PLoS One*, 2011. **6**(7): p. e22095.
103. Budzik, J.M., et al., *Intramolecular Amide Bonds Stabilize Pili on the Surface of Bacilli*. *Proc Natl Acad Sci U S A*, 2009. **106**(47): p. 19992-7.

## References

---

104. Kang, H.J., et al., *The Corynebacterium Diphtheriae Shaft Pilin SpaA Is Built of Tandem Ig-Like Modules with Stabilizing Isopeptide and Disulfide Bonds*. Proc Natl Acad Sci U S A, 2009. **106**(40): p. 16967-71.
105. Becke, T.D., et al., *Single Molecule Force Spectroscopy Reveals Two-Domain Binding Mode of Pilus-1 Tip Protein RrgA of Streptococcus Pneumoniae to Fibronectin*. ACS Nano, 2018. **12**(1): p. 549-558.
106. Persson, K., et al., *The Pilin Protein FimP from Actinomyces Oris: Crystal Structure and Sequence Analyses*. PLoS One, 2012. **7**(10): p. e48364.
107. Dufrene, Y.F., et al., *Imaging Modes of Atomic Force Microscopy for Application in Molecular and Cell Biology*. Nat Nanotechnol, 2017. **12**(4): p. 295-307.
108. Jalili N., L.K., *A Review of Atomic Force Microscopy Imaging Systems: Application to Molecular Metrology and Biological Sciences*. Mechatronics, 2004. **14**(8): p. 907-945.
109. Tripathi, P., et al., *Adhesion and Nanomechanics of Pili from the Probiotic Lactobacillus Rhamnosus GG*. ACS Nano, 2013. **7**(4): p. 3685-97.
110. Milles, L.F., et al., *Molecular Mechanism of Extreme Mechanostability in a Pathogen Adhesin*. Science, 2018. **359**(6383): p. 1527-1533.
111. Butt, H.J.a.J., M. , *Calculation of Thermal Noise in Atomic Force Microscopy*. Nanotechnology, 1995. **6**(1): p. 1-7.
112. Bechhoefer, J.L.H.a.J., *Calibration of Atomic-Force Microscope Tips*. Review of Scientific Instruments, 1993. **64**.
113. Bouchiat, C., et al., *Estimating the Persistence Length of a Worm-Like Chain Molecule from Force-Extension Measurements*. Biophys J, 1999. **76**(1 Pt 1): p. 409-13.
114. M. Menzinger, R.W., *The Meaning and Use of the Arrhenius Activation Energy*. Angewandte Chemie International Edition, 1969. **8**(6): p. 438-444.
115. Arrhenius, S., *Über die Reaktionsgeschwindigkeit bei der Inversion von Rohrzucker durch Säuren*. Zeitschrift für Physikalische Chemie, 1889. **4**: p. 226-248.
116. Hoff, J.H.v.t., *Etudes de Dynamique Chimique*. Frederik Muller and Co., Amsterdam, 1884: p. 114-118.
117. Merkel, R., et al., *Energy Landscapes of Receptor-Ligand Bonds Explored with Dynamic Force Spectroscopy*. Nature, 1999. **397**(6714): p. 50-3.
118. Taninaka, A., et al., *Force Measurement Enabling Precise Analysis by Dynamic Force Spectroscopy*. Int J Mol Sci, 2012. **13**(1): p. 453-65.
119. Friddle, R.W., A. Noy, and J.J. De Yoreo, *Interpreting the Widespread Nonlinear Force Spectra of Intermolecular Bonds*. Proc Natl Acad Sci U S A, 2012. **109**(34): p. 13573-8.
120. Hummer, G. and A. Szabo, *Kinetics from Nonequilibrium Single-Molecule Pulling Experiments*. Biophys J, 2003. **85**(1): p. 5-15.



121. Dudko, O.K., G. Hummer, and A. Szabo, *Intrinsic Rates and Activation Free Energies from Single-Molecule Pulling Experiments*. Phys Rev Lett, 2006. **96**(10): p. 108101.
122. Bennewitz, R., *Friction Force Microscopy*. Materials Today, 2005. **8**(5): p. 42-48.
123. Christopher P. Green, H.L., Jason P. Cleveland, Roger Proksch, Paul Mulvaney, John E. Sader, *Normal and Torsional Spring Constants of Atomic Force Microscope Cantilevers*. Review of Scientific Instruments, 2004. **75**(6).
124. Liu, W., K. Bonin, and M. Guthold, *Easy and direct method for calibrating atomic force microscopy lateral force measurements*. Rev Sci Instrum, 2007. **78**(6): p. 063707.
125. J.E. Munguía-Cervantes , J.V.M.-M., H.F. Mendoza-León, M.A. Alemán-Arce, *Si<sub>3</sub>N<sub>4</sub> Young's Modulus Measurement from Microcantilever Beams Using a Calibrated Stylus Profiler*. Superficies y Vacío, 2017. **30**(1).
126. A. Khan, J.P., and P. Hess, *Young's Modulus of Silicon Nitride Used in Scanning Force Microscope Cantilevers*. Journal of Applied Physics, 2004. **95**(4).
127. Khashayar Babaei Gavan, H.J.R.W., Emile W. J. M. van der Drift, and a.H.S.J.v.d.Z. Warner J. Venstra, *Size-Dependent Effective Young's Modulus of Silicon Nitride Cantilevers*. Applied Physics Letters, 2009. **94**(23).
128. D. F. Ogletree, R.W.C., Miguel Salmeron, *Calibration of Frictional Forces in Atomic Force Microscopy*. Review of Scientific Instruments, 1996. **67**(9).
129. M. Varenberg, I.E., and G. Halperin, *An Improved Wedge Calibration Method for Lateral Force in Atomic Force Microscopy*. Review of Scientific Instruments, 2003. **74**(7).
130. Wang, H. and M.L. Gee, *AFM Lateral Force Calibration for an Integrated Probe Using a Calibration Grating*. Ultramicroscopy, 2014. **136**: p. 193-200.
131. Dziekonski, C., W. Dera, and D.M. Jarzabek, *Method for Lateral Force Calibration in Atomic Force Microscope Using MEMS Microforce Sensor*. Ultramicroscopy, 2017. **182**: p. 1-9.
132. Becke, T.D., et al., *Covalent Immobilization of Proteins for the Single Molecule Force Spectroscopy*. J Vis Exp, 2018(138).
133. Zimmermann, J.L., et al., *Thiol-Based, Site-Specific and Covalent Immobilization of Biomolecules for Single-Molecule Experiments*. Nat Protoc, 2010. **5**(6): p. 975-85.
134. Schmidt, S.W., et al., *Simple Coupling Chemistry Linking Carboxyl-Containing Organic Molecules to Silicon Oxide Surfaces Under Acidic Conditions*. Langmuir, 2010. **26**(19): p. 15333-8.
135. Stetter, F.W., et al., *Investigating Single Molecule Adhesion by Atomic Force Spectroscopy*. J Vis Exp, 2015(96): p. e52456.
136. Jobst, M.A., et al., *Investigating Receptor-Ligand Systems of the Cellulosome with AFM-Based Single-Molecule Force Spectroscopy*. J Vis Exp, 2013(82): p. e50950.

## References

---

137. Vitry, P., et al., *Force-Induced Strengthening of the Interaction between Staphylococcus aureus Clumping Factor B and Loricrin*. MBio, 2017. **8**(6).
138. Herman-Bausier, P., et al., *Fibrinogen Activates the Capture of Human Plasminogen by Staphylococcal Fibronectin-Binding Proteins*. MBio, 2017. **8**(5).
139. Hinterdorfer, P., et al., *Detection and Localization of Individual Antibody-Antigen Recognition Events by Atomic Force Microscopy*. Proceedings of the National Academy of Sciences of the United States of America, 1996. **93**(8): p. 3477-3481.
140. Hinterdorfer, P., et al., *Conjugation of Biomolecules to Tip and Probe Surfaces for Molecular Recognition in Atomic Force Microscopy*. European Journal of Cell Biology, 1997. **74**: p. 72-72.
141. Riener, C.K., et al., *Heterobifunctional Crosslinkers for Tethering Single Ligand Molecules to Scanning Probes*. Analytica Chimica Acta, 2003. **497**(1-2): p. 101-114.
142. Ebner, A., et al., *A New, Simple Method for Linking of Antibodies to Atomic Force Microscopy Tips*. Bioconjugate Chemistry, 2007. **18**(4): p. 1176-1184.
143. Ott, W., et al., *Elastin-like Polypeptide Linkers for Single-Molecule Force Spectroscopy*. ACS Nano, 2017. **11**(6): p. 6346-6354.
144. Ott, W., et al., *Single-Molecule Force Spectroscopy on Polyproteins and Receptor-Ligand Complexes: The Current Toolbox*. Journal of Structural Biology, 2017. **197**(1): p. 3-12.
145. Metwalli, E., et al., *Surface Characterizations of Mono-, Di-, and Tri-Aminosilane Treated Glass Substrates*. J Colloid Interface Sci, 2006. **298**(2): p. 825-31.
146. D.Beyer, W.K., H.Ringsdorf, G.Elender, E.Sackmann, *Covalently Attached Polymer Mono- and Multilayers on Silanized Glass Substrates*. Thin Solid Films, 1996. **284–285**: p. 825-828.
147. Hermanson, G.T., *Chapter 13 – Silane Coupling Agents*, in *Bioconjugate Techniques* 2013, Academic Press. p. 535–548.
148. Howarter, J.A. and J.P. Youngblood, *Optimization of Silica Silanization by 3-Aminopropyltriethoxysilane*. Langmuir, 2006. **22**(26): p. 11142-7.
149. Hermanson, G.T., *Chapter 6 – Heterobifunctional Crosslinkers*, in *Bioconjugate Techniques*. 2013, Academic Press. p. 299–339.
150. Sehgal, D. and I.K. Vijay, *A Method for the High Efficiency of Water-Soluble Carbodiimide-Mediated Amidation*. Anal Biochem, 1994. **218**(1): p. 87-91.
151. Schmidt, S.W., M.K. Beyer, and H. Clausen-Schaumann, *Dynamic Strength of the Silicon-Carbon Bond Observed over Three Decades of Force-Loading Rates*. J Am Chem Soc, 2008. **130**(11): p. 3664-8.
152. Schmidt, S.W., et al., *Single-Molecule Force-Clamp Experiments Reveal Kinetics of Mechanically Activated Silyl Ester Hydrolysis*. ACS Nano, 2012. **6**(2): p. 1314-21.

153. Schmidt, S.W., et al., *Mechanically activated rupture of single covalent bonds: evidence of force induced bond hydrolysis*. *Phys Chem Chem Phys*, 2011. **13**(13): p. 5994-9.
154. Schmidt, S.W., et al., *Mechanically Induced Silyl Ester Cleavage Under Acidic Conditions Investigated by AFM-Based Single-Molecule Force Spectroscopy in the Force-Ramp Mode*. *Faraday Discuss*, 2014. **170**: p. 357-67.
155. Alsteens, D., et al., *Atomic Force Microscopy-Based Characterization and Design of Biointerfaces*. *Nature Reviews Materials*, 2017. **2**: p. 17008.
156. Dufrene, Y.F., *Sticky Microbes: Forces in Microbial Cell Adhesion*. *Trends Microbiol*, 2015. **23**(6): p. 376-82.
157. Herman-Bausier, P., et al., *Forces Guiding Staphylococcal Adhesion*. *J Struct Biol*, 2017. **197**(1): p. 65-69.
158. Oh, Y.J., et al., *Curli Mediate Bacterial Adhesion to Fibronectin via Tensile Multiple Bonds*. *Sci Rep*, 2016. **6**: p. 33909.
159. El-Kirat-Chatel, S., et al., *Single-Molecule Analysis of Pseudomonas Fluorescens Footprints*. *ACS Nano*, 2014. **8**(2): p. 1690-8.
160. Gunning, A.P., et al., *Use of Atomic Force Microscopy to Study the Multi-Modular Interaction of Bacterial Adhesins to Mucins*. *Int J Mol Sci*, 2016. **17**(11).
161. Echelman, D.J., A.Q. Lee, and J.M. Fernandez, *Mechanical Forces Regulate the Reactivity of a Thioester Bond in a Bacterial Adhesin*. *J Biol Chem*, 2017. **292**(21): p. 8988-8997.
162. Sullan, R.M., et al., *Binding Forces of Streptococcus Mutans P1 Adhesin*. *ACS Nano*, 2015. **9**(2): p. 1448-60.
163. Hull, J.R., G.S. Tamura, and D.G. Castner, *Interactions of the Streptococcal C5a Peptidase with Human Fibronectin*. *Acta Biomater*, 2008. **4**(3): p. 504-13.
164. Herman, P., et al., *The Binding Force of the Staphylococcal Adhesin SdrG Is Remarkably Strong*. *Mol Microbiol*, 2014. **93**(2): p. 356-68.
165. Casillas-Ituarte, N.N., et al., *Amino Acid Polymorphisms in the Fibronectin-Binding Repeats of Fibronectin-Binding Protein A Affect Bond Strength and Fibronectin Conformation*. *J Biol Chem*, 2017. **292**(21): p. 8797-8810.
166. Meenan, N.A., et al., *The Tandem Beta-Zipper Model Defines High Affinity Fibronectin-Binding Repeats within Staphylococcus Aureus FnBPA*. *J Biol Chem*, 2007. **282**(35): p. 25893-902.
167. Mitchell, G., et al., *Staphylococcus Aureus SigB Activity Promotes a Strong Fibronectin-Bacterium Interaction which May Sustain Host Tissue Colonization by Small-Colony Variants Isolated from Cystic Fibrosis Patients*. *Mol Microbiol*, 2008. **70**(6): p. 1540-55.

## References

---

168. Buck, A.W., et al., *Bonds Between Fibronectin and Fibronectin-Binding Proteins on Staphylococcus Aureus and Lactococcus Lactis*. Langmuir, 2010. **26**(13): p. 10764-70.
169. Xiong, Y.Q., et al., *Endovascular Infections Caused by Methicillin-Resistant Staphylococcus Aureus Are Linked to Clonal Complex-Specific Alterations in Binding and Invasion Domains of Fibronectin-Binding Protein A as well as the Occurrence of FnbB*. Infect Immun, 2015. **83**(12): p. 4772-80.
170. Fleury, O.M., et al., *Clumping Factor B Promotes Adherence of Staphylococcus aureus to Corneocytes in Atopic Dermatitis*. Infect Immun, 2017. **85**(6).
171. Herman-Bausier, P., et al., *Mechanical Strength and Inhibition of the Staphylococcus aureus Collagen-Binding Protein Cna*. MBio, 2016. **7**(5).
172. Casillas-Ituarte, N.N., et al., *Dissociation Rate Constants of Human Fibronectin Binding to Fibronectin-Binding Proteins on Living Staphylococcus Aureus Isolated from Clinical Patients*. J Biol Chem, 2012. **287**(9): p. 6693-701.
173. Formosa-Dague, C., et al., *Zinc-Dependent Mechanical Properties of Staphylococcus Aureus Biofilm-Forming Surface Protein SasG*. Proc Natl Acad Sci U S A, 2016. **113**(2): p. 410-5.
174. Formosa-Dague, C., et al., *Sticky Matrix: Adhesion Mechanism of the Staphylococcal Polysaccharide Intercellular Adhesin*. ACS Nano, 2016. **10**(3): p. 3443-52.
175. Feuillie, C., et al., *Molecular Interactions and Inhibition of the Staphylococcal Biofilm-Forming Protein SdrC*. Proc Natl Acad Sci U S A, 2017. **114**(14): p. 3738-3743.
176. Bowden, M.G., et al., *Evidence for the "Dock, Lock, and Latch" Ligand Binding Mechanism of the Staphylococcal Microbial Surface Component Recognizing Adhesive Matrix Molecules (MSCRAMM) SdrG*. J Biol Chem, 2008. **283**(1): p. 638-47.
177. Zong, Y., et al., *A 'Collagen Hug' Model for Staphylococcus Aureus CNA Binding to Collagen*. EMBO J, 2005. **24**(24): p. 4224-36.
178. Le Trong, I., et al., *Structural Basis for Mechanical Force Regulation of the Adhesin FimH via Finger Trap-Like Beta Sheet Twisting*. Cell, 2010. **141**(4): p. 645-55.
179. Yakovenko, O., et al., *FimH Forms Catch Bonds that Are Enhanced by Mechanical Force Due to Allosteric Regulation*. J Biol Chem, 2008. **283**(17): p. 11596-605.
180. Schoeler, C., et al., *Ultrastable Cellulosome-Adhesion Complex Tightens Under Load*. Nat Commun, 2014. **5**: p. 5635.
181. Foster, T.J., *The Remarkably Multifunctional Fibronectin Binding Proteins of Staphylococcus Aureus*. Eur J Clin Microbiol Infect Dis, 2016. **35**(12): p. 1923-1931.
182. Barth, A., *Infrared Spectroscopy of Proteins*. Biochim Biophys Acta, 2007. **1767**(9): p. 1073-101.
183. Haris, P.I. and D. Chapman, *The Conformational Analysis of Peptides Using Fourier Transform IR Spectroscopy*. Biopolymers, 1995. **37**(4): p. 251-63.

184. Arrondo, J.L. and F.M. Goni, *Structure and Dynamics of Membrane Proteins as Studied by Infrared Spectroscopy*. Prog Biophys Mol Biol, 1999. **72**(4): p. 367-405.
185. Gugutkov, D., et al., *Biological Activity of the Substrate-Induced Fibronectin Network: Insight Into the Third Dimension Through Electrospun Fibers*. Langmuir, 2009. **25**(18): p. 10893-900.
186. Rief, M., et al., *The Mechanical Stability of Immunoglobulin and Fibronectin III Domains in the Muscle Protein Titin Measured by Atomic Force Microscopy*. Biophys J, 1998. **75**(6): p. 3008-14.
187. Oberhauser, A.F., et al., *The Mechanical Hierarchies of Fibronectin Observed with Single-Molecule AFM*. J Mol Biol, 2002. **319**(2): p. 433-47.
188. Alegre-Cebollada, J., C.L. Badilla, and J.M. Fernandez, *Isopeptide Bonds Block the Mechanical Extension of Pili in Pathogenic Streptococcus Pyogenes*. J Biol Chem, 2010. **285**(15): p. 11235-42.
189. Castelain, M., et al., *The Nanomechanical Properties of Lactococcus lactis Pili Are Conditioned by the Polymerized Backbone Pilin*. PLoS One, 2016. **11**(3): p. e0152053.
190. Alon, R., et al., *The Kinetics of L-selectin Tethers and the Mechanics of Selectin-Mediated Rolling*. J Cell Biol, 1997. **138**(5): p. 1169-80.
191. Henriques-Normark, B. and S. Normark, *Commensal Pathogens, with a Focus on Streptococcus Pneumoniae, and Interactions with the Human Host*. Exp Cell Res, 2010. **316**(8): p. 1408-14.
192. Lofling, J., et al., *Cellular Interactions by LPxTG-Anchored Pneumococcal Adhesins and Their Streptococcal Homologues*. Cell Microbiol, 2011. **13**(2): p. 186-97.
193. Roman, J., *Extracellular Matrix and Lung Inflammation*. Immunol Res, 1996. **15**(2): p. 163-78.
194. Annoni, R., et al., *Extracellular Matrix Composition in COPD*. Eur Respir J, 2012. **40**(6): p. 1362-73.
195. Lin, M., et al., *Adsorption Force of Fibronectin on Various Surface Chemistries and its Vital Role in Osteoblast Adhesion*. Biomacromolecules, 2015. **16**(3): p. 973-84.
196. Mishra, A., et al., *Two Autonomous Structural Modules in the Fimbrial Shaft Adhesin FimA Mediate Actinomyces Interactions with Streptococci and Host Cells During Oral Biofilm Development*. Mol Microbiol, 2011. **81**(5): p. 1205-20.
197. Nelson, A.L., et al., *RrgA Is a Pilus-Associated Adhesin in Streptococcus Pneumoniae*. Mol Microbiol, 2007. **66**(2): p. 329-40.
198. King, S.J., *Pneumococcal Modification of Host Sugars: a Major Contributor to Colonization of the Human Airway?* Mol Oral Microbiol, 2010. **25**(1): p. 15-24.
199. Kadler, K.E., et al., *Collagen Fibril Formation*. Biochem J, 1996. **316** ( Pt 1): p. 1-11.
200. Kadler, K.E., et al., *Collagens at a Glance*. J Cell Sci, 2007. **120**(Pt 12): p. 1955-8.

## References

---

201. Huang, X., et al., *Single-Molecule Level Binding Force Between Collagen and Collagen Binding Domain-Growth Factor Conjugates*. *Biomaterials*, 2013. **34**(26): p. 6139-46.
202. Mostaco-Guidolin, L., N.L. Rosin, and T.L. Hackett, *Imaging Collagen in Scar Tissue: Developments in Second Harmonic Generation Microscopy for Biomedical Applications*. *Int J Mol Sci*, 2017. **18**(8).
203. Elliott, D.H., *Structure and Function of Mammalian Tendon*. *Biol Rev Camb Philos Soc*, 1965. **40**: p. 392-421.
204. Weiner, S. and W. Traub, *Bone Structure: from Angstroms to Microns*. *FASEB J*, 1992. **6**(3): p. 879-85.
205. Lekka, M., et al., *Friction Force Microscopy as an Alternative Method to Probe Molecular Interactions*. *J Chem Phys*, 2005. **123**(1): p. 014702.
206. Madani, A., K. Garakani, and M.R.K. Mofrad, *Molecular Mechanics of Staphylococcus Aureus Adhesin, CNA, and the Inhibition of Bacterial Adhesion by Stretching Collagen*. *PLoS One*, 2017. **12**(6): p. e0179601.
207. Shoemaker, C.T., et al., *Elevated Ratios of Type I/III Collagen in the Lungs of Chronically Ventilated Neonates with Respiratory Distress*. *Pediatr Res*, 1984. **18**(11): p. 1176-80.
208. Last, J.A., A.D. Siefkin, and K.M. Reiser, *Type I Collagen Content Is Increased in Lungs of Patients with Adult Respiratory Distress Syndrome*. *Thorax*, 1983. **38**(5): p. 364-8.
209. Xue, Y., et al., *Quantifying Thiol-Gold Interactions Towards the Efficient Strength Control*. *Nat Commun*, 2014. **5**: p. 4348.
210. Butt, H.J., Jaschke, M., *Calculation of Thermal Noise in Atomic Force Microscopy*. *Nanotechnology* 1995. **6**: p. 1-7.
211. Oesterhelt, F., M. Rief, and H.E. Gaub, *Single Molecule Force Spectroscopy by AFM Indicates Helical Structure of Poly(ethylene-glycol) in Water*. *New Journal of Physics*, 1999. **1**.

## **10 Supplementary Information**





## 10.1 Figures

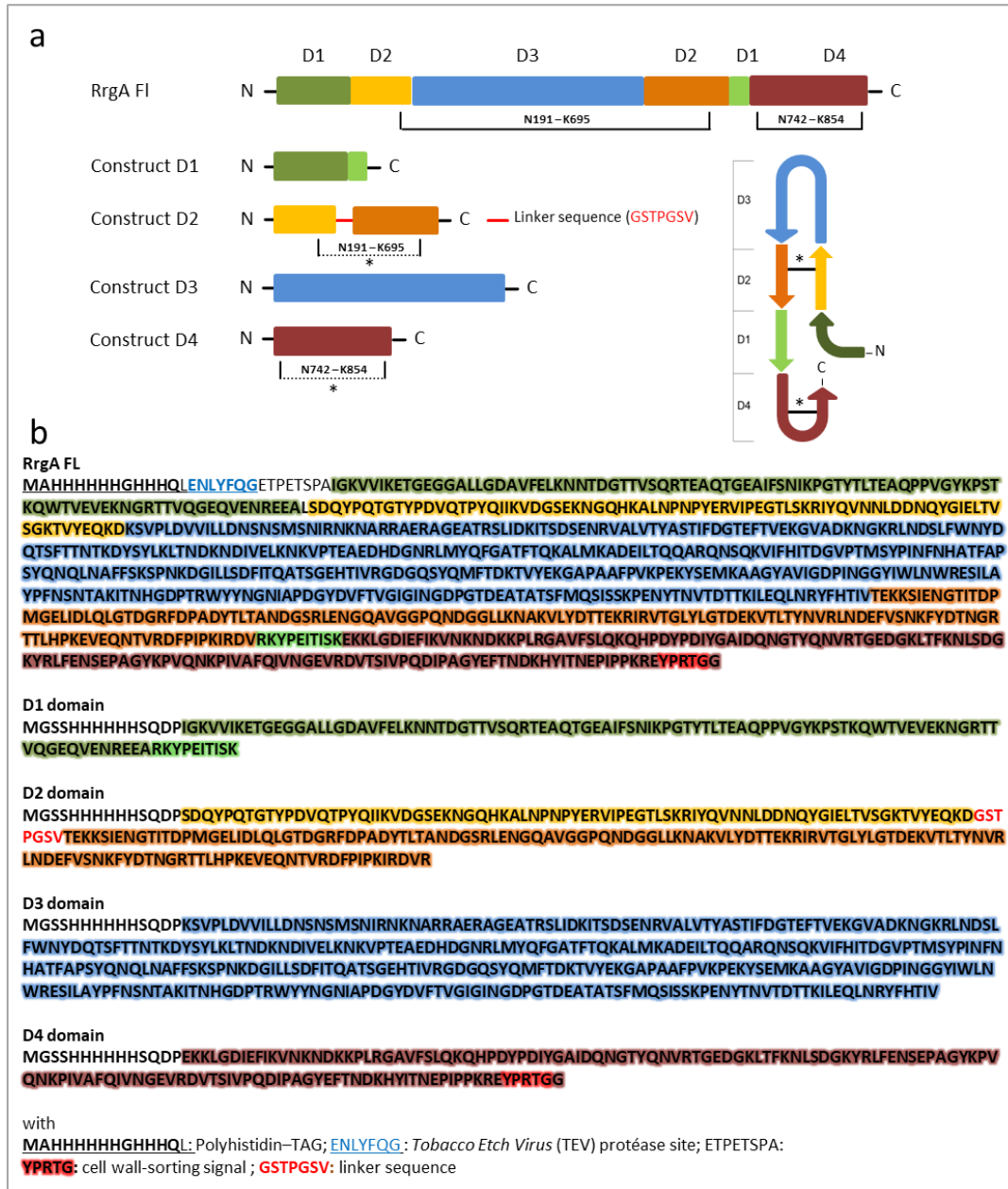


**Figure S1: Illustration of RrgA FI domain organization and corresponding structure-based expression.**

(a) RrgA (locus tag: SP\_RS02280, PDB: 2WW8) consists of four domains: Domain D3 (blue) is inserted into domain D2 (yellow/orange), both are inserted in D1 (green) forming a hairpin-like structure. D4 forms the C-terminal part of the protein. Intramolecular isopeptide bonds (\*) are formed within D2 and D4 (adapted from Izoré, T., *et al.*, Structure 2010 [88]). (b) Corresponding amino acid sequence of RrgA FI and domains. The respective D1 construct is composed of both D1 subunits, which were genetically fused. D2 subdomains were connected by a short linker sequence (GSTPGSV). Constructs D3 and D4 were cloned in consensus of their native sequence. Additionally, all constructs are provided with a N-terminal Polyhistidin-

## Supplementary Information

TAG. Colour codes: D1, green; D2, yellow/orange; D3, blue; D4, red. The figure has been adapted from Becke *et al.*, ACSnano, 2018 [105].

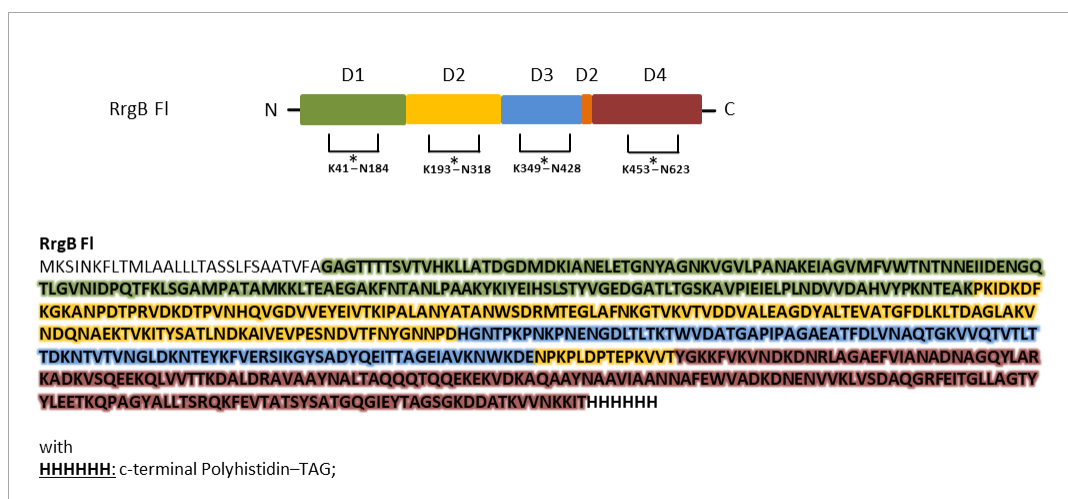


**Figure S2: Illustration of RrgB FI domain organization.**

RrgB FI (PDB: 2Y1V) consists of four domains: domains D1 (green), D2 (yellow/orange) and D4 (red) are arranged like pearls on a string with domain D3 (blue) laterally arranged relative to domain D2. D1 forms the N-terminal and D4 the C-terminal part of the protein. Intramolecular isopeptide bonds (\*) are formed within all domains (adapted from El Mortaji, *et al.*, Biochem. J. 2012 [89]). In addition, corresponding amino acid sequence of RrgB FI with a C-terminal Polyhistidin-TAG is shown.

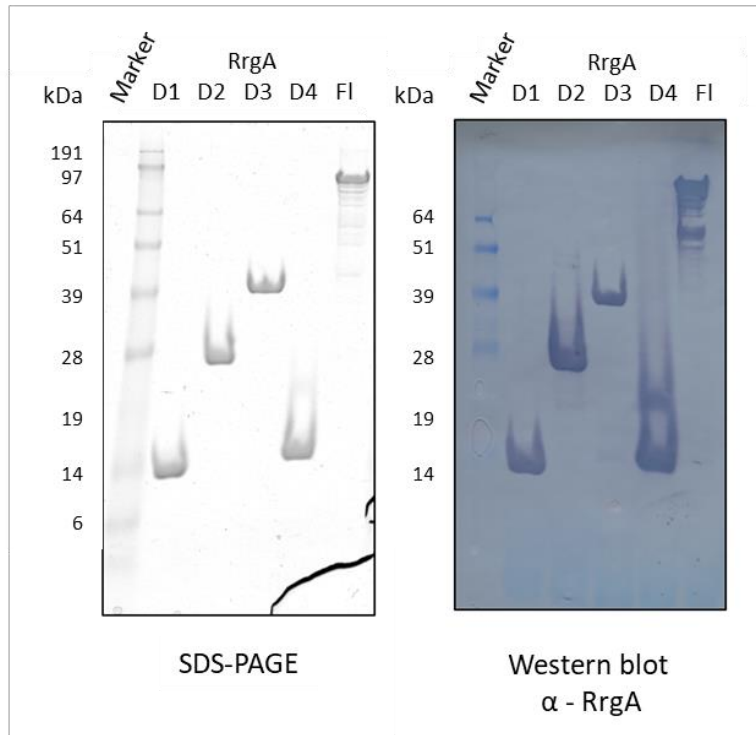


**Figure S3: Purified RrgA FI and single domain D1-D4 proteins.<sup>4</sup>**

His-tagged RrgA-constructs (Fig. S1) were heterologously expressed in *E. coli* (BL21-CodonPlus DE3-RIL) and corresponding proteins were purified using immobilized metal chelate affinity chromatography followed by size exclusion chromatography. SDS-PAGE separation followed by staining with Coomassie Brilliant Blue confirmed purity and estimated molecular weights of RrgA FI and single domain D1–D4 proteins (left). Western blot analysis using polyclonal anti-RrgA antibodies further proved protein identity (right).

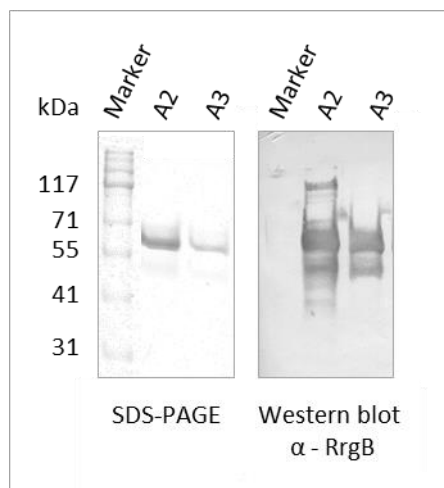


**Figure S4: Purified RrgB FI.<sup>4</sup>**

His-tagged RrgB (Fig. S2) were heterologously expressed in *E. coli* (Top 10). Proteins were purified using immobilized metal chelate affinity chromatography followed by size exclusion chromatography, which resulted in two fractions (A2, A3), of which fraction A3 was used. SDS-PAGE separation followed by staining with Coomassie Brilliant Blue confirmed purity and estimated molecular weights of RrgB FI (left). Western blot analysis using polyclonal anti-RrgB antibodies further proved protein identity (right).

<sup>4</sup> Protein expression and purification, photometric determination of protein concentration, SDS-PAGE and WESTERN blot analysis was mainly performed by Stefan Ness, M.Sc. (FG Protein Biochemistry & Cellular Microbiology, Munich University of Applied Sciences, 80335 Munich, Germany).

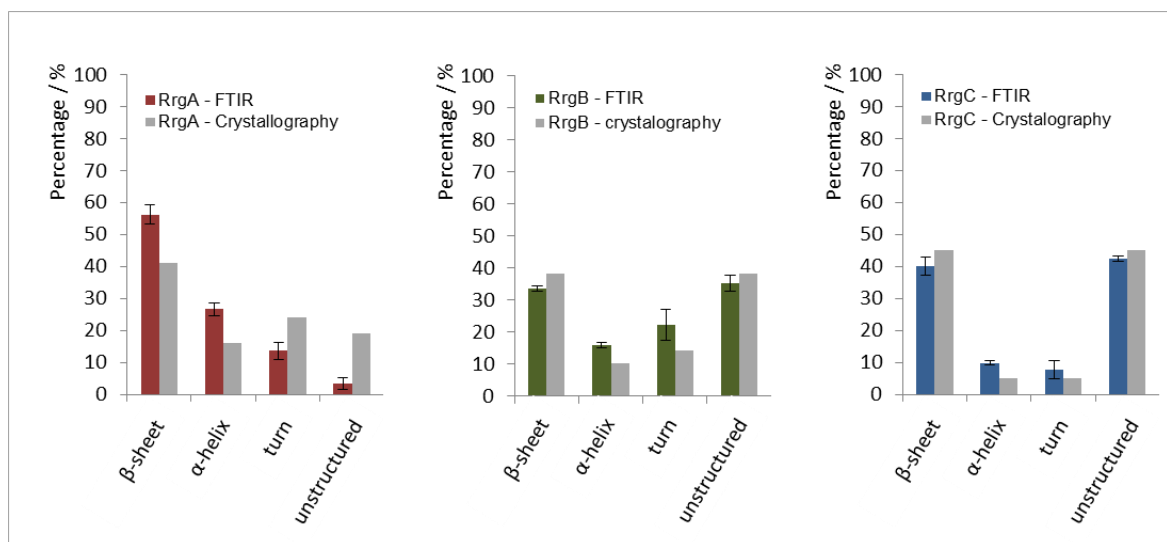


**Figure S5: RrgA FI, RrgB FI and RrgC FI secondary structure.**

Attenuated Total Reflection Fourier Transform Infrared Spectroscopy with subsequent multi-peak fit (Gaussian shape) of the amide I band ( $1700-1600\text{ cm}^{-1}$ ) revealed the secondary structure of RrgA FI (red), RrgB FI (green) and RrgC FI (blue) (PBS pH 7.4,  $n=3$ ). Structure was compared with crystallography data (grey bars) adapted from Izoré *et al.*, Structure 2010 for RrgA FI [88], El Mortaji *et al.*, Biochem. J., 2012 for RrgB FI [89] and Shaik *et al.* J. Biol. Chem., 2014 for RrgC FI [90].

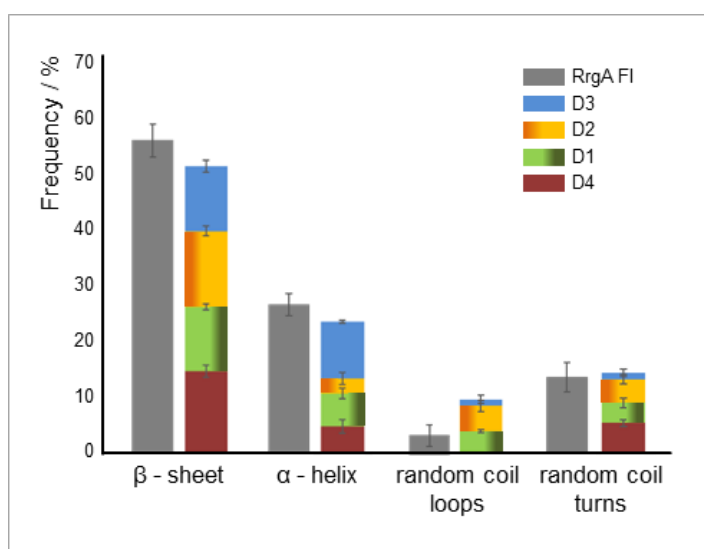


**Figure S6: RrgA FI and single domains D1-D4 secondary structure.** Attenuated Total Reflection Fourier Transform Infrared Spectroscopy with subsequent multi-peak fit (Gaussian shape) of the Amid I band ( $1700-1600\text{ cm}^{-1}$ ) revealed the secondary structure of RrgA FI and its' domains D1-D4 in solution (PBS, pH 7.4,  $n=3$ ). The domains D1, D2 and D4 predominantly consist of  $\beta$ -sheets, whereas D3 exhibits an equal part of  $\alpha$ -helices (compare Izoré, T., *et al.*, Structure 2010 [88]). The figure has been adapted from Becke *et al.*, ACSnano, 2018 [105].

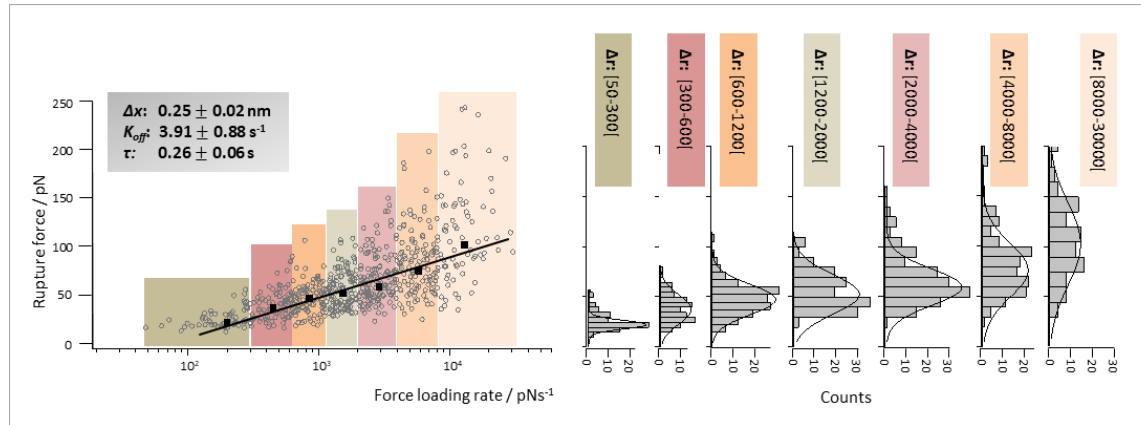


**Figure S7: Calculation of most probable rupture forces.**

Semilogarithmic representation of the RrgA FI-Fn rupture force as a function of the loading rate ( $r$ ) at retraction velocities between 250 to 4000 nm s<sup>-1</sup> (left). Gray circles represent individual rupture events, whereas the black squares show the most probable rupture force  $f_{MP}$  for seven distinct force-loading rate intervals ( $\Delta r$ ) between 50 and 30.000 pN s<sup>-1</sup> determined by fitting Gaussian distributions to the rupture force histograms (right). The black line (left) represents a Bell[-Evans-Ritchie] fit to the seven  $f_{MP}$  values with the fit parameters  $\Delta x = 0.25$  nm, and  $k_{off} = 3.91$  s<sup>-1</sup> (corresponding to  $\tau = 0.26$  s). The most probable rupture forces of domains D3 and D4 on Fn were calculated in an analogous manner. The figure has been adapted from Becke *et al.*, ACSnano, 2018 [105].

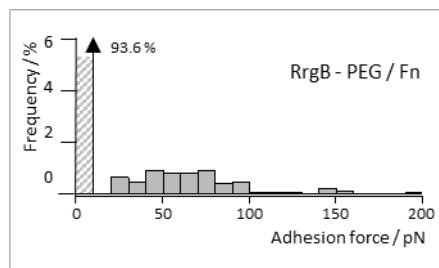


**Figure S8: Rupture force histograms obtained from RrgB FI-Fn interaction** ( $n = 1200$ ). Compare with data shown in Figure 7.1, main text).

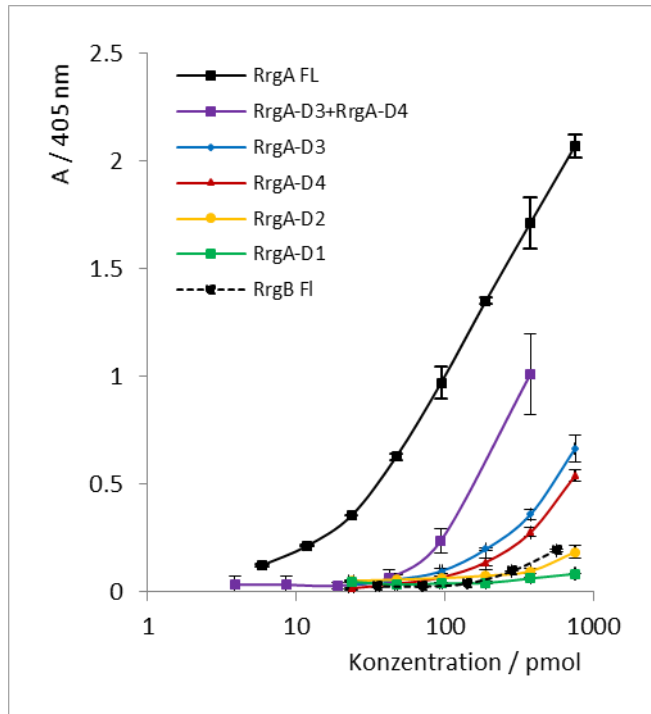


**Figure S9: ELISA results of RrgA FI, individual RrgA domains D1 – D4 and RrgB FI against Fn.**

RrgA FI (black) showed dose depending binding to Fn. Domains D3 (blue) and D4 (red) were able to bind to Fn but to a lesser extent as RrgA FI. Simultaneous binding of domains D3 and D4 (violet) at same molar concentrations resulted in a more than twofold higher signal as for the interaction of individual domains D3 and D4. The binding of domains D1 (green), D2 (orange) and RrgB FI (black, dashed) to Fn was insignificant. Two-fold dilution of all samples started at an equimolar ratio of 750 pmol/well. Absorbance was measured at 405 nm. Dots represent mean values, error bars indicate high/low values of the duplicates. The ELISA was repeated several times and showed unsteady results with same tendency.

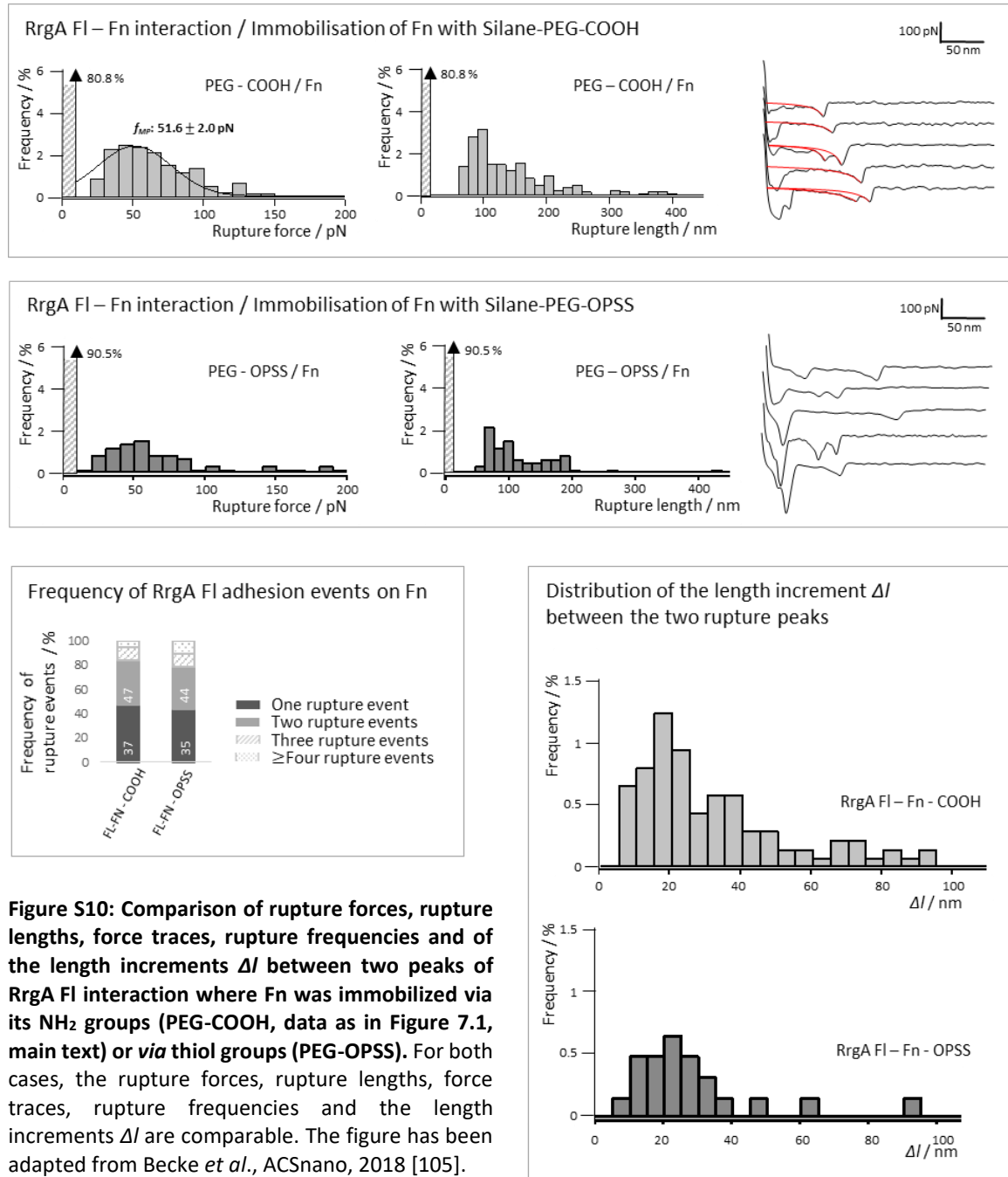


**Figure S10: Comparison of rupture forces, rupture lengths, force traces, rupture frequencies and of the length increments  $\Delta l$  between two peaks of RrgA FI interaction where Fn was immobilized via its  $\text{NH}_2$  groups (PEG-COOH, data as in Figure 7.1, main text) or via thiol groups (PEG-OPSS).** For both cases, the rupture forces, rupture lengths, force traces, rupture frequencies and the length increments  $\Delta l$  are comparable. The figure has been adapted from Becke *et al.*, ACSnano, 2018 [105].

## 10.2 Protocols

### 10.2.1 Purification of Proteins<sup>5</sup>

#### IMAC:

Note: The following protocol was used for the purification of RrgA Fl and individual domains (D1-D4) with a Column HisTrap HP and a Äkta avant 25 system (GE Healthcare). The protocol can be adapted to purify other proteins containing a Polyhistidin–TAG.

- Equilibrate the column with 5 column volumes (CV) of Buffer A (50 mM Tris-HCl, 150 mM NaCl, pH 8.0) including 4 % Buffer B (50 mM Tris-HCl, 150 mM NaCl, 500 mM Imidazole, pH 8.0) at a flow rate of 1 ml min<sup>-1</sup>.
- Apply the sample at a flow rate of 0.5 ml min<sup>-1</sup> including 4 % Buffer B to prevent unspecific protein binding.
- Wash column with 6 CV of 4 % Buffer B at a flow rate of 1 ml min<sup>-1</sup>.
- Eluate proteins in a three step elution at a flow rate of 1 ml min<sup>-1</sup> with
  - 6 CV of 10 % Buffer B
  - 6 CV of 30 % Buffer B (Elution of protein)
  - 6 CV of 100 % Buffer B.
- Wash column with 10 CV of 100 % Buffer B at a flow rate of 1 ml min<sup>-1</sup> to remove all residues from the column.

---

<sup>5</sup> Protein expression and purification was mainly performed by Stefan Ness, M.Sc. (FG Protein Biochemistry & Cellular Microbiology, Munich University of Applied Sciences, 80335 Munich, Germany).



**SEC:**

Note: The following protocol was used for a polishing of already IMAC purified RrgA FI samples with a Superdex 200 10/300 GL column and a Äkta avant 25 system (GE Healthcare). The column needs to be adapted to fit the protein size.

- Wash column with 4 CV of ddH<sub>2</sub>O at a flow rate of 0.8 ml min<sup>-1</sup>.
- Equilibrate column with 2 CV of PBS buffer at a flow rate of 0.8 ml min<sup>-1</sup>. Sufficient equilibration is indicated by constant absorption and conductometry signals.
- Fill a 500 µl sample loop with the respective pooled and concentrated IMAC sample (500 µl)
- Apply IMAC sample through rinsing the loop with 1 ml PBS buffer at a flow rate of 0.8 ml min<sup>-1</sup>.
- Eluate proteins with 1.5 CV of PBS at a flow rate of 0.8 ml min<sup>-1</sup>.

## 10.2.2 Immobilization of Proteins for SMFS and LFM

The following protocol is part of the article

### “Covalent Immobilization of Proteins for the Single Molecule Force Spectroscopy”

by Tanja D. Becke, Stefan Ness, Stefanie Sudhop, Hermann E. Gaub, Markus Hilleringmann, Arndt F. Schilling, and Hauke Clausen-Schaumann

Published: Journal of Visualized Experiments, 2018, (138).

DOI: 10.3791/58167 [132]

### 1. Immobilization of Proteins *via* Functional Silane Coupling Agents

**Note:** Figure [...] [3.8] gives an overview over the surface chemistry applied in this protocol.

**Caution:** In the following protocol different chemicals with corrosive and skin irritating properties are used. Wear adequate (acid-resistant) gloves, safety goggles, laboratory coat and work under the fume hood while preparing solutions in order to avoid inhalation of vapors.

#### 1.1. Functionalization of Glass Surfaces and Silicon Nitride Cantilever with Silane Coupling Agents

**1.1.1.** Remove coarse dust and contaminations from glass slides with isopropanol and lint-free precision wipes and cut slides in desired size (optional).

Note: Beside glass, the solid surface can be silica, quartz, and the oxides of aluminum, copper, tin, titanium, iron, chromium, zirconium, nickel, and zinc.

CAUTION: Cutting the glass slides may cause sharp edges.

**1.1.2.** Place glass slides in a staining jar filled with hydrochloric acid (33% HCl) diluted with doubly distilled water (ddH<sub>2</sub>O) to 3 - 5 % v/v, close jar with appropriate lid and place it in an ultrasonic bath for 90 min at room temperature.

Note (1): The used jar has a diameter of 6 cm and an approximate size of 65-70 ml. An appropriate volume of diluted HCl for the jar is 50 ml containing 5 ml 33 % HCl and 45 ml ddH<sub>2</sub>O.

Note (2): The HCl effectively removes non-binding metal ions, especially sodium, potassium, and calcium and reduces the silicon in order to produce a hydroxyl saturated glass surface.

CAUTION: HCl is corrosive and skin irritating. Wear adequate acid-resistant gloves, safety goggles, laboratory coat and work under the fume hood while preparing the solution in order to avoid inhalation of vapors.

- 1.1.3.** Place silicon nitride AFM cantilever probes on a clean glass slide with the tip facing upwards and irradiate with ultra violet light from above for at least 90 min.

Note (1): For single molecule force spectroscopy cantilevers with a nominal spring constant of 0.01 to 0.1 N m<sup>-1</sup> are suitable.

Note (2): Irradiation of the cantilever surface with UV light will remove organic contaminants, mainly fat substances, and render it hydrophilic on one side. If the other side is heavily contaminated - which should not be the case, if the cantilever probes are used fresh out of the suppliers' box - it may affect the SMFS measurement. A thorough cleaning of the whole cantilever chip using piranha solution, which has been used in many studies, may help [209].

CAUTION: UV light is harmful to the eyes, therefore irradiation of the cantilever probes should be carried out in an UV light impermeable chamber.

CAUTION: Piranha solution is highly reactive and may burn skin, paper and other organic material. Do not use plastic containers. If placed in dishes or jars even with small amounts of organic surface contaminations (*e.g.* from previous use) it may react rapidly.

- 1.1.4.** Substitute the hydrochloric acid in the staining jar with ddH<sub>2</sub>O without letting the glass surface dry and place the jar back in the ultrasonic bath for another 10 min. Replace the water two more times for 10 min respectively to properly wash off the hydrochloric acid.

- 1.1.5.** In the meantime dissolve ethoxy (or methoxy) silane polyethylene glycol acid (Si(OC<sub>2</sub>H<sub>5</sub>)<sup>3</sup>-PEG-COOH) in a mixture of ethanol and doubly distilled water (v/v 95 %/5 %, pH 4.6 adjusted with acetic acid) to a final concentration of 0.1 mg ml<sup>-1</sup>. Store solution hermetically sealed in order to avoid evaporation of the ethanol.

Note (1): Silane coupling agents are sensitive to moisture and temperature. Therefore, they should be stored under inert gas (nitrogen, N), at low temperature (-20 °C) and under dry conditions. Before opening the flask, make

sure that the silanes have reached room temperature to minimize hydration and thereby passivation of reactive groups.

Note (2): Heterobifunctional PEG coupling agents are available with numerous different functional groups and different spacer lengths. For random immobilization of proteins *via* their free amino groups (NH<sub>2</sub>), as described in this protocol, the functional group additional to the ethoxy/methoxy silane must be a N-Hydroxysuccinimid (NHS) ester. Beside the purchase of a silane agent with NHS ester, a simple way to gain such NHS ester is to activate a carboxyl group (-COOH) with 1-Ethyl-3-(3-dimethylaminopropyl) carbodiimid (EDC) and NHS (see 1.2.1. and 1.2.2.).

CAUTION: Ethanol is flammable and skin irritating. Acetic acid is flammable and corrosive. Take care not to get reactive silanes onto the skin or into the eyes. Wear adequate gloves, safety goggles, laboratory coat and work under the fume hood in order to avoid inhalation of vapors.

- 1.1.6.** Pour the silane solution in two separate petri dishes, place prepared cantilever probes and glass slides in one petri dish respectively, seal hermetically (*e.g.* parafilm) to avoid evaporation of the ethanol out of the solution and incubate stationary for 90 min at room temperature.

Note (1): The optimal size of the petri dish depends on the number of cantilever probes and the size of the glass slides which should be functionalized. A diameter size for good handling and low reagent volume is 50-60 mm.

Note (2): To avoid undesired bending of the cantilever while penetrating through the air water interface the cantilever should be held at a 90° angle to the air-water interface.

Note (3): The incubation of the glass slides (but not the cantilever probes) can optionally be carried out on an orbital shaker.

- 1.1.7.** Rinse cantilever and glass slides in three consecutive beakers containing pure ethanol to completely wash off the unbound silane compounds.

Note: To avoid undesired bending of the cantilever while penetrating through the air water interface the cantilever should be held at a 90° angle.

- 1.1.8.** Place functionalized glass slides in staining jar and cantilever on a clean glass slide and cure at 110 °C for 30 min.

Note (1): Curing with heat induces the formation of covalent siloxane bonds and the removal of water.

Note (2): As the glass slides were only functionalized on the one side, make sure to properly indicate the coated side.

- 1.1.9.** Store silanized glass samples and cantilever probes in a vacuum desiccator for up to one week.

Note: The protocol can be paused here.

## **1.2. Random Immobilization of Proteins on Silanized Glass and Silicon Nitride Cantilever**

Note: To avoid undesired bending of the cantilever, the cantilever probe should be held at a 90° angle while penetrating any air-water interfaces.

- 1.2.1.** Prepare a solution containing 42 mg ml<sup>-1</sup> of 1-(3-dimethylaminopropyl)-3-ethylcarbodiimide (EDC) and 20 mg ml<sup>-1</sup> N hydroxysuccinimide (NHS) in standard phosphate buffered saline (PBS; 137 mM NaCl, 2.7 mM KCl, 10 mM Na<sub>2</sub>HPO<sub>4</sub>, 1.8 mM KH<sub>2</sub>PO<sub>4</sub>, pH 7.4).

CAUTION: EDC is corrosive and skin irritating and can cause serious eye damage. Wear adequate gloves, safety goggles and laboratory coat.

- 1.2.2.** Cover silane coated glass slides with the solution and put silanized cantilever probes in a drop of the EDC/NHS solution and incubate for 10 min at room temperature.

Note (1): For the incubation of the cantilever probes, the original cantilever box is suitable.

Note (2): To couple proteins *via* their free amino groups to the carboxyls (-COOH) of the heterobifunctional silane-PEG agents, the -COOH group is activated with the widely used EDC/NHS chemistry. EDC couples NHS to the carboxylic acid, forming a “stable” NHS ester which enables efficient conjugation to primary amines at physiological pH in a next step.

- 1.2.3.** Rinse cantilever and glass slides thoroughly with PBS in three consecutive beakers in order to completely wash off excessive EDC/NHS.

Note: This washing step is critical as remaining EDC/NHS can crosslink proteins and thereby alter their functionality.

- 1.2.4.** Incubate activated glass slides with and cantilever probes in a droplet of the desired protein solution in a wet chamber at room temperature. The protein concentration and incubation time should be adapted to meet the requirements of the experiment. In general a concentration between 0.5 to

## ***Supplementary Information***

---

1 mg ml<sup>-1</sup> and incubation times from 30 min to 2 h are suitable for most proteins. (In the case of fibronectin (on glass slide) and pilus-1 tip protein RrgA (on cantilever) a molar concentration of 1.5 μM and 3 μM, respectively, and an incubation time of 2 h are sufficient).

**1.2.5.** Wash glass slides and cantilever probes thoroughly with PBS in three consecutive beakers in order to wash off unbound proteins.

**1.2.6.** Saturate the remaining NHS ester with Tris(hydroxymethyl)-aminomethan by placing the probes in Tris-buffered saline (TBS; 50 mM Tris, 150 mM NaCl, pH 7.6) for 20 min at room temperature.

Note: This step reduces undesired covalent coupling of proteins between the functionalized surface of the AFM tip and the glass, because amino groups of Tris can bind to the remaining activated COOH groups on the cantilever and substrate surface.

**1.2.7.** Wash glass slides and cantilever probes thoroughly with PBS and store them in separate petri dishes covered in PBS until use.

Note: The samples should be prepared freshly and used the same day.

### 10.2.3 Atomic Force Microscopy Based Single Molecule Force Spectroscopy

The following protocol is part of the article

#### “Covalent Immobilization of Proteins for the Single Molecule Force Spectroscopy”

by Tanja D. Becke, Stefan Ness, Stefanie Sudhop, Hermann E. Gaub, Markus Hilleringmann, Arndt F. Schilling, and Hauke Clausen-Schaumann

submitted to the Journal of Visualized Experiments (Jove).

#### 1. Atomic Force Microscopy Based Single Molecule Force Spectroscopy

Note: In this work, a NanoWizard I atomic force microscope from JPK Instruments was used and set ups for obtaining force-distance curves was defined with the Force RampDesigner.

##### 1.1. Cantilever Calibration with the Thermal Noise Method [210]

Note (1): For cantilever calibration follow the step for step manual of the manufacturer.

Note (2): Most cantilever suppliers state an approximate spring constant, which is usually calculated from the nominal cantilever shape (length, width, thickness) and is therefore not very reliable.

Note (3): As the correct spring constant is crucial, it is advisable to carry out the cantilever calibration described below in triplicate and use the mean values of optical lever sensitivity and spring constant. It can be useful to record the cantilever deflection in volts (V) during the experiment and convert it to force (pN) afterwards, using the optical lever sensitivity and spring constant mean values.

Note (4): The spring constant and optical lever sensitivity can be determined before and/or after the experiment, as long as the laser position is not changed on the cantilever (the position of the reflected laser can be readjusted on the photodiode).

**1.1.1.** Fix a clean, fresh glass slide on the AFM sample holder and cover it with PBS buffer.

Note: The calibration should be carried out on a hard surface (e.g. glass) and in the same buffer as the actual experiments.

**1.1.2.** Fix the prepared cantilever probe at the cantilever holder, place it in the AFM head and carefully wet the cantilever with a drop of PBS buffer.

Note: The wetting of the cantilever reduces the surface tension appearing during penetration in the PBS buffer on the calibration glass slide and thereby undesirable bending of the cantilever.

**1.1.3.** Slowly move the cantilever towards the calibration surface until the cantilever is completely immersed in the PBS buffer but still away from the calibration surface.

**1.1.4.** Use the top view optical microscope of the AFM or (if available) the inverted microscope underneath the AFM to position the laser of the AFM on the backside of the cantilever. Place the laser spot near the end of the cantilever close to where the tip is located.

Note (1): The laser spot should be located close to the end of the cantilever, but it should still be completely on the cantilever.

Note (2): If no optical microscope is available, use a piece of paper for visible laser diodes or a laser detector card for infrared laser diodes, put it underneath the AFM head and move the laser spot towards the edge of the cantilever-chip, where the cantilevers are located, until you see the spot on the paper or detector card. Then move the laser parallel to the edge. When the spot disappears it is on a cantilever arm. For linear cantilevers, move the spot towards the end of the lever arm until it appears on the paper / detector card and move it back until it is again on the lever arm (disappears from the paper/card). For triangular place the spot in the middle between two arms of the cantilever and move it towards the end of the cantilever, until it disappears from the paper/card. Check that you are in the middle of the cantilever by moving the spot perpendicular to the long axis of the cantilever.

**1.1.5.** Adjust the position of the four quadrant detector photodiode of the AFM in such a way that the reflected laser beam is positioned in the center of the photodiode.

Note (1): Proceed as follows: Use the micrometer screws near the detector diode to move the diode in horizontal and in vertical direction, until the sum signal from all four quadrants is maximized. Then move the diode in vertical direction, until the vertical deflection signal is zero, and move the diode in horizontal direction, until the lateral deflection signal is zero.

Note (2): Silicon nitride cantilevers usually have a gold coating and are therefore a bimetal with two different coefficients of thermal expansion. This results in a thermal drift (apparent in the vertical deflection signal) especially in solution. To reduce this drift during measurements, let the whole system equilibrate for a few minutes before starting the calibration.



- 1.1.6. Open the calibration manager in the AFM software and calibrate the cantilever sensitivity and spring constant of the cantilever with the thermal noise method as follows:
- 1.1.7. Record several thermal noise spectra of the cantilever with the cantilever approximately 100  $\mu\text{m}$  or more away from the surface in order to exclude any surface damping.
- 1.1.8. Determine the spring constant in pN/V of the cantilever by fitting a harmonic oscillator provided by the AFM software to the thermal noise spectra.
- 1.1.9. Carefully approach the substrate surface and record a force-distance curve.
- 1.1.10. Determine the optical lever sensitivity in nm/V by fitting a straight line to the steepest part of the retraction force curve, where the tip is in contact with the substrate surface. The sensitivity enables you to convert the cantilever spring constant to pN/nm.

Note: The slope of the retraction curve is the piezo travel distance vs. the change in photodiode voltage (measured in nm/V).

- 1.1.11. Slowly retract the cantilever and withdraw it from the solution.
- 1.1.12. Substitute the glass surface used for cantilever calibration with the sample surface containing the immobilized proteins.

Note: Make sure that the cantilever and the sample surface (and thereby the proteins) do not dry while changing the glass slides.

## **1.2. Interaction Force Experiments on the single protein level**

- 1.2.1. Slowly move the (still) moist cantilever towards the sample surface until the cantilever is completely covered by PBS buffer but still away from the substrate surface.

Note: To reduce the thermal drift during the experiment, let the whole system set for a few minutes before starting the force spectroscopy measurements.

- 1.2.2. Approach the surface and record multiple force-distance curves ( $\geq 500$ ) at different locations of the sample surface, with e.g. a contact force of 250 pN, a contact time of 1 s, a retraction length of 2  $\mu\text{m}$  and a retraction velocity of 1  $\mu\text{m s}^{-1}$ .

Note (1): For general force spectroscopy adjustments follow the manufacturer's manual.

Note (2): Variations: The retraction speed can be varied between e.g. 0.1 and 5  $\mu\text{m s}^{-1}$  to calculate kinetical data depending on the increasing force load. The interaction time can be varied to e.g. analyze time dependent bond strengthening. Instead of keeping the retraction speed constant, one may keep the force constant (force clamp mode).

### 1.3. Data analysis

Note (1): Data analysis was carried out using the data processing software.

Note (2): Depending on the immobilized proteins, the contact time or the retraction speed, whether a footprint was incorporated or not and other variable parameters, the force-distance curves contain multiple different information. Data analysis and interpretation can vary greatly between different SMFS experiments and can therefore not be described in detail here. As for the interaction of RrgA and Fn, the following protocol can be a first step for the analysis of SMFS data.

**1.3.1.** Open the measured force curve files by selecting the "Open Batch of Force Scan" icon and process the force-distance curves as follows:

**1.3.2.** Convert the cantilever deflection (V) to the directly proportional force (F) by selecting the "(Re)Calibrate the V-deflection by Adjusting Sensitivity and Spring Constant" icon.

Note: If cantilever calibration was carried out before the experiment, the values are saved in the force scan files and are automatically used during calibration of the V-deflection. If the calibration was carried out after the experiment, the software uses default values, which can be changed to the measured values.

**1.3.3.** Subtract the baseline of the retraction channel in a region of the force curve far from the surface to set the zero force level by selecting the icon "Baseline Subtraction".

Note: In some cases, the retraction may not have the same constant force value and the curve may display a linear tilt, which can be removed by selecting "Offset + Tilt".

**1.3.4.** Define the point where the tip gets into contact with the sample by selecting the "Contact Point Determination" icon.

- 1.3.5.** Convert the height signal to tip-sample separation by selecting the “Tip-Sample Separation” icon. In addition to subtracting the contact point position, this procedure subtracts the cantilever bending to calculate the distance between substrate surface and AFM-tip.

Note: For fitting polymer elastic models, like the extensible worm-like-chain model and the determination of interaction lengths the tip-sample separation which is corrected for the cantilever bending is needed. To determine the force loading rate from the slope of the force curve and the z-piezo velocity, the uncorrected force curves should be used.

- 1.3.6.** Screen the force-distance traces for force peaks occurring at rupture lengths above 70 nm (length of the stretched PEG spacer) [211] to sort out nonspecific interactions and apply the extensible worm-like-chain model to the selected peaks by selecting the “Fit a Polymer Chain Model” icon and chose the “Extensible Worm-like Chain Model”. The peaks in the retraction force curve will be fitted with this model and rupture forces and lengths are obtained, together with the elastic parameters of the polymer.

- 1.3.7.** Display the data as histograms showing the force and length distributions. Use at least 100 unbinding events for the histograms.



## 11 Lebenslauf

### Persönliche Daten

Name	Tanja Becke
Adresse	Fürholzer Weg 33c, 85375 Neufahrn
Tel.	0176/24853515
E-Mail	tbecke@hm.edu
geb.	14.10.1987 in 85356 Freising

### Bildungsweg

2014 - 2019	Kooperative Promotion an der Technische Universität München und der Hochschule München im Labor für Nanoanalytik und Biophysik sowie Proteinchemie und zelluläre Mikrobiologie
2012 - 2014	Studium an der Hochschule Weihenstephan-Triesdorf und Hochschule München Masterstudiengang Biotechnologie / Bioingenieurwesen (M.Sc.)
2008 - 2012	Studium an der Hochschule München Bachelorstudiengang Bioingenieurwesen (B.Eng.)
2007 - 2008	Studium an der Technischen Universität München Bachelorstudiengang Informationstechnik (ohne Abschluss)
1998 - 2007	Allgemeine Hochschulreife am Josef-Hofmiller-Gymnasium Freising
1994 - 1998	Grundschule St. Lantpert Freising



## 12 Eidesstattliche Erklärung

Ich erkläre an Eides statt, dass ich die bei der promotionsführenden Einrichtung  
Fakultät für Medizin

der TUM zur Promotionsprüfung vorgelegte Arbeit mit dem Titel:

*Streptococcus pneumoniae* TIGR4 pilus-1 biomechanical aspects of adhesion during interaction with the host

in der Forschungsgruppe Experimentelle Plastische Chirurgie

unter der Anleitung und Betreuung durch: Prof. Arndt F. Schilling

ohne sonstige Hilfe erstellt und bei der Abfassung nur die gemäß § 6 Ab. 6 und 7 Satz 2 angebotenen Hilfsmittel benutzt habe.

- Ich habe keine Organisation eingeschaltet, die gegen Entgelt Betreuerinnen und Betreuer für die Anfertigung von Dissertationen sucht, oder mir die obliegende Pflichten hinsichtlich der Prüfungsleistungen für mich ganz oder teilweise erledigt.
- Ich habe die Dissertation in dieser oder ähnlicher Form in keinem anderen Prüfungsverfahren als Prüfungsleistung vorgelegt.
- Die vollständige Dissertation wurde in \_\_\_\_\_ veröffentlicht. Die promotionsführende Einrichtung \_\_\_\_\_ hat der Veröffentlichung zugestimmt.
- Ich habe den angestrebten Doktorgrad noch nicht erworben und bin nicht in einem früheren Promotionsverfahren für den angestrebten Doktorgrad endgültig gescheitert.
- Ich habe bereits am \_\_\_\_\_ bei der Fakultät für \_\_\_\_\_ der Hochschule \_\_\_\_\_ unter Vorlage einer Dissertation mit dem \_\_\_\_\_ Thema \_\_\_\_\_ die Zulassung zur Promotion beantragt mit dem Ergebnis: \_\_\_\_\_

Die öffentlich zugängliche Promotionsordnung der TUM ist mir bekannt, insbesondere habe ich die Bedeutung von § 28 (Nichtigkeit der Promotion) und § 29 (Entzug des Doktorgrades) zur Kenntnis genommen. Ich bin mir der Konsequenzen einer falschen Eidesstattlichen Erklärung bewusst.

Mit der Aufnahme meiner personenbezogenen Daten in die Alumni- Datei bei der TUM bin ich

- einverstanden,       nicht einverstanden

---

Ort, Datum, Unterschrift





## **13 Danksagung**

An dieser Stelle möchte ich mich bei all denjenigen bedanken, die mich während meiner Promotion mit guten Gedanken und Gesprächen begleitet und bei der Anfertigung meiner Doktorarbeit mit Rat und Tat unterstützt haben.

Zuerst gebührt mein Dank Prof. Arndt Schilling, der meine Doktorarbeit betreut und begutachtet hat. Die Möglichkeit meine Arbeit im Rahmen der besprochenen Arbeitspakete nach eigenem Ermessen gestalten zu können, die hilfreichen Anregungen in unseren persönlichen Gesprächen und die konstruktive Kritik bei der Erstellung der Veröffentlichungen und dieser Arbeit half mir mich, nicht nur im Arbeitsalltag, sondern auch persönlich, weiterzuentwickeln. Prof. Matthias Rief, der sich bereit erklärt hat die Arbeit mit physikalischem Blick zu betreuen und zu begutachten, danke ich ebenfalls für das in mich gesetzte Vertrauen und den Spielraum eigene Idee einbringen und umsetzen zu können.

Ich danke Prof. Hauke Clausen-Schaumann, der mir als Mentor während meiner Arbeit zur Seite stand. Bedanken möchte ich mich für die kontinuierlich hervorragende Betreuung, die auch über die eigentlich Arbeit hinaus reichte, und die zahlreichen interessanten Ideen und Debatten, die auch zusammen mit Dr. Stefanie Sudhop entstanden sind und maßgeblich dazu beigetragen haben, dass diese Doktorarbeit in dieser Form vorliegt. Des Weiteren bedanke ich mich für die vielen Stunden Arbeit, die in die Korrektur der Veröffentlichungen geflossen sind.

Ich danke Prof. Markus Hilleringmann, ohne dessen Hilfe dieses spannende Projekt nicht entstanden wäre und der mir mit seiner Expertise bei jeglichen Fragen zur Mikrobiologie (des Pneumokokkus) hilfreich zur Seite stand. Für die persönliche Betreuung, die Hilfe sowie die konstruktive Kritik bei der Erstellung von Veröffentlichungen und dieser Arbeit bin ich sehr dankbar.

## ***Danksagung***

---

Ich danke Prof. Hermann Gaub und den Mitarbeitern vom Institut für Angewandte Physik, Biophysik & Molekulare Materialien der Ludwig-Maximilians-Universität für die zeitlich begrenzte, aber sehr herzliche Aufnahme in ihre Arbeitsgruppe.

Ebenfalls möchte ich mich bei Dr. Michael Pill bedanken, der mir mit viel Geduld und Hilfsbereitschaft die kleinen und großen Geheimnisse der Rasterkraftmikroskopie offenbarte.

Stefan Ness danke ich für die Herstellung und Reinigung einer Vielzahl von Proteinen und für die produktive Zusammenarbeit an diesem spannenden Thema und nicht zu vergessen für die kleinen, aber immer wieder motivierenden Kaffeepausen. Ohne ihn als Zweitautor wären diese Arbeit und die vorrausgehenden Veröffentlichungen nicht zustande gekommen.

Ich danke Carina Prein und Stefanie Kiderlen, die jedes Mal ihre eigenen Arbeiten unterbrechen um mir bei meinen Versuchen zu helfen. Besonders möchte ich mich für den (emotionalen) Rückhalt, für die tollen Tage während Konferenzen und für das Aufrechterhalten der weiblichen „Power“ im Labor bedanken.

Abschließend möchte ich mich bei Bastian Hartmann, Benedikt Kaufmann, Julian Blaser, Conny Hasselberg-Christoph und Martina Hörig, sowie allen anderen Mitstreitern vom Centrum für Angewandtes Tissue Engineering und Regenerative Medizin (CANTER), dem Labor für Nanoanalytik und Biophysik und dem Labor für Protein Biochemistry / Cellular Microbiology bedanken, die mir meine Promotion durch ihre Unterstützung ermöglicht haben. Danke auch für die vielen Abende an denen wir zusammen gesessen und gefeiert haben- ihr habt meine Promotionszeit neben der Wissenschaft mit Freude und Spaß erfüllt.